UNIVERSITY OF TRENTO

Doctoral School in Civil, Environmental and Mechanical Engineering

Curriculum 3. Modelling and Simulation

Alberto Flor

Atomic Modelling of Disorder in Metal Nanocrystals

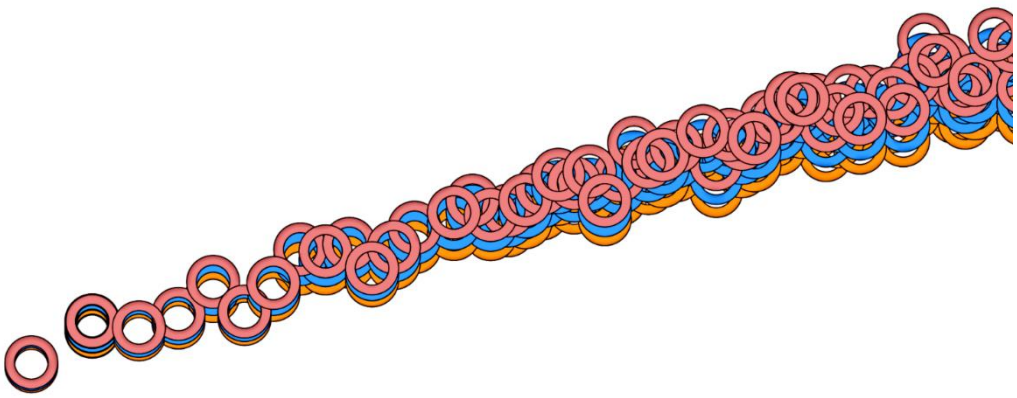

2019 - Doctoral Thesis

UNIVERSITY OF TRENTO - Italy
Department of Civil, Environmental and Mechanical Engineering

Doctoral School in Civil, Environmental and Mechanical Engineering Curriculum "Modelling and Simulation" – XXXI cycle
2016/2018

Doctoral Thesis - April 2019

Alberto Flor

ATOMIC MODELLING OF DISORDER IN METAL NANOCRYSTALS

Supervisor

Prof. Paolo Scardi, University of Trento

ISBN (paper): ..... ; ISBN (online):.....

University of Trento
Doctoral School in Civil, Environmental and Mechanical Engineering
http://web.unitn.it/en/dricam
Via Mesiano 77, I-38123 Trento
Tel. +39 0461 282670 / 2611 - *dicamphd@unitn.it*

“Premature optimization is the root of all evil”

Donald Knuth

ATOMIC MODELLING OF DISORDER IN METAL NANOCRYSTALS

Alberto Flor

Contents

.....Motivation and Methodology 1

1.1 Introduction 1

1.2 Nanoparticles and Catalysis 5

1.3 Molecular dynamics 11

1.3.1 MSRD and RPDF 13

1.3.2 Molecular Dynamics in practice: 17

1.4 Static and dynamic disorder 21

1.4.1 A full Mean Square Radial Displacement calculation 21

1.4.2 Separation of static and dynamic contributions to disorder 24

1.5 diffraction from nanocrystalline systems 34

1.5.1 Debye-Waller coefficient 34

1.5.2 X-Ray Powder Diffraction and Whole Powder Pattern Modelling 34

1.5.3 Warren's approach 39

..... Implementation of the Results 43

2.1.2 Parametrization of WPs 50

2.1.3 Real Powder sample vs MD simulation: the correction to $\Delta L2$ 52

2.1.4 Implementation of MD results in the WPPM 53

2.2 Further Applications 62

..... Application: Debye-Waller coefficient of heavily deformed nanocrystalline iron 63

3.1 Abstract 63

3.2 Introduction 63

3.3 Experimental 65

3.4 Numerical Simulations 67

3.5 Results and Discussion 68

3.6 Concluding Remarks 85

Application: Correlated Debye model for atomic motions in metal nanocrystals 87
4.1 Introduction 87
4.2 Mean square displacement and traditional Correlated Debye model 88
4.3 Correlated Debye model in finite crystalline domains 96
4.4 Testing the Correlated Debye model 101
4.5 Experimental 114
4.6 Concluding Remarks 116
Application: Vibrational properties of Pd nanocubes 119
5.1 Introduction 119
5.2 Experimental 120
5.3 Atomistic Modelling 123
5.3.1 Molecular Dynamics, MSD and MSRD 123
5.3.2 Modelling the MSRD components 127
5.4 Results & Discussion 132
5.5 Concluding Remarks 135
Final Conclusions 137
Appendix 139
7.1 Surface and Volume of truncated cube (with triangular facet {111}) 139
7.1.1 Surface: 142
7.1.2 Volume: 144
7.2 Details on Truncation 147
7.3 Warren Plot calculated from Molecular Dynamics Trajectories 150
References 153
List of Publications 165
Acknowledgments 167

LIST OF ABBREVIATIONS AND ACRONYMS

CD	Correlated Debye
DCF	Displacement Correlation Function
DW	Debye-Waller
EAM	Embedded Atom Method
EXAFS	Extended X-Ray Absorption Fine Structure
IP	Instrumental Profile
MD	Molecular Dynamics
MSD	Mean Square Displacement
MSRD	Mean Square Relative Displacement
NLLS	Non Linear Least Squares
PBC	Periodic Boundary Conditions
PDF	Pair Distribution Function
RMSRD	Root Mean Square Relative Displacement
RPDF	Radial Paird Distribution Function
RT	Room Temperature
Θ_D	Debye Temperature
TDS	Thermal Diffuse Scattering
TEM	Transmission Electron Microscopy
VDOS	Vibrational Density of States
WP	Warren's Plots
WPPM	Whole Powder Diffraction Method
WSS	Weighted Sum of Squares
XFEL	X-Ray Free Electron Laser
XRD	X-Ray Diffraction
XRPD	X-Ray Powder Diffraction

MOTIVATION AND METHODOLOGY

1.1 INTRODUCTION

The atomic mean square displacement (MSD, $\overline{\sigma_i^2}$) is often used in computational materials science studies to calculate measurable properties from the atomic trajectories of simulations; for example, the diffusion coefficient, which according to Einstein relations (Einstein 1905) on the random walk is 1/6 of the slope of the trend of $\overline{\sigma_i^2}$ vs. time (Chandler 1987). Equally relevant is the mean square relative displacement (MSRD, $\overline{\sigma_{ij}^2}$), used in X-ray Spectroscopies, mainly EXAFS, to describe the atomic disorder in solids (Calvin 2013) (Fornasini 2014).

Less known is the relevance of the MSRD in X-ray scattering from nanoparticles. In particular, in Total Scattering methods (Pair Distribution Function and Debye Scattering Equation), which rely on an atomistic description of the nanoparticles, the MSRD is the key to distinguish *dynamic* (thermal) and *static* disorder (Krivoglaz 1969) (Kuhs 2006). Interestingly, the trend of the MRSD with the distance is characteristic of the nanoparticle shape, an aspect investigated in some detail in this Thesis work. More generally it can be shown that beyond the expected effect of nanocrystal size, the shape alters the contribution of the surface, which is quite relevant for the MSRD. The importance of the shape and of the surface region holds also in case of clusters of nanoparticles, not only in isolated particles.

Besides the MSRD, the atomic configurations simulated by molecular dynamics (MD) can also be used to calculate the so-called Warren plot (or diagram), originally introduced in the seminal work of Warren & Averbach of the '50s to describe the effects of plastic deformation in metals (Warren B.E. 1950). Recent work has shown how to obtain Warren plots from the analysis of the diffraction line profiles according to the Whole Powder Pattern Modelling (WPPM) (L. M. Scardi P. 2002) (Scardi P 2017) (P. E.-W. Scardi 2018), in particular from the analysis of the strain component of the diffraction peak profile broadening. As proposed in this work, If the Warren plot can be

calculated directly from MD simulations, then it is possible to proceed backwards, and construct more reliable strain functions from an atomistic knowledge of the local atomic displacement caused by static and dynamic disorder components.

This thesis is divided in two main parts, discussing two different but complementary topics:

(i) atomistic modelling and calculations of displacement quantities,
(ii) application of the above results to experimental case studies, based on the modelling of diffraction data from nanocrystalline systems.

We start by describing the atomistic simulations and vibrational properties calculated for several atomic configurations. The main case study concerns Palladium nanoparticles of different sizes and shapes, for which we show that vibrational properties and correlation properties between atoms pairs are greatly influenced by the geometric shape of the nanoparticle and to a lesser extent by their size. The interest is on truncated cubes, i.e. cubes whose edges and corners are progressively removed, as in the series of so-called Wulff solids, ranging from the cubic to the octahedral shape (Wulff G. 1901). As shown in (ii), these are the object of several experimental studies.

The developed methodologies are nevertheless applicable to other cases, like the clusters of nanocrystals observed in powders produced by high-energy ball milling, which is also a topic discussed in (ii).

The work aims to show a general approach to atomistic modelling, both for isolated nanoparticles with definite shapes, and grains of unspecified shape in plastically deformed polycrystalline materials. We then use the values for displacement quantities (e.g., MSD, MSRD) calculated for the simulated systems to compare them to the experimental results. An underlying fact that seems to hold in all the different cases is that the surface behaviour of nanomaterials has the largest influence on the displacement quantities. For isolated particles we observe strong correlation between displacement quantities and the shape; whereas in the case of a nanocrystalline grain

clusters (Figure 1-1) we see that no matter the defects inside the grain, the main contribution to MSRD is given by the grain boundary.

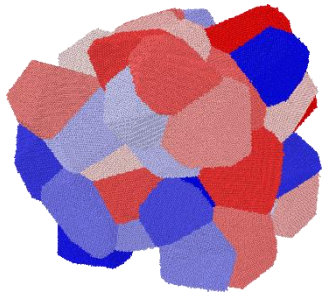

Figure 1-1

An example of simulated cluster of nanocrystalline FeMo alloy. Colours are used to identify the different domains.

(Scardi P 2017)

1.2 NANOPARTICLES AND CATALYSIS

Catalytic properties are enhanced in materials at the nanoscale. The smaller the size of the particle, the larger the surface to volume ratio, meaning that a higher number of atoms are sub-coordinated. Not only small nanoparticles have a larger percentage of atoms on the surface, but in the case of anisotropic shapes (like rods, octahedrons and cubes) different coordination numbers can be found for different sectors of the surface. It is important to know what direction the faces of a geometrical shape are orientated with respect to the crystalline arrangement. In fact, most of the times the morphology of a nanocrystal follows the packing arrangement of atoms. This means that symmetry elements of the constituting lattice are also properties of the overall polyhedral shape. A cube-shaped nanocrystal has the faces parallel to the crystallographic planes {100}. Same goes for octahedral faces that are parallel to the {111} planes.

Heterogeneous catalysis is proved to be directly dependant on the nanocrystal shape, and on the surfaces exposed to the external world. The coordination number of atoms on differently orientated surfaces changes, and therefore the electron density too. As a consequence, catalytic activity for different reactions changes whether it takes place on a cube's or on an octahedron's surface (Long Ran 2013).

A number of studies address this specific topic, i.e., how the catalytic action depends on the type and extension of the exposed facets, i.e. the amount of a certain type of surface exposed to the environment (e.g., see (Rao 2007) (Kwangjin An 2012) (Yan Zhou 2018)). However, a recent work (Luo Mingchuan 2017) shows that particles with an overall "similar" shape can however perform differently as catalysts, depending on the surface strain, i.e. the degree of deformation of the surface compared to an ideal shape.

The geometry of a nanoparticle proved to be important, with the following points of interest:

- Metal nanoparticles in catalysts are deposited on a layer or immersed in some capping agent or solvent, in order to protect and prevent nanoparticles from lumping together.

- The surface effects are more or less influent depending on the shape under investigation. This means that some shapes will deform, geometrical faces will get convex or concave depending on the shape itself.
- The thermal effects always exist, as atom always vibrate about an equilibrium position, but vibration modes and amplitude change with size and shape of the nanocrystals.

In the end it is not sufficient to study different shapes at the nanoscale, as the effects on the atomic disorder (as a function of shape and size) should be quantified, taking into account both the thermal and the structural components of the disorder in the atomic arrangement. The MSRDis a quantity well suited for the task and it will be one of the main tools to investigate nanocrystals by atomistic simulations.

In particular, the present work focuses on Palladium nanocrystals, which are well known for their catalytic properties. Modern synthesis techniques allow the production of precise shapes with narrow size distribution, i.e. almost monodispersed Pd nanocrystals of almost identical shape. (Wenxin Niu 2011) (Jiawei Zhang 2016)

Our aim is to simulate Pd nanoparticles using MD (see next paragraph). The first step consists in defining the virtual structure to be simulated by fixing atomic positions in space. This is done by carving geometrical shapes out from a large lattice of palladium atoms in ideal crystallographic positions, i.e. evenly spaced according the *fcc* crystal structure with unit cell parameter a=3.89 Å, which is an average of bulk Pd lattice parameter, chosen in order to have a plausible starting value for the simulations.

The nanoparticle shapes illustrated in this work are *spheres* (a *de facto* standard shape when testing models or calculations, even if not so frequent in real applications) and especially *truncated cubes*. The size ranges from 40 to 150 Å of the particle shape linear dimension (diameter in case of spheres, cube edge for truncated cubes).

These sizes involve numbers of atoms ranging from about 3600 (cube edge 40 Å) to roughly 230.000 (cube edge 150 Å). The computational complexity for the MD simulation is approximately of the order $O(N^2)O(t)$ (depending on the cut-off distance of the employed interatomic potential), i.e. it scales linearly with the time of simulation and quadratically with the number of atoms. Additional computational complexities arise when analysing the trajectories in phase space, as it will be shown in coming paragraphs. Therefore, maximum size for the nanoparticles described in the current work is partly dictated by the above mentioned computational limitations, but it is also related to the heterogeneous catalysis applications. In fact, as stated previously, the nanoparticle specific effects (catalytic properties among them) are relevant for small aggregates, and the computational limitation does not hinder the results.

With the term "truncated cubes", we refer to those Wulff solids one can generate from progressively removing vertices and edges to a cube. Specifically: *truncated cube with triangular corner facet* are cubes where edges and vertices are partly removed. The removal is progressive and made in such a way that the facet orthogonal to the cube diagonal is always of a triangular shape. (See Appendix).

The reason for choosing truncated cubes is twofold: on one hand the changing truncation allows to span the whole spectrum of possible shapes from a cube to an octahedron (Wulff solids), dealing therefore with a full family of geometrical solids by adjusting one parameter only; on the other hand palladium cubes can be grown in laboratory with controlled shape, and Transmission Electron Microscopy (TEM) shows that their actual shape closely resembles a cube with blunted edges and corners. Such 'smearing' of the perfect cube reference shape is an effect of surface energy minimization, which tends to remove atoms from high-energy / low coordination positions like sharp corners and edges (e.g., see Figure 8 in (Blazhynska M. M. 2018)).

One can systematically run from a cube to an octahedron by changing a single parameter: the truncation value. A number $\mathrm{p} \in [0,1]$ (Figure 1-2) is defined such that p=0 is a cube of edge l, and p=1 is an octahedron of edge $\mathrm{a} = \mathrm{l}/\sqrt{2}$. (Figure 1-3)

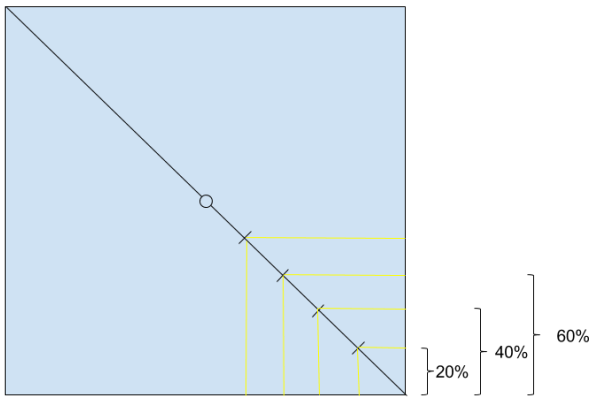

Figure 1-2

Naming convention for different degrees of truncation is based on the fractions of the face diagonal.

A cube corresponds to a truncation value of 0%, while 100% truncation yields an octahedron.

All the particle renderings in figures are made with OVITO (Stukowski A. 2010).

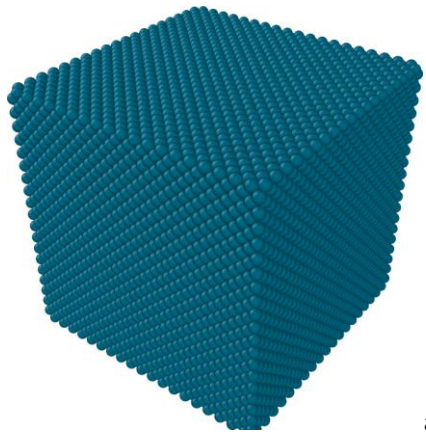

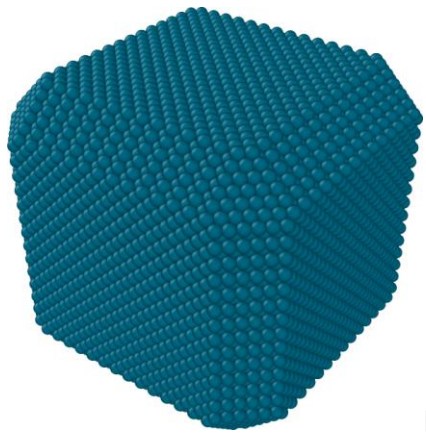

Figure 1-3

Nanoparticles with three different degrees of truncation:

a) Truncation 0% (p = 0)

b) Truncation 30% (p = 0.3)

c) *Truncation 98% (p = 0.98)*

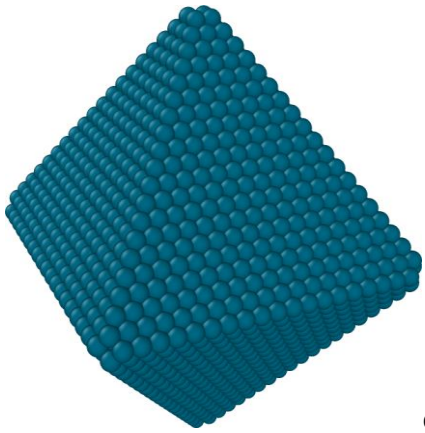

c)

This kind of truncation is obtained by defining 3 points (the vertices of the triangular facets) for each cube vertex for a total of 24 points (Figure 1-4). The convex volume delimited by the 24 point defines the **truncated cube**.

If the cube is centred in the origin, **cube** vertices are in positions $(\pm l/2, \ \pm l/2, \ \pm l/2)$. One can just focus on the $x > 0, \ y > 0, z > 0$ region, thus leaving 7 regions with identical properties. Let us call this subsection of the cube **eighth of truncated cube**.

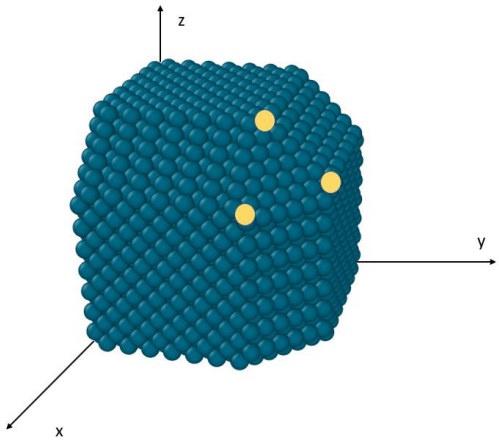

Figure 1-4

The three delimiting points. For every cube vertex three similar points are defined. The particle will be the space region (maximum convex volume) delimited by the planes containing all 24 points.

In this region, the facet vertices are in positions:

$$v_1 = (\mathrm{l}(1-\mathrm{p})/2,\ \mathrm{l}/2,\ \mathrm{l}(1-\mathrm{p})/2)$$
$$v_2 = (\mathrm{l}/2,\ \mathrm{l}(1-\mathrm{p})/2,\ \mathrm{l}(1-\mathrm{p})/2)$$
$$v_3 = (\mathrm{l}(1-\mathrm{p})/2,\ \mathrm{l}(1-\mathrm{p})/2,\ \mathrm{l}/2)$$

(1-1)

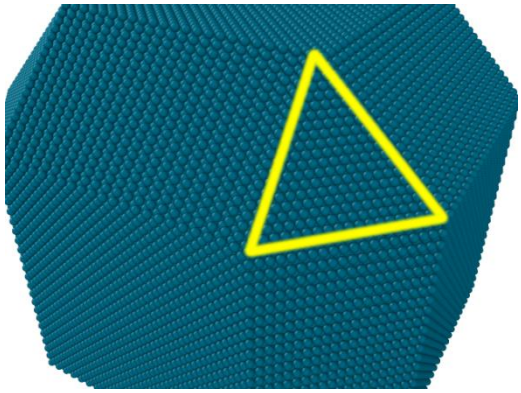

Figure 1-5

The triangular facet along the direction [111]

More details in the Appendix.

1.3 MOLECULAR DYNAMICS

Molecular Dynamics provides numerical models of nanocrystals based on the solution of the equation of motion for all the atoms in the given atomic or molecular system (Allen M.P. 1989) (Rapaport 2004). As such, MD is the numerical realization of what has historically been the domain of Statistical Mechanics, since the configuration (and phase) space of the system under investigation can be simulated, i.e. the *6N* values for position and velocity of the N atoms.

Two ingredients are needed to obtain atom trajectories in time: a suitable model for the interaction potential and high computational capabilities, in order to simulate large systems for long enough periods of time. Since the equations of motion must be solved numerically, a discretization of the continuous solution is required and the choice for the time step duration and overall time scale is important. For each atom in the system the trajectory can be calculated as solution of the Newton's equations of motion:

$$m_i \frac{d^2 \boldsymbol{r_i}}{dt^2} = \boldsymbol{f}_i(\boldsymbol{r}_i); \tag{1-2}$$

With forces acting on each atom obtained from the potential energy:

$$\boldsymbol{f_i}(\boldsymbol{r}_i) = -\frac{\partial}{\partial \boldsymbol{r_i}} \boldsymbol{U}(\boldsymbol{r}_i). \tag{1-3}$$

The potential energy, in general, is a sum of many terms. The zeroth term, usually called "external field", is a function of the atom positions only (r_i). Following terms are the "many-body terms" starting from two-body, i.e. the interaction between the i-th atom with the other atoms (potentially all N-1 depending on the interaction range), then adding increasingly more complex interactions:

$$\mathcal{U}(\boldsymbol{r}_i) = \sum_{i=1}^{N} v_1(\boldsymbol{r}_i) + \sum_{i,j=1}^{N} v_{12}(\boldsymbol{r}_i, \boldsymbol{r}_j) + \sum_{i,j,k=1}^{N} v_{123}(\boldsymbol{r}_i, \boldsymbol{r}_j, \boldsymbol{r}_k) + \cdots \tag{1-4}$$

Once a suitable potential is chosen, the trajectory for each atom is calculated at discrete intervals of time (timesteps) by solving (1-2) with an integration algorithm (for example Verlet algorithm, *leap-frog*, velocity-Verlet, see (Thijssen 2007) and references therein).

Modern computers allow the calculation, in a matter of hours, of trajectories of ten thousands of atoms for a simulation time of several nanoseconds, which is deemed appropriate to study several physical properties (Sheng H. 2018). In particular the timestep for simulation should be chosen as some orders of magnitude smaller than the reciprocal of the highest frequency of motion (Rapaport 2004) (Tuckerman 2010), while the overall timescale (the duration in "real time") should be enough to sample a suitable number of statistically uncorrelated configurations of the system (Allen M.P. 1989). For Palladium, the maximum frequencies are on the order of $THz = 10^{12}\ s^{-1}$ (Miller A. P. 1968) (Miller A.P. 1971), therefore the integration timestep is chosen to be $1\ fs = 10^{15}\ s$ and the time for the simulation is at least $0.5\ ns = 0.5 \cdot 10^{-9} s$.

Interaction potentials range from simple models with few phenomenological parameters, like the Lennard-Jones potential:

$$\mathcal{U}_{\mathcal{LJ}}(\boldsymbol{r}_{ij}) = 4\epsilon \left[\left(\frac{\sigma}{\boldsymbol{r}_{ij}} \right)^{12} - \left(\frac{\sigma}{\boldsymbol{r}_{ij}} \right)^{6} \right], \tag{1-5}$$

to complex molecular potential with ab-initio calculated parameters (like ReaxFF) (van Duin A.C.T. 2001). A common choice for metallic materials is the Embedded-Atom Method (EAM) (Daw 1983) (Daw 1984) potential, defined as (Lee 2011):

$$\mathcal{U}_{\mathcal{EAM}} = \sum_{i \neq j} U_{ij}(\boldsymbol{r}_{ij}) + \sum_{i} F_i(\rho_i). \tag{1-6}$$

The EAM parameters are fitted against simulations of "bulk" materials, so they are chosen to better represent bulk properties. For this reason it is still source

of debate whether using an EAM potential for the simulation of isolated nanoparticles can give reasonable results, and corrections to the EAM scheme have been proposed to overcome such limitations (especially the treatment of surface) (Zhou L. G. 2012).

The EAM potential is composed of a repulsive term U_{ij} and a functional of the electron density (ρ_i), $F(\rho_i)$. In the Embedded-Atom case, the functional form is deduced semi-empirically and in part by fitting to esperiments. One of the objectives of the present work is to investigate the validity of such a choice, also to provide indications for possible future developments, to support a better agreement between simulations and experiment.

Before discussing the use of MD, we need to present some other ingredients used throughout the work. For the time being we just underline that the result of an MD simulation is a collection of atomic coordinates (frames) evenly sampled at different times during the simulation of the system. The whole output of coordinates at different times is called a **trajectory**, borrowing the term from classical mechanics, even if these are discrete (in time) trajectories and not continuous.

In the current work, Molecular Dynamics calculations have been performed with the open source software LAMMPS. Originally developed in 1995 (Plimpton 1995), LAMMPS has been constantly upgraded and supported and it is still one of the best and widely used software for MD simulations (See https://lammps.sandia.gov/papers.html (Sandia National Laboratiries n.d.)).

1.3.1 MSRD and RPDF

Once the atomic trajectories for a nanoparticle are obtained from MD, it is necessary to identify a quantity that can be measured on the virtual sample. The aim is to determine properties of the shape and surface of the particle. MD provides the position of all N atoms, $\boldsymbol{r_i(t)}$, with *t* as the sampling time for the coordinates. The distance of all pairs of atoms, i.e. the distance vector between i-th and j-th atoms, is:

$$\boldsymbol{r_{ij}(t) = r_i(t) - r_j(t).} \qquad (1\text{-}7)$$

Atomic trajectories are simulated by MD for a certain amount of time, usually of the order of nanoseconds; one can therefore calculate time-average positions of each atom, as well as the time-average distance between each pair of atoms, defined respectively as:

$$\overline{\boldsymbol{r_i}} = \frac{1}{T}\int_0^T \boldsymbol{r}_i(t)dt, \tag{1-8}$$

$$\overline{\boldsymbol{r_{ij}}} = \frac{1}{T}\int_0^T [\boldsymbol{r}_i(t) - \boldsymbol{r}_j(t)]dt. \tag{1-9}$$

The variance of each pair distance with respect to the time average is also of interest:

$$\overline{\sigma_{ij}^2} = \overline{\left(\boldsymbol{r_{ij}(t)} - \overline{\boldsymbol{r_{ij}}}\right)^2}. \tag{1-10}$$

This quantity is the mean square relative displacement and it is a measure of the correlation between positions of two atoms. The higher the value of $\overline{\sigma_{ij}^2}$ for a pair *ij*, the lower the correlation. As already mentioned in the previous section, the MSRD is a suitable quantity to understand the atomic disorder, i.e. the displacement of atoms from an idealized position (mainly) due to temperature and finite size of the nanocrystal (structural distortion).

When considered with respect to larger values of interatomic distance $\boldsymbol{r_{ij}}$ (which correspond to atoms on opposite facets), the MSRD can display what is happening on the surface of the nanoparticle, thus allowing a classification of different sizes and shape of nanoparticles, according to their "surface behaviour" (i.e. the different MSRD).

However, the MSRD is a computationally demanding quantity. A possible solution is to use already optimized codes to calculate a related quantity: the Radial Pair Distribution Function (RPDF), also indicated with *g(r)*.

The RPDF can be readily calculated from molecular dynamics trajectories and it is defined as:

$$\mathrm{g}(r) = \lim_{dr \to 0} \frac{p(r)}{4\pi\left(N_{pairs}/V\right)r^2 dr}. \qquad (1\text{-}11)$$

With *p(r)* being the average number of atom pairs with distance between *r* and *r+dr* (Figure 1-6), V total volume of the system, N_{pairs} number of unique atom pairs in the system, i.e.

$$N_{pairs} = \frac{N(N-1)}{2}, \qquad (1\text{-}12)$$

In the limit of $\mathrm{dr} \to 0$ the number of atom pairs *p(r)* is just

$$\mathrm{p}(\boldsymbol{r}) = \sum_{i,j \in N;\, i \neq j} \delta\left(\boldsymbol{r} - \boldsymbol{r}_{ij}\right) \qquad (1\text{-}13)$$

Where the Dirac's Delta is used to count the number of pairs of atoms at distance ***r***.

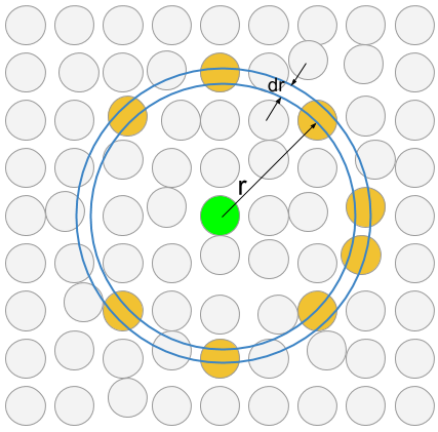

Figure 1-6

Two dimensional projection of a spherical shell of radius r and thickness dr.

The function in eq. (1-13) selects only the atoms with center inside the shell.

The set of all atoms lying at a certain distance forms a shell of atoms, aka the *coordination shell*. These shells are not to be interpreted as physical shells with respect to an origin point.

The typical RPDF for a metal particle is as shown in Figure 1-7.

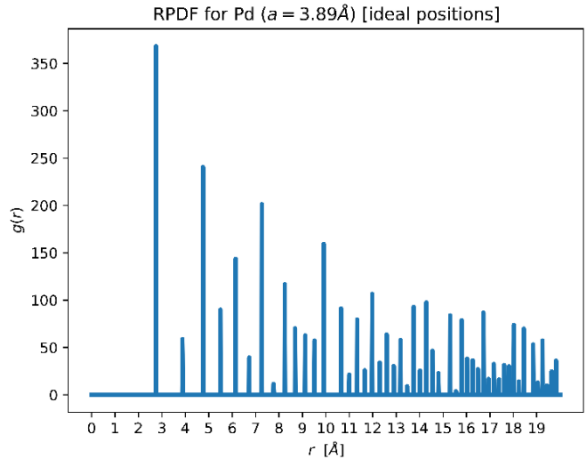

a)

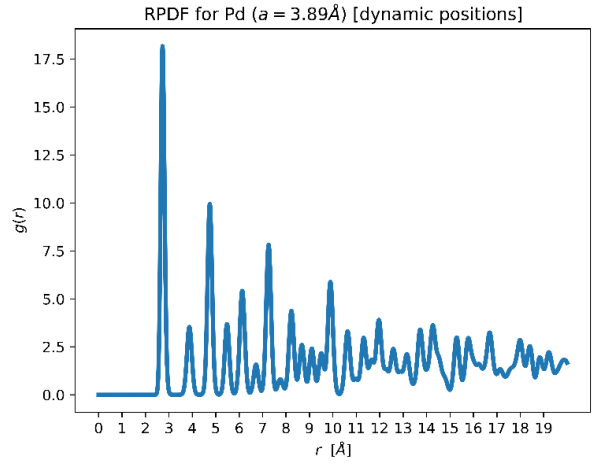

b)

Figure 1-7

a) The RPDF of the ideal configuration. The atoms are in fixed crystallographic positions. The peaks have zero width.

b) After the Relaxation, averaging in time the RPDF, we obtain the distribution of atoms pairs distances.

In the case of an ideal (perfect) crystal, the peaks of the RPDF are Dirac's deltas, i.e. infinitely narrow: dispersion of values around the Dirac's delta is represented by the MSRD discussed earlier.

Existing algorithms (Levine (2011)) can be used to calculate the RPDF and then fit each peak to extract the MSRD. This procedure is applicable only to objects in a crystalline form, where it is easy to connect different peaks to different coordination shells and it works only for the inner coordination cells, as with the increasing distance the overlapping of the peaks makes the separation of single shell contributions unreliable.

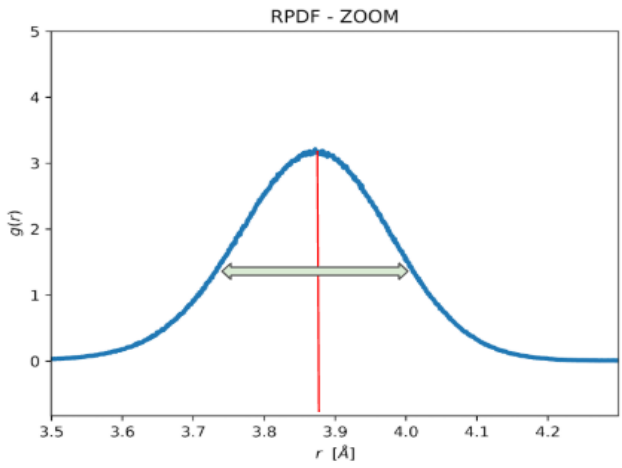

Figure 1-8

An example of RPDF peak. Zoom on the 2nd nearest neighbours shell, i.e. the density of atoms pairs at distance around 3.89 Å.

The Mean Square Relative Displacement (eq. (1-10)) is the variance of the curve. In case of a Gaussian fit, the variance of the curve is a good approximation of the MSRD value for all pairs belonging to the 2nd neighbours shell.

1.3.2 Molecular Dynamics in practice:

It is important to define which system states can be simulated by MD and the differences between them:

- Starting from an ***ideal*** configuration (i.e. a set of atoms arranged according to a perfect crystallographic structure) the simulation first generates a ***relaxed*** configuration of a nanocrystal, where atoms are shifted to the minimum energy configuration. Atoms are allowed to "feel" each other *through* the chosen potential (here the EAM potential previously discussed). The Hamiltonian at this step comprises of the Kinetic and Potential Term.

- After this first minimization step, the system is virtually put in contact with a heat bath (reservoir) and brought to room temperature. In the Hamiltonian of the system a new term is added, i.e. a thermostat function of the conjugated variables (position and momentum) and temperature.
- Finally, the system is left isolated for a suitably long period of time (typically, not less than 0.5-1 ns) and time-frames of the atomic configurations are saved periodically (usually a snapshot of the system configuration every picosecond). These time-frames are called ***dynamic*** frames. The collection of all these frames, sampled at different times, constitutes the *atoms* trajectories. In this case the system is considered isolated (micro canonical ensemble in statistical mechanics terms), and the thermostat term is absent in the Hamiltonian.
- The time average position of the atoms during the dynamic phase is called ***average dynamic***. This can be calculated by averaging the positions of atoms during the *dynamic* phase.

Every quantity to be measured on the system can be calculated in the four aforementioned configurations:

- ideal,
- relaxed,
- dynamic,
- and average-dynamic.

Every quantity measured on a simulated nanoparticle must be represented as a function of the system coordinates (positions, velocities, magnetic moment, etc). The simplest case is a quantity that depends on the atomic positions $\boldsymbol{r}_i$ of all atoms. The same quantity can be calculated differently, yielding different averages, by using atomic coordinates from the four configurations described above. For example, a quantity that is represented by a function:

$$\mathrm{f(t)} \equiv f\big(\boldsymbol{r}(\mathbf{t})\big). \qquad (1\text{-}14)$$

Can be calculated on the time average positions (average-dynamic configuration), thus being independent of time:

$$\mathrm{f} \equiv f(\bar{\boldsymbol{r}}). \tag{1-15}$$

Or it can be calculated along the trajectory and then time averaged:

$$\overline{f(\boldsymbol{r})} = \frac{1}{T}\int_0^T f\big(\boldsymbol{r}(\boldsymbol{\tau})\big)d(\tau). \tag{1-16}$$

At the same time, the spatial average can be defined, i.e. the average for all atoms with a certain property. For example, we can define the indices of atoms that are contained in a spherical volume of radius ρ:

$$\mathrm{V} = \{i : |r_i| < \rho\}; \tag{1-17}$$

And calculate a quantity averaged only on the atoms in the volume:

$$\langle f(\boldsymbol{t})\rangle_V = \sum_{i \in V} f(\boldsymbol{r}_i; t). \tag{1-18}$$

To better show the difference among the four configurations, see the quantities shown in Figure 1-9 for a typical case study of a metal nanocrystal.

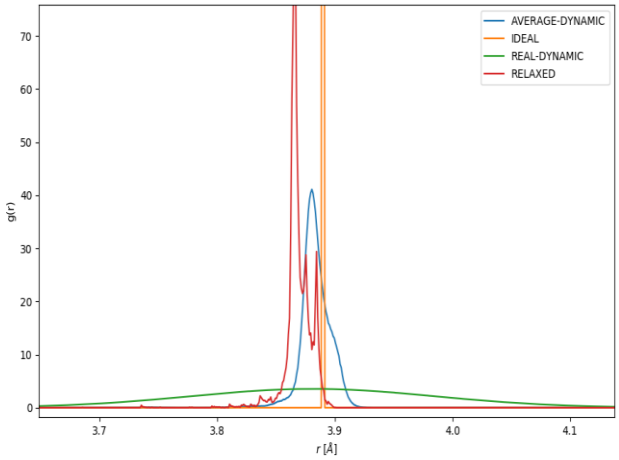

Figure 1-9

Detail of the RPDF of a Pd nanoparticle for the second coordination shell. The ideal configuration gives a sharp peak, since all atoms belonging to the shell are at the same ideal distance of 3.89 Å

Note that the "real-dynamic" RPDF refers to the average of RPDFs calculated at each frame during the dynamic phase. This accounts for the fact that observation times of X-ray spectroscopic and scattering techniques (in this study, X-Ray Diffraction in particular) are much longer than the typical vibrational frequencies. Even with the most modern X-ray Free Electron Lasers (X-FELs), X-rays are 'fast probes', such that the observation involves a time-averaging process over a large number of time-frames.

A more detailed discussion of the curves in Figure 1-9 is presented in the next paragraph.

1.4 STATIC AND DYNAMIC DISORDER

1.4.1 A full Mean Square Radial Displacement calculation

The RPDF in Figure 1-9 is a good starting point to define ***static*** and ***dynamic*** *disorder* (the latter not to be confused with the dynamic configuration of a MD simulation, even if the two concepts are indeed related). In the current context dislocations are not considered or any other strong strain field: all the atomic displacements with respect to an ideal (crystallographic) configuration are due to the interatomic potential and to the thermal motion introduced in the simulation as explained above.

Every source of deviation from an ideal configuration is considered disorder. Static disorder can be seen in the RPDF for the relaxed configuration, as an effect of the "shrinking" of atomic distances caused by the finite size of the particle and the sub-coordination of surface atoms, evident from the shift of the center of the peak. It is worth noting here, in pass, that the occurrence of a shrinkage or expansion of atomic distances (or absence of variation) depends on the atomic species and, to some extent, on the atomic potential used (see discussion about different potential in 7.3).

Temperature is also responsible for a static component, related to thermal expansion, that can be spotted in the RPDF of the average-dynamic configuration. The largest effect, however, is the dynamic disorder due to the thermal vibration of atoms about the equilibrium position, clearly visible for the real-dynamic configuration of the RPDF, showing a broad peak. These definitions are not uniformly used and accepted in the context of the different X-ray spectroscopies. For example, in EXAFS literature the sources of disorder are sometimes divided into *structural* and *thermal* (containing both the static and the dynamic contribution due to temperature) components (Krivoglaz 1969) (Lonsdale 1968).

At this point, given the atom trajectories and the ability to take both time and spatial averages, we analyse the connection to the experiments. The (single

atom) displacement is a time-dependent feature of each atom in the real dynamic configuration:

$$\boldsymbol{\sigma}_i(t) = \boldsymbol{r}_i(t) - \bar{\boldsymbol{r}}_i, \tag{1-19}$$

where $\mathrm{r_i(t)}$ denotes the position of the *i*-th atom at time *t* and $\bar{\boldsymbol{r}}_\iota$ is the time average position of the *i*-th atom during the whole dynamic evolution. By defining the distance of two atoms at time *t* as $\mathbf{r_{ij}(t) = r_i(t) - r_j(t)}$, the pair displacement of atoms *i* and *j* can be expressed as:

$$\boldsymbol{\sigma}_{ij} = \boldsymbol{r}_{ij}(t) - \bar{\boldsymbol{r}}_{ij}. \tag{1-20}$$

The squared time-averages of the two quantities $\overline{\boldsymbol{\sigma^2}_\iota(t)}$ and $\overline{\boldsymbol{\sigma^2}_{\iota J}(t)}$ are respectively the MSD and the MSRD, as it has already been shown in the previous section. The two quantities can be connected, since the MSRD can be written in terms of single-atom contributions ($\overline{\sigma_\iota^2}$) and a correlation term ($\overline{\sigma_\iota \cdot \sigma_J}$) (a. L. Scardi P. 2016) (Jeong I.-K. 1999):

$$\overline{\sigma_{\iota J}^2} = \overline{\sigma_\iota^2} + \overline{\sigma_J^2} - 2\,\overline{\sigma_\iota \cdot \sigma_J}. \tag{1-21}$$

In the EXAFS literature this is most often written as (Fornasini 2014) (Calvin 2013)

$$\mathrm{MSRD}_{AB} = MSD_A + MSD_B - 2DCF, \tag{1-22}$$

where the correlation term is called Displacement Correlation Function (DCF). When dealing with monoatomic metals, (1-22) can be further simplified by using the approximation $\overline{\sigma_\iota^2} \approx \overline{\sigma_J^2}$

$$\overline{\sigma_{\iota J}^2} = 2\,\overline{\sigma_\iota^2} - 2\,\overline{\sigma_\iota \cdot \sigma_J}. \tag{1-23}$$

Calculating the MSRD from the RPDF is computationally advantageous but is unreliable if it is necessary to analyse the MSRD for each the possible pair

distances. The radial distribution, in fact, presents broad and overlapping peaks for large distances. This requires a direct calculation of the MSRD. In doing so different versions of the MSRD function have been constructed, each of them able to single out different contribution to disorder.

First, let us define a coordination shell, by labelling the atoms that (before MD simulation) belonged to the same shell. To do so one uses the coordinates of the ideal configuration, $\boldsymbol{r}_{i;I}$, where the capital "I" indicates the ideal system. A shell of atoms at distance R is then defined as the set of indices whose atoms satisfy the distance condition:

$$S_R = \{i, j: \|\boldsymbol{r}_{i;I} - \boldsymbol{r}_{j;I}\| = R\}. \quad (1\text{-}24)$$

r [Å]	*Number of pairs*
2.750	*38940*
3.89	*18866*
4.764	*73488*

Table 1 *Number of atom pairs in the first three coordination shells for a fcc Pd sphere of 7000 atoms. Radius (R) is in Å*

From the definition of equation (1-22), for any two (i-th and j-th) atoms

$$\overline{\sigma_{ij}^2} = \overline{\left(\boldsymbol{r}_{ij}(\boldsymbol{t}) - \overline{\boldsymbol{r}_{ij}}\right)^2}, \quad (1\text{-}25)$$

the MSRD can be written as a function of the coordination shells radius by taking the shell average of (1-22):

$$\overline{\sigma_{S_R}^2}(r) = \frac{1}{N_S} \sum_{i,j \in S_R} \overline{\sigma_{ij}^2} = < \overline{\sigma_{ij}^2} > \quad (1\text{-}26)$$

or

$$\overline{\sigma_{S_R}^2}(r) = < \overline{\sigma_{ij}^2} >. \quad (1\text{-}27)$$

We denote the time average with the BAR and shell average with the BRACKETS.

In paragraph 1.3.1 it has been shown how the MSRD can be obtained, directly from the RPDF, by fitting the RPDF peaks with Gaussian functions, the variance of which is a good estimate of the MSRD (Figure 1-8). Although efficient, this way of calculating the MSRD has evident limitations. The assumption that the RPDF peaks have a Gaussian shapes, even if qualitatively good is not entirely correct, since the peaks may be asymmetric (as seen in Figure 1-9 for the Average-Dynamic case), and the trend of the tail region can generally be different from the Gaussian profile. Moreover, only the first peaks are far apart enough to be fitted individually (as seen in Figure 1-7 b); beyond the first ~15 peaks it becomes difficult to separate unequivocally what contribution to the MSRD is due to which peak, due to their increasingly more complex overlapping.

As an alternative we propose in this Thesis work, by resorting to the molecular dynamics positions and using equation (1-26) the MSRD can be calculated numerically for all coordination shells. The downside of this direct calculation is the computational complexity: for a system of N atoms, the number of pairs to calculate is $N(N-1)/2$, and the calculation should be made for a meaningful number of time frames (usually several hundreds to have a realistic time average). In the following we show details and applications of this approach.

1.4.2 Separation of static and dynamic contributions to disorder

As shown so far, MSRD is obtained without particular assumptions from MD simulations. To get separate information on the components of the MSRD we must instead use appropriate averages and approximations. The *static displacement component* of the MSRD, ${\delta_{S_R}}^2(r)$, accounts for the deviation of distances of pairs from the average value for all pairs in a shell. This is obtained from the average-dynamic configuration, thus removing (almost completely) the effect of the thermal contribution:

$$\delta_{S_R}{}^2(r) = \frac{1}{N_S}\sum_{i,i\in S_R}\left(\overline{\boldsymbol{r_{ij}}} - \frac{1}{N_S}\sum_{i,i\in S_R}\overline{\boldsymbol{r_{ij}}}\right)^2. \qquad (1\text{-}28)$$

Next step is to obtain the dynamic component of the MSRD. This can be done using equation 1-26, for the "full" MSRD, and 1-28, for the static component. Under the reasonable approximation that both components can be treated as independent Gaussian distributions, the dynamic (thermal) disorder component can be obtained as the difference of the previous two quantities. With simple algebraic manipulations it can be shown that:

$$\overline{\sigma_{SR}^2}(r) - \delta_{\mathrm{SR}}{}^2(r) = \langle\overline{\boldsymbol{r_{ij}^2}}\rangle - 2\cdot\langle\overline{\boldsymbol{r_{ij}}}^2\rangle + \langle\overline{\boldsymbol{r_{ij}}}\rangle^2. \qquad (1\text{-}29)$$

The quantity defined in (1-29) can be interpreted as the only thermal component. Figure 1-10 and Figure 1-11 show $\delta_{\mathrm{SR}}{}^2(r)$ for spheres and truncated cubes of various sizes. For the given nanoparticle shape the trend is nearly independent of the number of atoms. In particular, the maximum value of $\delta_{\mathrm{SR}}{}^2(r)$ is independent of the nanoparticle size, and shifts to larger distances for increasing sizes. This means that for very large nanocrystals, as in the bulk form of the material, the mean effect of $\delta_{\mathrm{SR}}{}^2(r)$ tends to disappear. In fact, the trend of the MSRD for a bulk is expected to tend asymptotically to twice the MSD value, when most pairs are made of atoms far enough to be considered uncorrelated (see eq. (1-23)).

It is interesting to note where the maximum values of $\delta_{\mathrm{SR}}{}^2(r)$ fall off. For spheres this happens for pair distances close but not equal to the diameter, whereas for truncated cubes the maximum falls off around the face-face distance (the truncated cube edge). In both cases this is the condition when pairs are made of one atom on the surface region (i.e., within 2-3 atomic layers from the very surface) and one far away, but within the "core" region, where surface effects are much weaker. Beyond the maximum the static MSRD decreases linearly to zero, rather steeply, for the longest distance in the nanoparticle. We also note the trend for truncated cubes in Figure 1-11 (a), is not as smooth and definite as in the spherical case, and maxima are higher in cubes than in spheres.

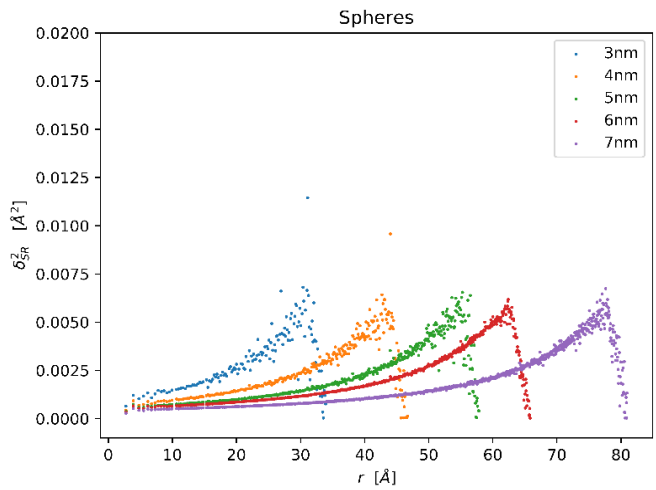

Figure 1-10

Values of $\delta_{SR}{}^2(r)$ for spheres of different sizes. The trend is similar, but "stretched" along the abscissae for the different diameters.

Nominal Edge Length	Number of atoms	Face-Face Distance
3 nm	1464	3.112 nm
4 nm	3660	4.668 nm
5 nm	6986	5.446 nm
6 nm	10204	6.1462 nm
7 nm	18924	7.78 nm

Table 2
Details of the nanoparticles in Figure 1-10

Looking at equation (1-23), in purely algebraic terms a decrease of $MSRD$ could stem both from an increase of ***DCF***, the correlation between the atoms pairs, or from a decrease of ***MSD***, the single atom mean square displacement.

In case of an increased correlation, this means long-distance interactions between atoms, which makes sense for pairs of atoms on opposite surfaces, which presumably behave in similar ways, thus leading to a low variance of the pair displacements. It is unlikely, instead, that the low MSRD for longest distances be due to a decreasing MSD, as on the contrary the surface atoms are presumably less constrained in their displacements than the atoms of inner shells.

The trend of the static MSRD for truncated nanocubes, which is the shape of main interest in the applications shown later on, follows approximately a polygonal chain (see the triangle of Figure 1-11 (b)). It is null for zero and beyond the maximum distance, which in a perfect cube would be the body diagonal ($\sqrt{3} \times l$, with l the edge length); whereas the projection of the vertex on the

base of the triangle falls approximately at the face-face distance. Given the nanocube size (edge length and truncation level) it is therefore possible to use a simple parametrization to approximate the trend of the static MSRD. Indeed, this possibility is explored in chapter 5 (page 119), where we put forward an approximate analytical expression for the MSRD.

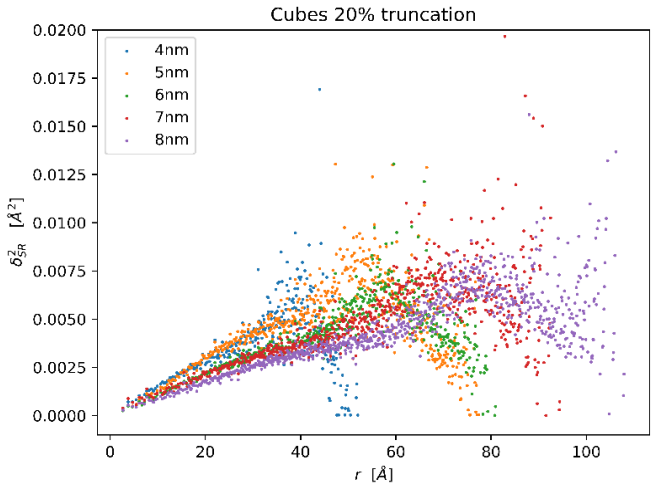

a)

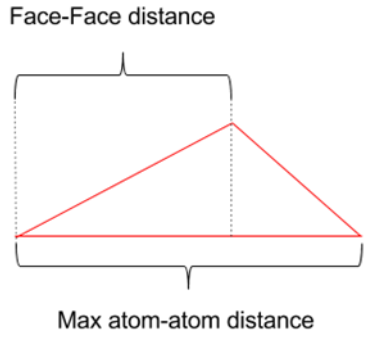

b)

Figure 1-11

a) *Values of $\delta_{SR}{}^2(r)$ for 20% truncated cubes of different sizes. The trend is similar, allthough more scattered than the spherical case (Figure 1-10).*

b) *Schematic sketch of the $\delta_{SR}{}^2(r)$ for a cubic nanoparticle, see text for details.*

Nominal Edge Length	Number of atoms	Face-Face Distance
4 nm	3638	3.8122 nm
5 nm	10715	5.446 nm
6 nm	12000	5.7572 nm
7 nm	18800	6.9242 nm
8 nm	27778	7.7022 nm

Table 3 Details of the nanoparticles in Figure 1-11

We can now analyse more closely the two contributions to the MSRD. The "full" MSRD is given by equation (1-26), whereas static and dynamic components are estimated from equations 1-28 and 1-29, respectively. Results are shown in Figure 1-12 for a sphere and Figure 1-13 for a truncated cube. Apart from the longest distances, the thermal component behaves as in bulk materials, raising gradually to a nearly constant value. In fact, it is in the first (innermost) coordination shells that atom vibrations are correlated, thus decreasing the MSRD. The effect of finite nanoparticle size is apparent for the longer distances, where the thermal component deviates from the uniform trend. This is clearly a consequence of surface atoms vibrating with larger amplitudes, but apart from those few distances the trend of the thermal component seems not much bound to the nanoparticle shape. It is mostly the size, which determines the mean value over the whole particle, as already proved with the recently proposed Correlated Debye model, modified to account for the finite domain size (F. A. Scardi P. 2018). Moreover, for any property derived from the MSRD and its components, the contribution of the individual coordination shells must be weighted on the number of pairs of atoms; as shown in Figure 1-12(b) and Figure 1-13(b), the weight of the longer distances, where the upward deviation of the MSRD is visible, is rather limited.

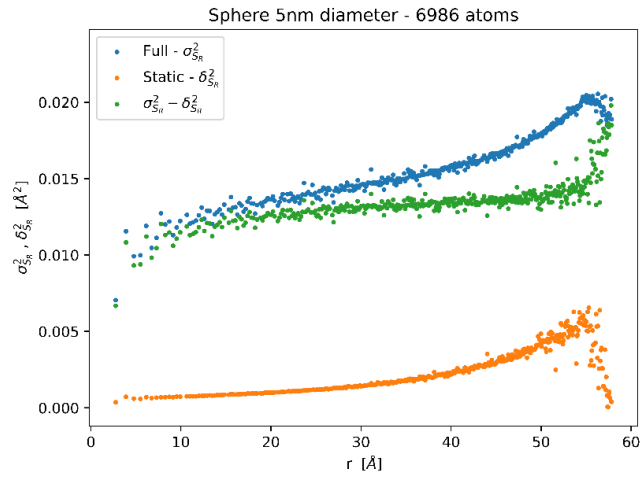

a)

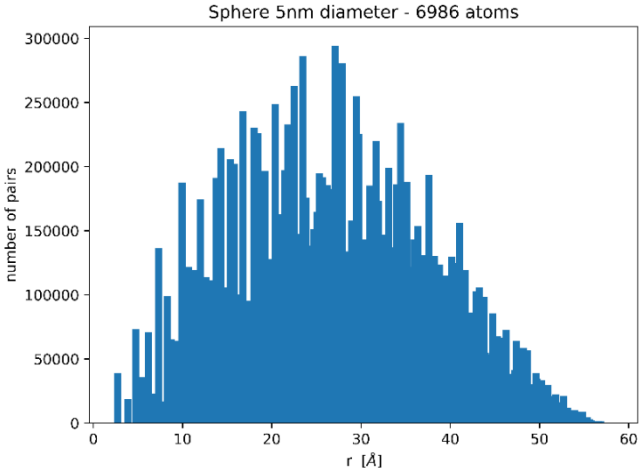

b)

Figure 1-12

MSRD components for a sphere of 6986 atoms.

a) The three components of Relative Displacement: static (orange), full (blue), difference of the two (green).

b) The corresponding number of pairs for each coordination shell of radius R.

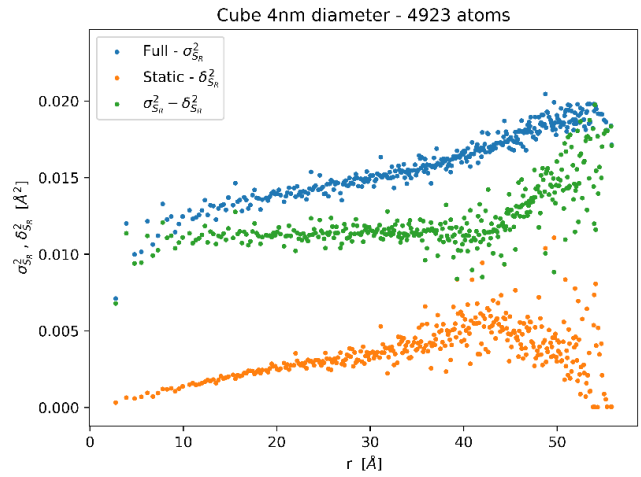

a)

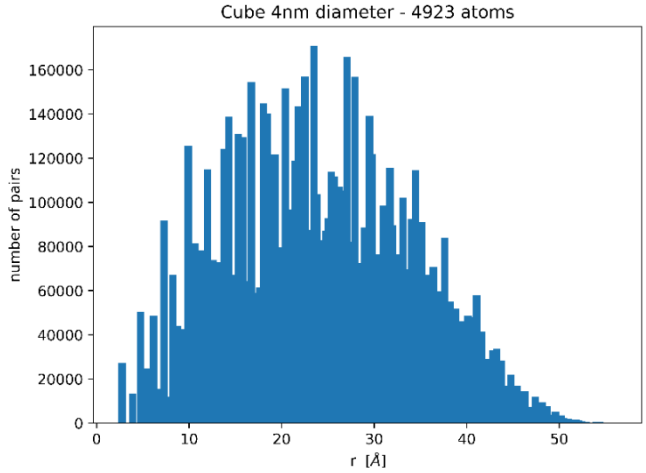

b)

Figure 1-13

MSRD components for a 20% truncated cube of 4923 atoms.

a) The three components of Relative Displacement: static (orange), full (blue), difference of the two (green).

b) The corresponding number of pairs for each coordination shell of radius R.

Differently from the thermal component, the static displacement is specific of the nanocrystal shape. As already pointed out, the static MSRD increases steadily until the “face-face” distance in truncated nanocubes, and a few atom layers short of the diameter for spheres; beyond that point the trends decrease linearly (see Figure 1-10 and Figure 1-11). The combined effect of thermal and static components (the full MSRD) is rather similar for cubes and spheres, with the former presenting a large scatter of values.

In the following Figure 1-14 and Figure 1-15 we can see the trend of $\delta_{SR}{}^2(r)$ for two nanocrystals with comparable number of atoms, respectively a sphere of about 7 nm diameter and a (20%) truncated cube of edge about 6 nm. As already discussed in this work, MSD and MSRD are variances of distributions, respectively of atomic displacements and of distances of pairs of atoms. In the figures, three points at increasing shell radius are highlighted in red. The distributions shown in part (b) of the figures are those corresponding to the three highlighted variances. It is quite apparent that a Gaussian distribution is just a coarse approximation of the real distributions, and it is more reasonable for the sphere than for truncated cubes. For truncated cubes the shape of the distribution varies quite visibly from point to point, thus explaining the scatter of values in the MSRD trends, larger than the spherical case.

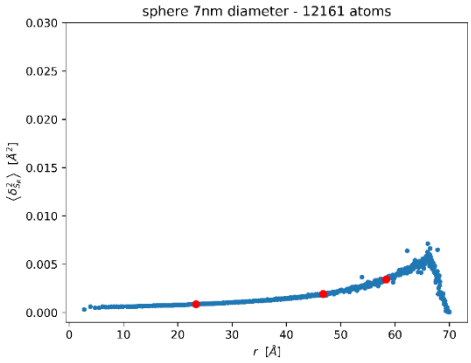

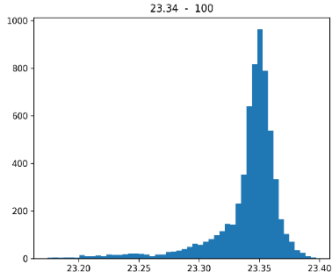

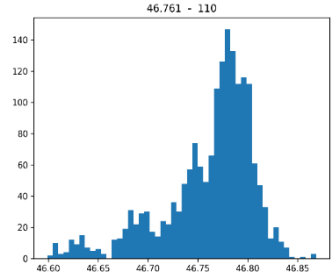

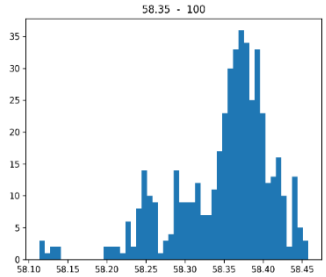

b)

Figure 1-14

MD simulation of a sphere of 7 nm diameter, 12161 atoms.

*a) Trend of the **static** MSRD component (blue), with three points highlighted in red.*

b) Static displacement distributions for the three points shown in red in a).

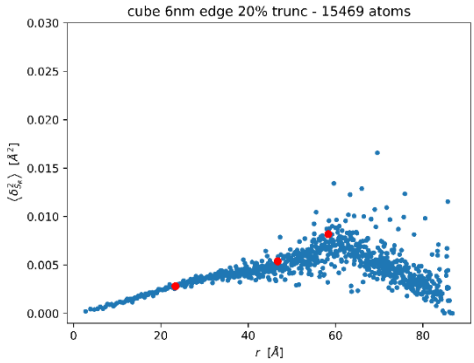

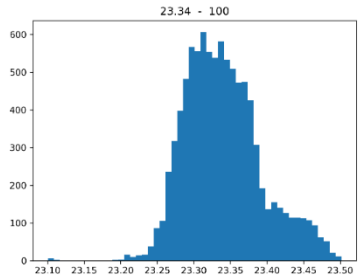

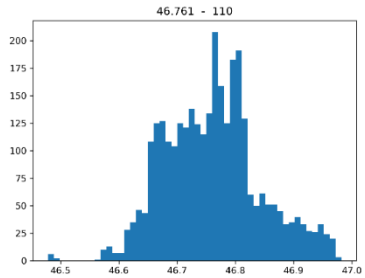

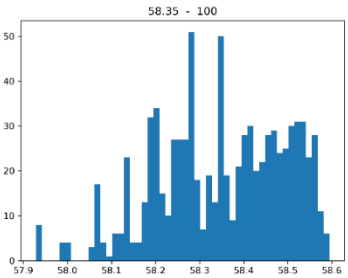

b)

Figure 1-15

MD simulation of a (20%) truncated cube of 6 nm edge, 15469 atoms.

a) *Trend of the **static** MSRD component (blue), with three points highlighted in red.*

b) *Static displacement distributions for the three points shown in red in a).*

1.5 DIFFRACTION FROM NANOCRYSTALLINE SYSTEMS

1.5.1 Debye-Waller coefficient

The MSRD connects directly to measurable quantities in diffraction. The Debye-Waller coefficient (Debye 1913) (Waller 1923), for instance, provides a measure of structural disorder in materials, directly related to the static and dynamic components of the MSD ($\overline{\sigma_i^2}$) (Krivoglaz 1969):

$$B_{ISO} = \frac{8\pi^2}{3}\,\overline{u^2}, \tag{1-30}$$

where $\overline{u^2} = \sum_{i=1}^{N_{Atoms}} \overline{\sigma_i^2}$ is the average of the MSD of each atom in a coherently scattering domain.

B_{ISO} is a quantity related to an average (and isotropic) effect of the atomic motion. In spectroscopic techniques it usually accounts for the atomic displacement, mainly due to temperature. In general, $\boldsymbol{B}$ is not a scalar quantity and depends on the direction (Willis B. T. M. 1975); it has also been shown recently that the correlated motion of the inner coordination shells also influences the values in small crystalline domains (a. L. Scardi P. 2016). However, considering the information content in a typical powder pattern, it is common practice in powder diffraction and for polycrystalline bulk systems to use the scalar value $\boldsymbol{B} \sim B_{ISO}$.

In the context of the present work, molecular dynamics allows the calculation of the overall thermal factor by using the MSD as in (1-30), by following atoms trajectories in time.

1.5.2 X-Ray Powder Diffraction and Whole Powder Pattern Modelling

The WPPM provides a theoretical expression of the whole profile based on a convolution of components for the contributing effects:

$$I_{hkl}(q, q_{hkl}) \propto \int_{-\infty}^{+\infty} \mathbb{C}_{hkl}(L) e^{i(q-q_{hkl})\cdot L}\, dL, \tag{1-31}$$

where q and q_{hkl} are the scattering vector, respectively for any value and in Bragg condition, whereas L is the Fourier length. The Fourier Transform, according to the convolution theorem, is the product of all relevant components:

$$\mathbb{C}_{hkl}(L) = T^{IP}(L) \cdot A^{S}_{hkl}(L) \cdot A^{D}_{hkl}(L) \cdot \dots \qquad (1\text{-}32)$$

It is pertinent in this application to consider the domain size/shape component $A^{S}_{hkl}(L)$ and the strain component $A^{D}_{hkl}(L)$. The contribution of the instrument ($T^{IP}(L)$) is of interest in dealing with experimental data and need not to be considered for simulations. So we focus on the two profile components,

$$I_{hkl}(q, q_{hkl}) \propto \int_{-\infty}^{+\infty} A^{S}_{hkl}\, A^{D}_{hkl}\, e^{i(q-q_{hkl})\cdot L}\, dL. \qquad (1\text{-}33)$$

1.5.2.1 Common Volume Function

A^S is the finite-size profile component, which according to Wilson has a simple geometrical meaning as normalized Common Volume Function (CVF) (Wilson 1962). In particular

$$A^{S}(L) = CVF(L)/CVF(L=0) \qquad (1\text{-}34)$$

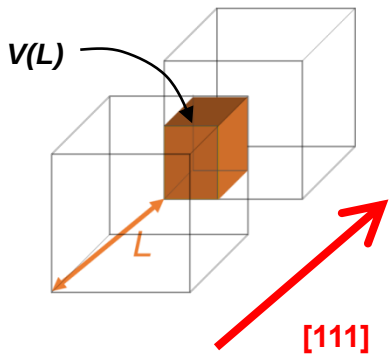

The CVF is the intersection volume between a body and the same body translated by a distance L along the direction [hkl]. According to this definition, V(L=0) is the volume of the body. The figure shows V(L) of a perfect cube along [111].

A^S encodes information in the diffraction profile on the size and shape of the nanocrystal and has simple analytical expressions for regular shapes. For

example, for a spherical nanoparticle of volume D (the hkl subscript is dropped for the isotropy of the spherical shape),

$$\mathrm{A^S} = 1 - \frac{3}{2}\frac{\mathrm{L}}{\mathrm{D}} + \frac{1}{2}\left(\frac{\mathrm{L}}{\mathrm{D}}\right)^3. \qquad (1\text{-}35)$$

Suitable expressions can be obtained for other shapes of simple convex solids, also considering size dispersion, i.e., a distribution of sizes. In the context of MD simulations, $\mathrm{A^S}$ is obtained numerically, by directly counting the atom couples for each distance L along the given [hkl] direction in the nanocrystal (A. L. Leonardi 2012), so it is in principle known for any possible shape.

For any polyhedron of volume V^c, the Common Volume Function, CVF_{hkl}, is described by a cubic equation of *L*, (Wilson 1962)

$$A^c_{hkl}(L) = \frac{CVF_{hkl}(L, D, h, k, l)}{V^c(D)} = \sum_{n=0}^{3} H^c_n \left(\frac{L}{D}\right)^n. \qquad (1\text{-}36)$$

In the case of simple polyhedra like cube or octahedron, some relatively simple analytical expression can be written. Let us call $D'(hkl)$ the limit distance along [hkl] direction, i.e. the maximum allowed distance between pairs of atoms along the considered direction. Larger values of L would imply pair of atoms outside the boundaries of the particle.
For the cube the expression for the Size component are:

$$\begin{cases} A^S(L) = 1 - \dfrac{h+k+l}{H}\dfrac{L}{D} + \dfrac{hk+kl+hl}{H^2}\left(\dfrac{L}{D}\right)^2 - \dfrac{hkl}{H^3}\left(\dfrac{L}{D}\right)^3 \\ A^S(L) = 0 \end{cases} \qquad (1\text{-}37)$$

In this work, an expression for truncated cubes is needed. Even though the corresponding polynomial might require to be defined piecewise, with different coefficients for different ranges from *L*=0 to *L* =D'(hkl), where D'(hkl) is the maximum length in the polyhedron along the given [hkl] direction. For Wulff solids it is proved that the CVF for the given [*hkl*] can be described by a single cubic or by a piecewise cubic. Details are given by (A. L. Leonardi 2012).

That corresponds to the cubic equation respectively throughout the entire range from $0 \leq L \leq D^{'}(hkl)$ or with the coefficients (H_0, H_1, H_2, H_3) defined in $L \leq 0 \leq L^{'}(hkl)$
$\left(H_0^{'}, H_1^{'}, H_2^{'}, H_3^{'}\right)$ defined in $L^{'}(hkl) \leq 0 \leq D^{'}(hkl)$
It is convenient to define

$$D^{'} = \frac{D}{K^c(hkl)}, \qquad (1\text{-}38)$$

with $K^c(hkl)$ a function of the specific direction, and *D* any suitable reference length in the solid (the edge of the cube in the case of a perfect cube). This definition is coherent with (Scardi, 2001), where $K^c(hkl)$ is given for several simple solids: for cubes, $K^c(hkl) = \frac{h}{\sqrt{h^2+k^2+l^2}}$ (as shown above). For Wulff solids, *D* might be the edge of the original cube (one of the extremes in the Wulff series), and D' calculated analytically or tabulated for the different degrees of truncation, starting from the perfect cube (truncation = 0) to the octahedron (truncation = 1).

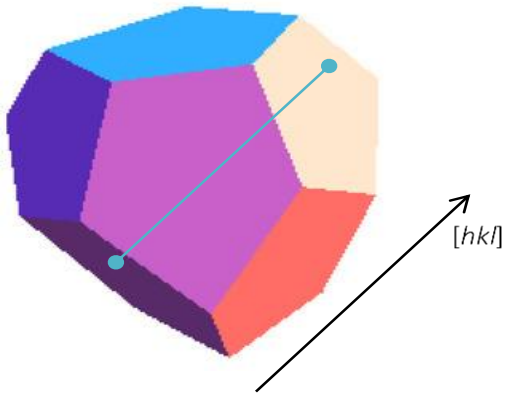

Figure 1-16

Example of a polyhedral crystallite with indication of the max length along the [hkl] direction

When dealing with a real powder sample, the nanoparticles that comprise the powder are never all of the same size nor of the same shape. Therefore, the size component in the FT should not describe only one particle. For simplicity let us assume that the particles have the same shape, which is a characteristic matched by several preparations of metallic nanocrystalline catalysts (Niu

2011) (Zhang 2012) (Laskar 2014), but have a distribution of sizes $g(D)$. A realistic distribution is the lognormal distribution with parameters μ and σ:

$$g(D;\,\mu,\sigma) = \frac{1}{D\sigma\sqrt{2\pi}}\exp\left[-\frac{(\ln D\ -\ \mu)^2}{2\sigma^2}\right]. \qquad (1\text{-}39)$$

The moments of the distribution, that are useful to construct the convolution size component of a lognormal distribution of particles, are given by the expression:

$$\mathrm{M}_n(\,\mu,\sigma) = \frac{\int_0^{+\infty} x^n g(x)dx}{\int_0^{+\infty} g(x)dx} = \exp\left[n\mu + \frac{n^2}{2}\sigma^2\right]. \qquad (1\text{-}40)$$

By this definition, then, the Fourier Transform of the powder diffraction line profile of a distribution ($g(D)$) of polyhedra, that is, with identical shape but size changing according to the distribution, is given by

$$A_{hkl}(L) = \frac{\int_{L\cdot K^c}^{\infty} A_{hkl}^c(L)g(D)V(D)dD}{\int_0^{\infty} g(D)V(D)dD} = [M_3]^{-1}\int_{L\cdot K^c}^{\infty} A_{hkl}^c(L)g(D)D^3dD, \qquad (1\text{-}41)$$

where in the last equality it is assumed that the volume of the solid can be written in a form proportional to a single parameter *D*. As an alternative the first equality always works.

This definition is especially useful if one adopts the notation of eq. (1-36), so that eq. (1-41), for the specific case of a lognormal distribution, is:

$$A_{hkl}(L) = \sum_{n=0}^{3} H_n^c erfc\left[\frac{ln(L\cdot K^c) - \mu - (3-n)\sigma^2}{\sigma\sqrt{2}}\right]\frac{M_{3-n}}{2M_3}L^n. \qquad (1\text{-}42)$$

For truncated cubes, as already stated, one can calculate the common volume numerically and, once set the shape (i.e. the degree of truncation of interest)

an expression can be constructed for the size component for a lognormal distribution of particles with that same shape.

1.5.2.2 Strain component

The strain component in the WPPM convolution encodes information in the diffraction profile on the atomic displacement in the specimen with respect to an ideal crystallographic configuration. Said displacement (also expressed as a strain) can be the result of different effects, like presence of lattice defects or just the surface relaxation due to the finite size of the particles.

In the next paragraph we show explicitly an example of strain component, and how the relevant parameters can be calculated from MD simulations.

1.5.3 Warren's approach

An important connection exists between the work illustrated up to this point on MSRD and XRD. As discussed in previous paragraphs, the MSRD for a truncated cube shows important properties, and also increasing scatter of values as the distances increase (for shells very far apart). The next step is to separate according to crystallographic directions, in the same fashion as the contributions to MSRD for different shells can be separated.

This operation translates into changing the set of atomic indices we use for spatial averaging, adding a new condition:

$$S_{R,hkl} = \left\{ i,j : \left\| \boldsymbol{r}_{\boldsymbol{i};\boldsymbol{I}} - \boldsymbol{r}_{j;I} \right\| = R \ \wedge \ (\boldsymbol{r}_{\boldsymbol{i};\boldsymbol{I}} - \boldsymbol{r}_{j;I}) \circ \hat{\boldsymbol{u}}_{hkl} = \ R \right\}; \qquad (1\text{-}43)$$

where we denoted with $(\circ)$ the dot product between vectors, and with $\hat{\boldsymbol{u}}_{hkl} = \frac{\boldsymbol{u}_{hkl}}{\|\boldsymbol{u}_{hkl}\|} = (h,k,l)/\sqrt{h^2+k^2+l^2}$ the unit vector along the family of crystallographic directions $\langle hkl \rangle$.

Based on the MD simulations and the definitions already introduced, we can account for the crystallographic direction by sorting appropriately all couples of atoms in a nanocrystalline domain. We keep track of the atom pairs that lie, in the ideal configuration, along the same direction (the versor $\hat{\boldsymbol{u}}_{hkl}$), and then further separate these pairs into displacement distance groups (similar to the

separation in shells, but now atoms in pairs obey to an additional constraint, see Figure 1-17).

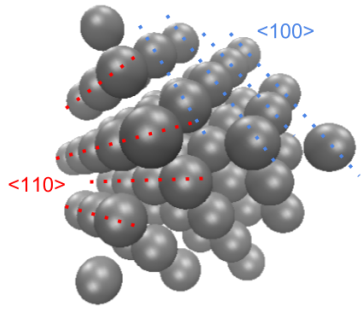

Figure 1-17

Qualitative representation of the separation of atoms groups according to crystallographic directions.

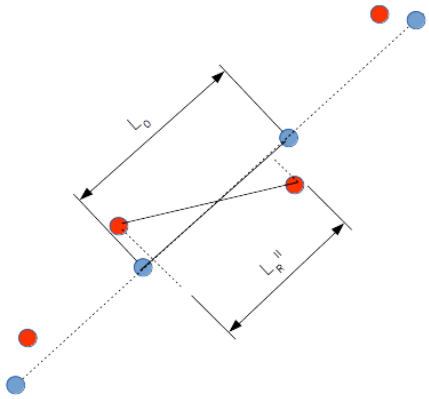

Figure 1-18

*Blue dots represent the atoms in the **ideal configuration**, red dots are atoms in the **relaxed configuration**, while the dashed line is a specific [hkl] direction.*

This approach is well known in diffraction theory, as shown in several articles and textbooks (Warren, X-Ray Diffraction 1990) (Warren, A generalized Treatment of Cold Work in Powder Patterns 1955) (Stokes 1944). In particular, Warren's theory shows how information on directional atomic displacement can be represented: the *Warren plot*, originally introduced by Warren & Averbach in 1950 (Warren B.E. 1950), is the representation of the standard deviation of the distribution of relative displacements of couples of atoms along a specific [*hkl*] direction, with respect to the ideal distance between any two pairs:

$$\sigma_{hkl}(\mathrm{L}) = \sqrt{\langle \Delta L_{hkl}^2 \rangle - \langle \Delta L_{hkl} \rangle^2}, \qquad (1\text{-}44)$$

where $\Delta L = L_R^{//} - L_0$. It is worth noting, in this case, we indicate the interatomic distance with *L* instead of using the $\boldsymbol{r}_{ij}$ notation introduced above. With this we want to stress that Δ*L* is the projection of the interatomic distance on the interatomic distance in the *ideal case* (see Figure 1-18), i.e. the displacement with respect to an idealization of the crystal, and not to the average of all atom's pairs belonging to the shell.

This subtle difference accounts for some discrepancies between the two methods, but the code written in this Thesis work for the MSRD calculation can be suitably modified to obtain the Warren plot function $\sigma_{hkl}(\mathrm{L})$.

In particular the quantities $\langle \Delta L_{hkl}^2 \rangle$ and $\langle \Delta L_{hkl} \rangle$ can be directly calculated from the MD simulations, and can be used to construct the strain component in the WPPM convolution.

The strain component can be split into a real and an imaginary part:

$$A^D(L) = A(L) \cdot B(L). \qquad (1\text{-}45)$$

As shown recently by Perez-Demydenko & Scardi (Perez Demydenko C. 2017), a reasonable approximation for $A(L)$ and $B(L)$ is:

$$A(L) \cong \exp[-q_{hkl}^2 \langle \Delta L_{hkl}^2 \rangle / 2], \qquad B(L) \cong q_{hkl} \langle \Delta L_{hkl} \rangle. \qquad (1\text{-}46)$$

In the modern powder diffraction theory there are models that describe the diffraction line profiles in terms of the displacement quantities $\langle \Delta L^2 \rangle$ and $\langle \Delta L \rangle$. These quantities are related to the strain field in the material, as $\varepsilon(L) = \Delta L(L)/L$, and can be used to model the deformation effect with respect to an ideal (unperturbed) configuration. Models available in the literature, like the Krivoglaz-Wilkens models (Wilkens 1970) for dislocations, and the more empirical PAH (Popa–Adler–Houska) (Adler 1979) (Popa 1998) (A. R.-D. Scardi P. 2018), are based on continuum mechanics and rely on several

approximations, not always or not entirely appropriate to nanoparticles (P. E.-W. Scardi 2018). Indeed, one of the goals of the present Thesis is to shed light on the cited models , investigating their meaning and aptness in the context of nanocrystals.

IMPLEMENTATION OF THE RESULTS

We simulated Pd nanocrystals with different number of atoms and different shapes. The shapes have been chosen to range from around 0% truncation (a cube) to 100% (an octahedron).

The size name of the various particles is a "nominal value", according to the number of atoms. For example, a particle of arbitrary truncation that is identified with "15nm" contains a number of atoms roughly equal to those in a cube with edge of 15nm.

In

Table 4 the number of atoms is shown for each of the 36 nanoparticles simulated.

N. atoms	4nm	6nm	8nm	10nm	12nm	15nm
5%	4631	14895	34461	66325	113491	228259
20%	4491	14371	33029	69971	117435	231015
40%	4503	14357	35783	67303	114113	228365
60%	4501	14933	34023	66665	115395	226077
80%	4267	14553	35785	68099	109525	227743
100%	4573	16263	33775	69201	110929	219023

Table 4
Number of atoms for each simulated nanoparticle.

We did not simulate a cube with 0% truncation because of the extremal atoms on vertices and edges. This is discussed in the Appendix.

For each combination of size and shape, $\sigma_{hkl}{}^2(\mathrm{L})$ (the function of the Warren Plot (1-44)) has been calculated along several crystallographic directions: [100], [110], [111], [311], [331], [420], 422], …

The main goal of the following analysis is to study how the atomic displacement is influenced by the shape and size of the nanoparticle. The computational results will also help in the creation of a Strain Term $A_{hkl}^{D}(L)$ to be used in WPPM method.

2.1.1.1 Different shape, fixed sizes.

We first analyze how the Warren Plot (WP) changes for nanoparticles with the same number of atoms, but with different geometrical shapes. The results for three crystallographic directions ([100], [110], [111]) for the case of particles with 200000 atoms (the nominal "15nm" case) are shown in Figure 2-1 for truncated cubes with truncation spanning from 5% (close to perfect cube) to 100% (octahedron). The WP trends are represented by full lines, instead of scattered data points, to better illustrate the different behavior and dependence on shape as a function of the pair distance. To keep all trends on the same scale the abscissa is normalized to the maximum length for the given [hkl] direction.

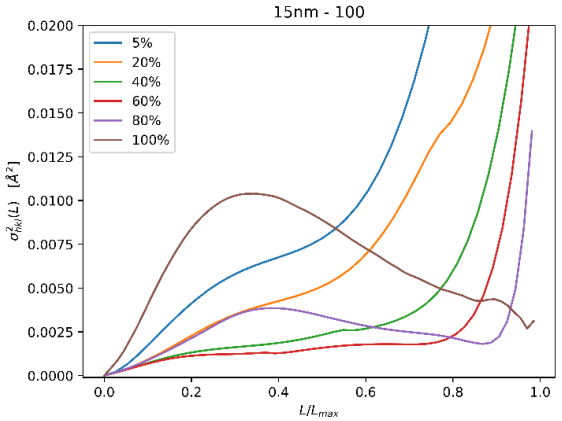

a)

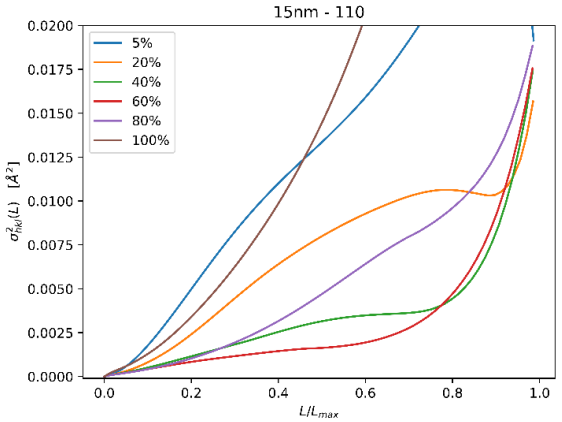

b)

Figure 2-1

Plots of $\sigma_{hkl}{}^2(L)$ for nanoparticles of nominal size "15nm" (see Table 4 for details) with different truncations values and along crystallographic directions [100] (a), [110] (b), [111] (c).

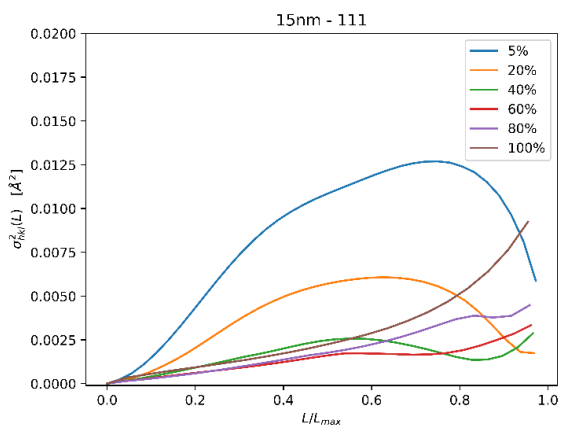

c)

Although peculiar of the different shapes, WP's trends have no simple and unambiguous relation with the truncation level. Some features are nevertheless apparent: regardless of the crystallographic direction, shapes lying halfway between the two extremes (cube and octahedron) of the Wulff series, e.g., 40% and 60% truncation, show the overall lower values of σ^2_{hkl}. Indeed, truncated cubes at 40% and 60% are "rounder", i.e. they are the Wulff shapes closest to the isotropy of spherical nanoparticles. On the contrary, shapes at the extremes have trends drastically changing with the [hkl] direction. For example, the 5% truncated cube, for the [111] direction, assumes values that are 2 to 4 times larger than the other shapes (Figure 2-1 (c)); whereas for octahedron (100%) largest values are obtained for [110] and [100].

2.1.1.2 Different sizes, fixed shapes.

We proceed by analysing Warren Plots of nanoparticles with the same shape but increasing number of atoms. In this case too, the distances are normalized to the maximum value, so the abscissae are restricted to the interval [0,1].

For a cube of edge L the maximum distance allowed for a pair of atoms depends on the direction of the vector connecting the two atoms. The maximum distance along <100> is of course L, whereas along <110> is $\sqrt{2}L$, and along <111> is $\sqrt{3}L$ (see paragraph Common Volume Function1.5.2.1).

Some discrepancies are to be expected in a numerical calculation of WPs. In fact, it is inherently impossible, with discrete elements like atoms, to perfectly replicate the same geometrical shape at every dimension. We can likewise say that the discrete nature of atoms does not allow them to completely fill purely geometrical shapes of increasing size.

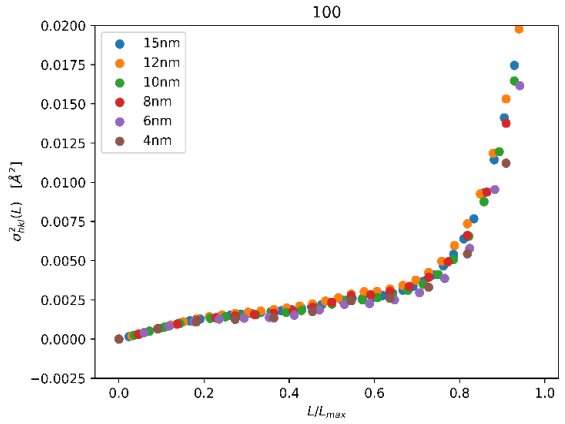

a)

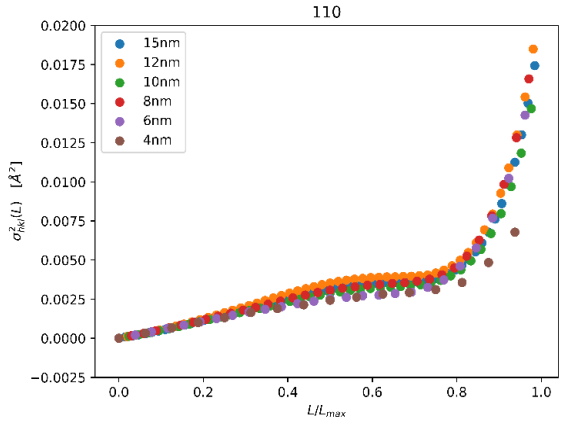

b)

Figure 2-2

Values of $\sigma_{hkl}{}^2$ for cubes with 40% truncation, with different number of atoms (see

Table 4 for details), along the directions [100] (a), [110] (b), [111] (c).

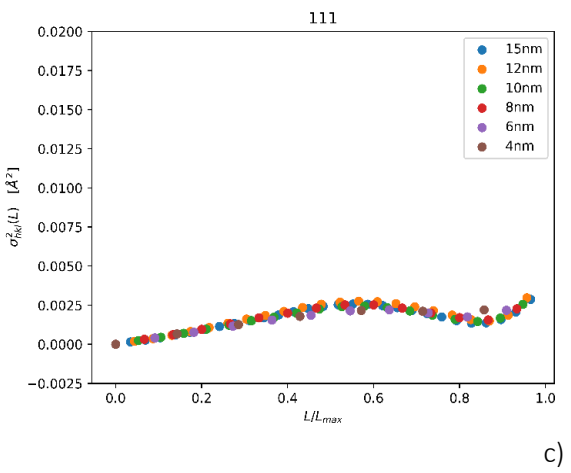

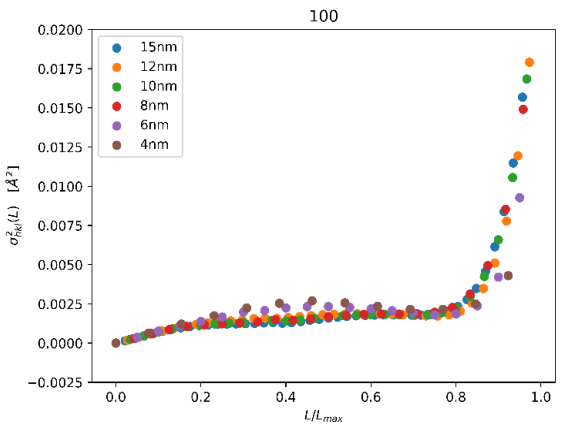

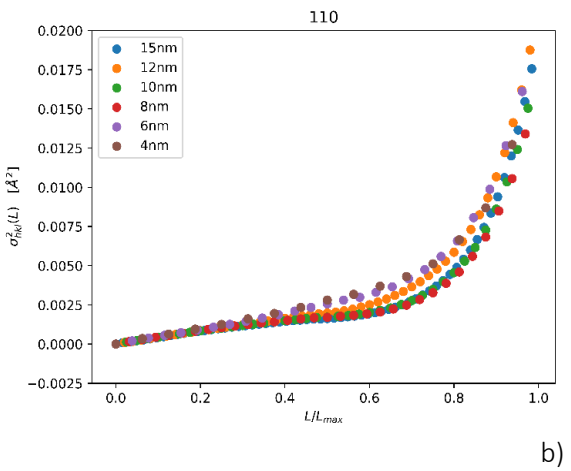

Figure 2-3

Values of $\sigma_{hkl}{}^2$ for cubes with 60% truncation, with different number of atoms (see

Table 4 for details), along the directions [100] (a), [110] (b), [111] (c).

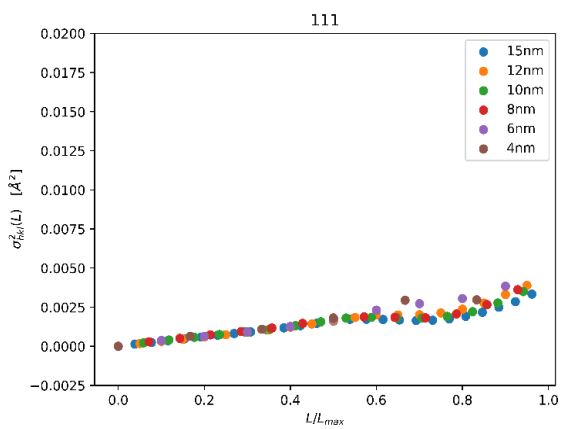

c)

As shown in Figure 2-12 and Figure 2-13, respectively for the 40% and 60% truncation, the trends are remarkably similar for all sizes in the studied range, which spans from rather small to values of the experimental cases discussed in the following. Apart from some minor and understandable discrepancies, the steepness and convexity of the curves is preserved across all sizes. For all six shapes (from 5% to 100% truncation) and along the tested directions (13 in total) the results are similar, with deviations observed in some isolated cases only.

From these simulations it is rather evident that the trend in the Warren plot is mainly dictated by the shape of the nanocrystal, whereas the effect of the size is just a rescaling of the lengths. As an example, Figure 2-14 shows results for the direction [620] for the 60% truncation shape:

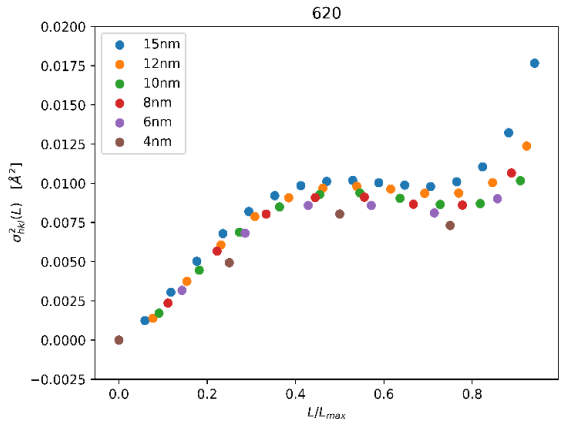

Figure 2-4

Values of $\sigma_{hkl}{}^2$ for cubes with 60% truncation, with different number of atoms, along the direction [620]

The convexity is preserved across all sizes, as it can be seen by the fact that all simulated particles present a plateau roughly at half of the maximum atom-atom distance allowed along the [620] direction.

If one plots together the values of $\sigma_{hkl}{}^2$ for as many (virtually all) directions in the crystal, the resulting sum approaches, with minor differences, the "static MSRD" $\delta_{S_R}{}^2$. As an example, several WPs are shown in Figure 2-5 for the 20% truncated cube of nominal size 15nm.

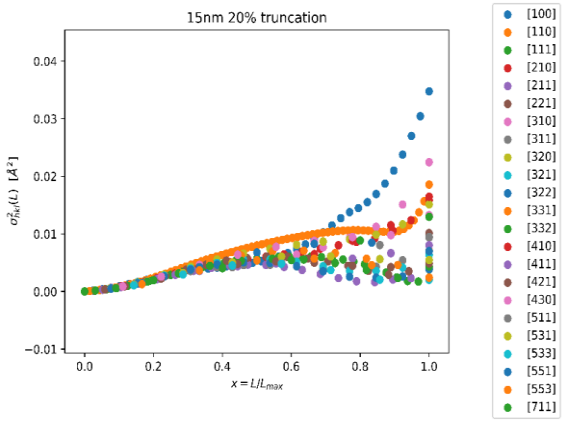

Figure 2-5

Plot of several $\sigma_{hkl}{}^2$ trends along different directions for a cube truncated 20%.

The results in this paragraph can be summarized as follows:

1. The dependence of $\sigma_{hkl}{}^2$ **on shape** is not a simple one. We can qualitatively state that shapes at the extremes of the Wulff series (cube and octahedron) have a more variable and direction-dependent Warren plot, both because of geometrical reasons and because of number of under-coordinated atoms (vertices and edges). Shapes in the middle of the Wulff series (~40, 50, 60%) tend to be isotropic, i.e. $\sigma_{hkl}{}^2$ is independent of (or little dependent on) the [hkl] direction.
2. Even in the same particle, $\sigma_{hkl}{}^2$ can drastically change for different directions: $\sigma_{hkl}{}^2$ is sensitive to the anisotropy of both the crystal structure (that determines the elastic properties) and of the geometrical shape. The latter effect could partially be ruled out when analyzing, as we did, many different shapes.

3. Values of ${\sigma_{hkl}}^2$ are generally higher for the extremes of the Wulff series. Intermediate shapes show lower disorder, as it is true of the spherical shape.

The first point is especially relevant to the rest of this work, as it allows us to describe the WPs for any shape and direction by means of simple parametrizations.

2.1.2 Parametrization of WPs

A plausible function for a parametric representation of the numerical results presented so far is a polynomial without zeroth term (since ${\sigma_{hkl}}^2(0) = 0$), multiplied by an exponential function to enforce a monotonously increasing behavior at short distances. The simulated values have been fitted by a non-linear least squares (NLLS) algorithm (Jones E 2001). The modelling function is of the form:

$$ {\sigma_{hkl}}^2(L) = e^{L-1}(aL + bL^2 + cL^3 + dL^4). \qquad (2\text{-}1) $$

The parameters a, b, c, d are obtained from the NLLS fitting. Different weights have been assigned to the data to fit in the procedure. As explained in (More 1977), the use of weighted data means that not all points are equally relevant and similarly to the case of the MSRD, the number of atom pairs varies with the distance (see Figure 1-13 (b) for example). In the case of the directional quantity, ${\sigma_{hkl}}^2$, characterizing the Warren plots, the number of atom pairs is proportional to the Common Volume Function (paragraph1.5.2) along the given $[hkl]$ direction (Figure 2-6), which is the most reasonable weight to be used in the NLLS fit of the parametric equation.

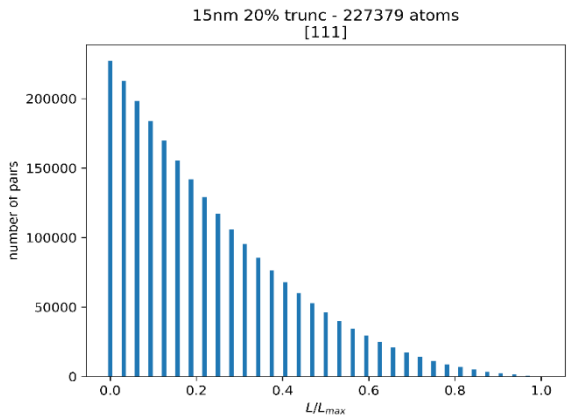

Figure 2-6

Number of pairs for each (normalised) distance along direction [111], for a truncated (20%) cube with 227379 atoms. Count starts at distance 0 (each atom with itself), where the number of pairs is the number of atoms.

Figure 2-7 shows some parametrizations with the best fit by NLLS. It is quite evident that the proposed parametric representation is sufficiently flexible to capture the main features of the WPs along any direction.

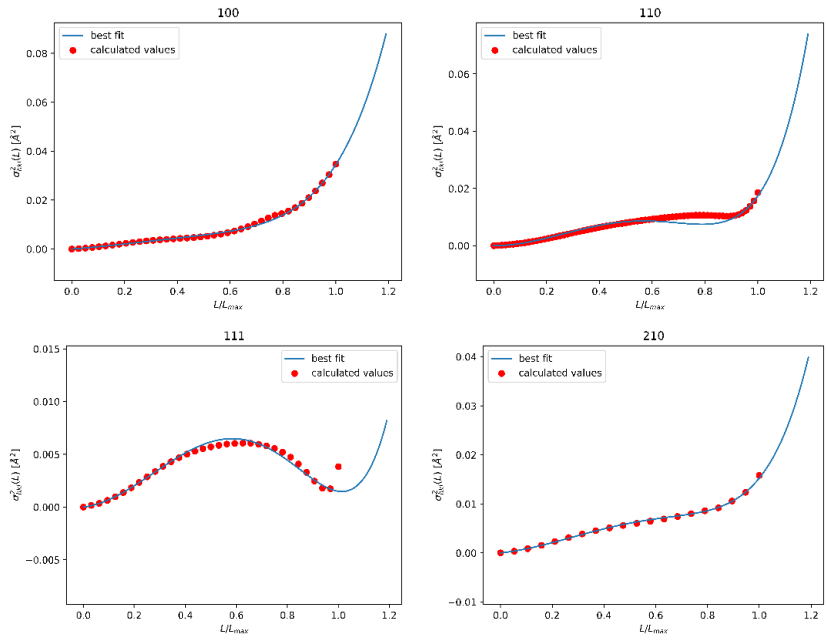

Figure 2-7

NLLS fit of the parametric expression of $\sigma_{hkl}{}^2$ for different crystallographic directions.

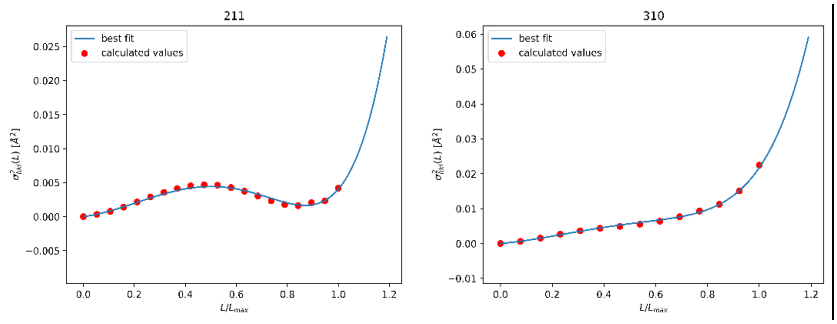

Based on the analysis carried out with the use of a parametric description of the Warren Plots, we can put forward the following comments. The modelling function is formally defined over an infinite domain, while the Warren Plot must of course be limited to the maximum atom-atom distance along the considered direction. However, even if the parametrization extends beyond the max length, as shown in Figure 2-7, the use of $\sigma_{hkl}{}^2$ will always be paired with the common volume function, which is zero, by definition, outside the boundaries of the particle.

The function in eq. (2-1) represents the MD result. It is therefore determined by the specific EAM potential used, and by the rather ideal conditions of the simulation (a nanocrystal isolated in a vacuum). In the practical implementation of the parametric equation, therefore, additional parameters will be introduced to add the flexibility required to adapt to the real, experimentally obtained WPs. This point is discussed in paragraph 2.1.4.

2.1.3 Real Powder sample vs MD simulation: the correction to $\langle \Delta L^2 \rangle$

In the original work of Warren and in more recent applications, the real component of the strain term is written as a function of $\langle \Delta L^2 \rangle$ only. The assumption is that the sample supports no macrostrain: if it is a polycrystalline bulk material, the crystalline domains do not undergo significant contraction or expansion. This is generally true for real powder samples, as in the case of metal nanoparticles in a capillary suspended in an organic capping agent. Then it is understood that $\Delta L = 0$, so that $\sigma_{hkl}^2 = \langle \Delta L^2 \rangle$ (see eq.(1-44)).

When dealing with molecular dynamics simulations of nanoparticles, a starting (reference) configuration exists, which in the present case is the ideal

crystallographic lattice, based on bulk values for the lattice parameter. Then it is quite evident that $\langle \Delta L \rangle \neq 0$, since the particle will contract or expand from that initial (and arbitrary) reference configuration, depending on many factors such as the choice of the interatomic potential, the number of atoms or the overall shape.

The Warren Plot from MD simulations therefore requires eq. (2-1), here proposed again as:

$$\sigma_{hkl}^2 = \langle \Delta L^2 \rangle - \langle \Delta L \rangle^2. \qquad (2\text{-}2)$$

Details on the influence of the potential when calculating equation (2-2) from MD trajectories can be found in the Appendix.

2.1.4 Implementation of MD results in the WPPM

Given the parametrization in eq. (2-1), the Fourier Transform of the strain component of the diffraction line profile, to be used in the WPPM approach described before, can be calculated as:

$$\mathrm{A}_{hkl}^{\mathrm{D}}(L) = \exp\left(-\frac{q_{hkl}^2}{2}\sigma_{hkl}^2(L)\right) \qquad (2\text{-}3)$$

with σ_{hkl}^2 as in eq. (2-2). This expression is based on the assumption that the displacement distribution (of which σ_{hkl}^2 is the variance) is a Gaussian, for every value of Fourier length, *L*, and for each orientation [hkl]. As already pointed out in a similar context, the discussion about Figure 1-14 and Figure 1-15 (paragraph 1.4.2), this assumption is only approximately true, although is used in most methods of line profile analysis (Warren, X-Ray Diffraction 1990) if the whole line profile is to be modelled.

We test the parametric expression and eq (2-3) on a real sample of Pd nanocrystals, about 15 nm edge (truncated nanocubes). The nanocubes, produced following an already reported procedure (e.g., see (A. L.-K. Scardi P. 2015) and references therein), were capped by PVP and contained in a kapton capillary for the XRD measurements. TEM (Figure 2-8confirmed the Pd

nanocubes are approximately 15nm edge, with a monomodal and relatively narrow size distribution (standard deviation 1.7 nm) (a. L. Scardi P. 2016); just few nanocrystals deviate from the cubic shape.

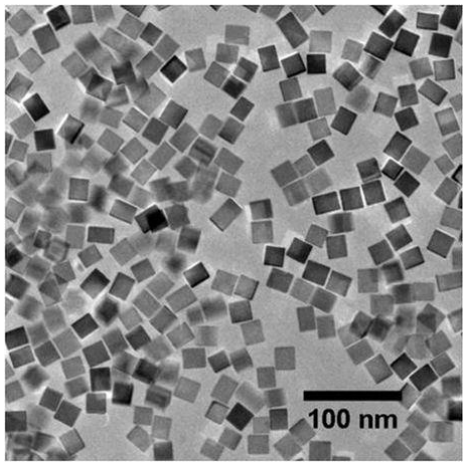

a)

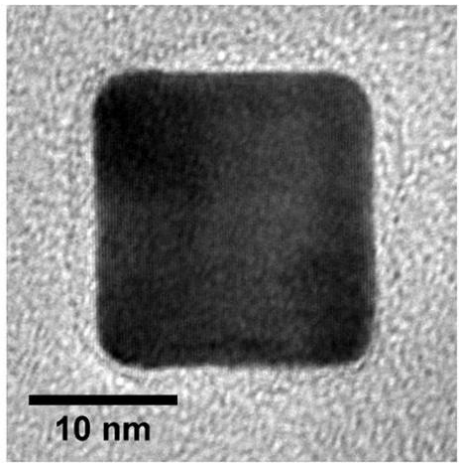

b)

Figure 2-8

TEM images of the sample used in (A. L.-K. Scardi P. 2015).

The shapes are very close to the truncated nanocubes discussed in the Thesis.

Higher magnification images (A. L.-K. Scardi P. 2015) show that cube corners and edges are clipped, respectively along (111) and (110) planes, so that a realistic picture of the average nanoparticle is like the simulation in Figure 2-9. These features can be observed in the picture of Figure 2-8.

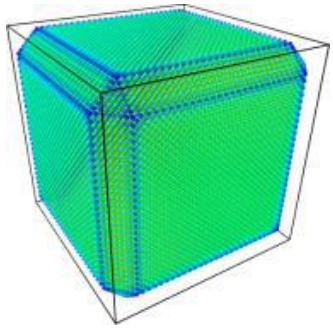

Figure 2-9

Model of the truncated nanocube of Pd used for the calculation of the Warren Plots

The X-ray diffraction patterns were collected with synchrotron radiation at 30keV, on the 11-BM beamline of APS (Advanced Photon Source of ANL, the Argonne National Laboratory, Argonne, USA), using the set-up described in (A. L.-K. Scardi P. 2015).

We then proceeded simulating a nanocube with truncation 20% and nominal edge length of 15nm, which can be considered statistically representative for size and shape of the experimental sample. From the simulations and procedure of the previous paragraphs, we calculated the directional MSRD quantities $\langle \Delta L_{hkl} \rangle$, $\langle \Delta L_{hkl}^2 \rangle$ and σ_{hkl}^2 for all the [hkl] directions involved in the experimental pattern. The parametrization of σ_{hkl}^2 has been implemented in a modified version of PM2K (Leoni M. 2006), a software based on the Whole Powder Pattern Modelling approach, as an additional strain broadening model (see below). To fit the model to the experimental pattern PM2K adopts a NLLS minimization procedure based on the Levenberg-Marquardt algorithm. Details are reported in the cited literature (P. Scardi, chapter 13 2008).

With respect to the expression (2-1) for σ_{hkl}^2, a free parameter A has been added to grant flexibility to the parametric model based on the MD results:

$$\sigma_{hkl}{}^2(L) = Ae^{L-1}(\boldsymbol{a}L + \boldsymbol{b}L^2 + \boldsymbol{c}L^3 + \boldsymbol{d}L^4). \qquad (2\text{-}4)$$

Indeed the parametrization was calculated for a specific particle, with a given truncation and size (Figure 2-9), whereas the experimental sample shows a distribution of sizes and some inevitable (although limited) variability in shape. The value of A can be refined in the NLLS procedure to allow the MD

parametrization of the strain broadening component to better adjust to the real sample, which is not composed of nanoparticles identical to those used to obtain the parameters of eq. (2-4). Therefore, it is important to underline that σ_{hkl}^2 in eq (2-4) has only **one** free parameter (A) while the other 4 parameters (a, b, c, d), calculated from the MD trajectories, as discussed in paragraph 2.1.2, are constant.

To evaluate the goodness of the constructed model versus the experimental data, we use the Weighted Sum of Squares (WSS) as statistical quality index. Besides testing the parametrization from MD, the following analysis is useful to test existing models of strain broadening. In particular, the literature reports models for σ_{hkl}^2 derived from continuum mechanics, like the Krivoglaz-Wilkens model, specific to deal with the strain field of dislocations (Krivoglaz 1969) (Wilkens 1970). A second, more recent model is based on the work of Adler & Houska and of Popa (Popa 1998), and it is therefore named PAH (A. R.-D. Scardi P. 2018); this model is partly empirical, but appropriate to grasp the main features of the strain field and its effect on the line profiles. Both models account in a flexible way for the anisotropy of the elastic medium and of the strain field of the defect causing the strain. Detail can be found in recent literature (A. R.-D. Scardi P. 2018), but in brief:

- PAH (Popa–Adler–Houska) (Popa 1998) provides a model of σ_{hkl}^2 based on two adjustable parameters (*a* and *b*) for the part dependent on the Fourier length, and two more parameters, *A* and *B*, for the anisotropy, respectively in:

$$\sigma_{hkl}^2 = \overline{C_{hkl}}(a \cdot L + b \cdot L^2) \qquad (2\text{-}5)$$

and

$$\overline{C_{hkl}} = A + B\frac{h^2k^2 + k^2l^2 + h^2l^2}{h^2 + k^2 + l^2}, \qquad (2\text{-}6)$$

where h,k,l are the Miller indices labelling each Bragg peak in the powder pattern. This expression is valid for the case of a cubic material, but can be generalized to any symmetry (A. R.-D. Scardi P. 2018).

- Krivoglaz-Wilkens model (Wilkens 1970). All parameters have a direct physical meaning related to the strain field of dislocations, but the functional dependence on the Fourier length, including the anisotropy already discussed for the PAH model, seems sufficiently flexible to describe other strain fields. Expressed in formal way, the model of σ_{hkl}^2 can be written as:

$$\sigma_{hkl}^2 = \frac{\overline{C_{hkl}}}{4\pi} a[-\log(L) + b + O((L/b)^2)]L^2, \qquad (2\text{-}7)$$

  with $\overline{C_{hkl}}$ as in eq (2-6), with *A* and *B* refinable parameters, in addition to *a* and *b* for the *L*-dependent part. As we do not refer to dislocations and use this model only for the convenient and flexible functional form, in the following we refer to equation (2-7) as pseudo-Wilkens model.

The two models (2-5) and (2-7) have 4 free parameters (*A*,*B*, *a*, *b*), both including a so-called contrast factor ($\overline{C_{hkl}}$) to account for the strain anisotropy of the sample (modifying *A* and *B* to change the [hkl] dependence). The "parametrization model" (eq. (2-4)) on the other hand, is much more rigid, as it can only adapt to the experimental data by changing *A*, while the specific [hkl] dependence is fixed from the Molecular Dynamics results.

In Figure 2-10 two examples of modelling are shown, one using the MD parametrization and the other using the pseudo-Wilkens model. Both fits show a small residual, and a good accordance with the experimental data.

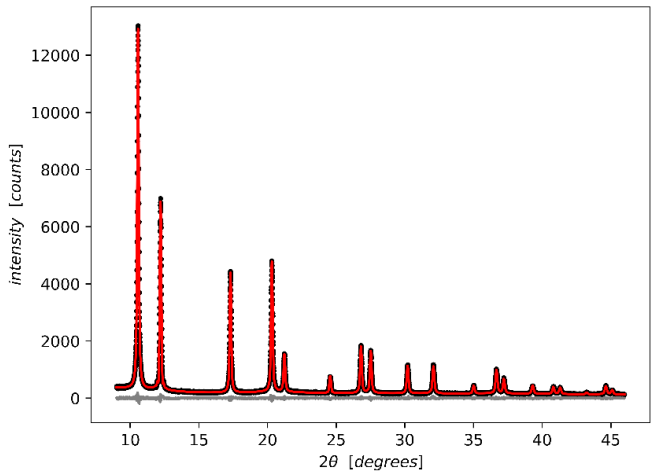

a)

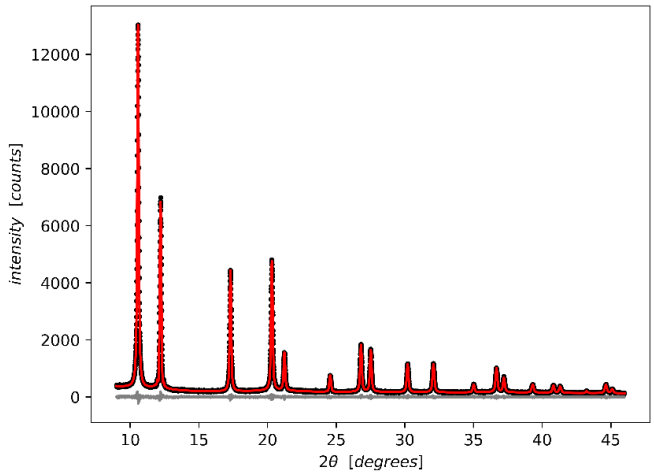

b)

Figure 2-10

Fitting of the experimental pattern for

a) WPPM with strain component obtained from the MD model

b) WPPM with strain component given by the pseudo-Wilkens model.

The three versions of σ_{hkl}^2 (eq. (2-4),(2-5) and (2-7)) are shown in Figure 2-11, obtained as best fit against the experimental data. Other components of the pattern modelling (such as the size component, the instrumental profile or the background) have been kept fixed to the values already refined in (A. L.-K. Scardi P. 2015) . This means that the differences between WSS's in the three

cases are due to the different choice of strain component, i.e. they depend on the expression chosen for σ^2_{hkl}.

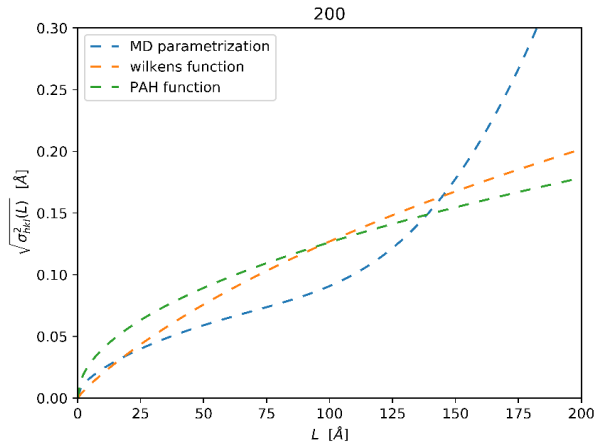

a)

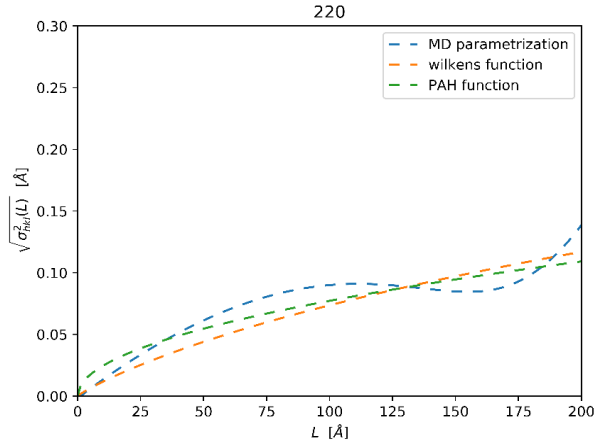

b)

Figure 2-11

Plot of the σ^2_{hkl} with the three different definitions, along three main [hkl] directions.

The three values of WSS are:

MD param.	WSS = 5693
pseudoWilkens	WSS = 5016
PAH	WSS = 5031

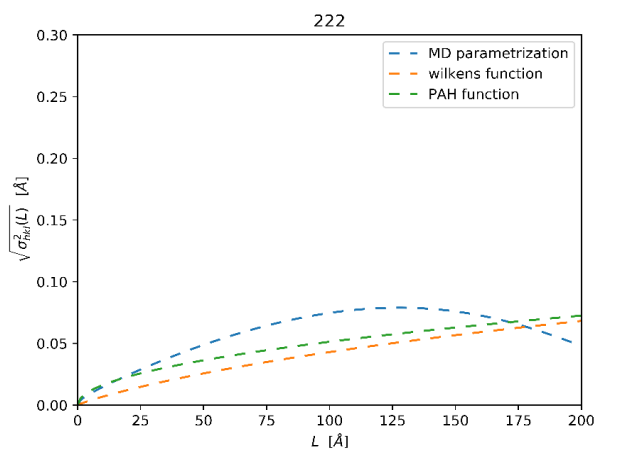

c)

The following conclusions can be drawn from the results shown in this paragraph. First of all, we underline that the main contribution to the line broadening, as it is often the case when studying nanocrystals, comes from the size (and shape) of the nanocrystals. The strain broadening adds as a relatively minor effect, in the convolution of equation(1-33), which is the core of the WPPM method. The instrumental profile adds a further contribution, which is however unimportant in the present case. The strain effect, however, can be well separated from the size effect because, as diffusely demonstrated in the literature and textbooks, the dependence on the scattering vector of size and strain broadening is quite different (Klug H. P. 1974).

So, within the limits of the experimental observation of a relatively minor effect, we see that the best WSS is obtained with the pseudo-Wilkens model, but PAH and also the MD parametrization follow very closely. In the refinement using the parametric model the value of the adjustable parameter is A = 0.960 (14), not far from unity, which means no correction with respect to the trend given directly by MD simulations. This means that the MD parametrization is surprisingly close to the much more flexible – adaptive – models of eq (2-5) and (2-6). As the fit to the experimental values gives A<1, we can only conclude that the MD simulations tend to slightly overestimate the contribution of inhomogeneous displacement to the line broadening.

Therefore, the most significant result is that the statistical quality of the fit made with the much more flexible strain models of eq. (2-4) and (2-5) is just

slightly better than that made with the MD parametrization of eq. (2-4). This means on one hand that the empirical models are appropriate, at least approximately, to deal with the complex strain field in the nanocrystals, which originates from the sub-coordination of the surface atoms and all related effects (like capping agents and environment); on the other hand, we cannot expect that an EAM potential will give results perfectly adhering to a certainly much more complex reality. This can be considered a validation of both possibilities, using empirical (but very flexible) line profile models or calculated models, as the MD parametrization. The second option opens new scenarios in the analysis of X-ray spectroscopy data.

2.2 Further Applications

The next three chapters present other applications of the concept described up to this point. Atomistic simulations and models are not only used for calculating quantities directly comparable with experiments, but they can also complement experimental results, by providing insight that is not otherwise accessible.

APPLICATION: DEBYE-WALLER COEFFICIENT OF HEAVILY DEFORMED NANOCRYSTALLINE IRON

This chapter is mostly based on a recently published article:

"Debye-Waller coefficient of heavily deformed nanocrystalline iron", P. Scardi, L. Rebuffi, M. Abdellatief, A. Flor and A. Leonardi, *Journal of applied crystallography, Volume 50, Part2, 508-518. April 2017.*

https://doi.org/10.1107/S160057671700022X

3.1 ABSTRACT

Synchrotron radiation XRD patterns from an extensively ball-milled iron alloy powder were collected at 100K, 200K, and 300K. Results were analyzed together with those of EFAXS, taken on the same sample at LN2 (77K) and room temperature (300K), to assess the contribution of static disorder to the Debye-Waller coefficient (B_{ISO}). Both techniques give a ~20% increase with respect to the bulk reference iron, a sensibly smaller difference than reported by most literature on similar systems. Besides good quality XRD patterns, proper consideration of the Temperature Diffuse Scattering seems to be the key to accurate values of Debye-Waller coefficient. Molecular Dynamics simulations of nanocrystalline iron aggregates, mapped on the evidence provided by XRD in terms of domain size distribution, shed light on the origin of the observed B_{ISO} increase. Main contribution to the static disorder is given by the grain boundary, while line and point defects have a much smaller effect.

3.2 INTRODUCTION

The Debye-Waller coefficient (B) provides a measure of structural disorder in materials, directly related to the static and dynamic components of the atomic mean square displacement (Krivoglaz 1969) (Kuhs 2006). Like most properties, the MSD depends on the size of the crystalline domain (Clark B.C. 1965) (Allen R.E. & F.W. DeWette 1969). However, there are no simple and general rules to predict the MSD in nanocrystals. Besides domain size and shape, deviations from bulk MSD values depend on lattice defects and environment surrounding the nanocrystals, i.e., whether they are embedded in a matrix or isolated, capped by contaminants or by suitable organic phases.

Free or weakly constrained metal nanoparticles often show a larger MSD, with a corresponding decrease of the average Debye temperature (Θ_D) (Valiev R.Z. 2000) (Zhao 1999). In simple monoatomic solids like cubic metal nanocrystals, the following relation holds between MSD and Θ_D at temperatures sufficiently high ($T>\Theta_D$) to render quantum effects (zero-point vibration) negligible (Willis B. T. M. 1975):

$$B_{iso} = \frac{8\pi^2}{3}\overline{u^2} \propto \frac{T}{\Theta_D} \qquad (3\text{-}1)$$

(same equation as (1-30)).

The MSD increase (and corresponding Θ_D decrease) is often attributed to a surface softening, as atoms on surfaces and interfaces are under-coordinated. LEED measurements on metals have shown that the surface Debye temperature is about 50% lower than the bulk value (Inagaki M. 1983) (Clark B.C. 1965) (VanHove M.A. 1986), with a corresponding increase in B_{ISO}. The surface effect is responsible for increasing average MSD (decreasing average Θ_D), which in nanocrystals scales approximately as the surface/volume ratio, i.e., as 1/D, where D is the diameter or any characteristic length of the crystalline domain. Mössbauer spectroscopy has shown a similar core/shell effect either in free iron nanocrystals (Eynatten G. Von 1977) and in ball-milled Cr-Fe alloy nanocrystalline powders, where the Debye temperature of the grain boundary region was found to be 100K lower (i.e., about ¼ lower) than the bulk value (Kuwano H. 1992). Beyond the simplistic view of a sharp core(bulk)/shell(surface) model, MD has shown quite clearly that the MSD is not constant across a metal nanoparticle. More than undergoing a sharp change from core to surface, the MSD increases steeply but continuously toward the surface layers, where the low coordination has effect on atomic displacement and vibrational properties (K. B. Gelisio L. 2013).

Besides the specific effect on the vibration dynamics of nanocrystals, the MSD increase is also related to a corresponding increase both in the thermal expansion coefficient (Yang C.C. 2006), and in the heat capacity at low temperature, where surface vibration modes are important (Michailov M. 2012) (Bai H.Y. 1996). The Debye-Waller (DW) coefficient of nanocrystals can therefore deviate considerably from the corresponding bulk perfect-crystal values, and in addition to the above mentioned effects, different types of static

disorder can be responsible for values in excess of the expected ones (Krivoglaz 1969). More recently, coupled MD and X-ray powder diffraction (XRPD) simulations have suggested that static disorder in grain boundary regions contributes both to the coherent and to the diffuse scattering (A. S. Leonardi 2012) (A. L. Leonardi 2013), the last resulting in a thermal-like step in the background of Warren plot profiles (Figure 3 in (Warren B.E. 1950). Experimental measurements of DW coefficient are therefore indispensable to assess presence and extent of the different contributing effects.

Despite the interest and generality of the problem, measured B values of nanocrystalline materials vary considerably in the literature, sometimes showing huge increments with respect to the reference values (Zhao 1999). Values for ball-milled iron, for example, have been reported to be 110% (Zhao Z.H. 2001) or even 300% (Azzaza S. 2015) higher than the reference DW coefficient for bulk iron (Butt 1988). The interpretation of such large increase of B is not always clear. Even if the role of surfaces and grain boundaries is well established (VanHove M.A. 1986), large B values in ball-milled nanocrystalline materials have been frequently ascribed to some local strain (microstrain), a measure of which is obtained from diffraction line broadening (Sirdeshmukh D.B. 1993) (Purushotham E. 2010), with no further justification or proof of a real cause-effect linkage.

The present chapter investigates the DW coefficient of an extensively ball-milled iron alloy powder. The modelling of the synchrotron radiation XRPD patterns collected at three temperatures (100, 200, 300K), complemented by EXAFS results for the same sample, provides values of DW coefficient definitely smaller than those of the above cited literature. With the support of simulations of nanocrystalline iron clusters made by MD this work sheds light on the origin of the increased B with respect to bulk values, and on the role of the correlated displacement of neighbor atoms.

3.3 EXPERIMENTAL

The studied sample is an Astaloy Mo powder (Fe-1.5wt%Mo, FeMo), extensively ground (64h) in a Fritsch P4 planetary ball mill. Details on the grinding process and resulting powder can be found in (Rebuffi L. 2016) for the

experimental part and electron microscopy, whereas (Broseghini M. 2016) deals with a kinetic modelling of the mill used in the optimization of the grinding process.

XRPD data were collected at 11-BM, the powder diffraction beamline of Argonne National Laboratory (Advanced Photon Source) based on the Debye-Scherrer geometry. The X-ray beam of nominal energy 30 keV (actual wavelength λ= 0.0413679 nm) was diffracted by a FeMo powder specimen loaded in a kapton capillary (radius, R=0.15 mm), using a detector assembly consisting of 12 independent Si (111) analyzers and as many scintillation counters. The 2θ sampling step was 0.005°, over a 2θ range from 0° to 55°, with a counting time of 0.3 seconds per step.

The capillary mount is particularly convenient to collect reliable intensity values, provided that absorption is sufficiently low, so that data corrections can be avoided. In fact, expressions to correct intensity for absorption are known (Maslen E.N. 2006) but require information on the density of the specimen, which is hardly known, especially in a spinning capillary. Therefore, to limit absorption the powder was diluted in carbon black, and just lightly pushed in the capillary, enough to hold steady on spinning but still low density. Preliminary absorption measurements were made at 22.163 keV, using X-rays from a sealed tube with Ag anode. Based on the direct measurement of linear absorption coefficient, μ, we could estimate $\mu \cdot R$ <0.1 for the 30 keV of 11BM, a value sufficiently low to make absorption corrections unnecessary. XRPD data on the same sealed capillary were collected at 100K, 200K and 300K, in sequence, using an air blower to condition the capillary temperature.

The Instrumental Profile (IP) was also experimentally evaluated, collecting the pattern of NIST SRM660a (LaB6) (Cline 2000) under comparable conditions. The IP was parameterized, in terms of 2θ-dependent trends of width and shape of a pseudo-Voigt line profile fitting the experimental data. Also, the contribution from the kapton capillary and air scattering was carefully evaluated: the pattern of a blank capillary was fitted by seven pseudo-Voigt functions, enough to reproduce empirically the pattern, and the resulting model was adapted as background to the ball-milled FeMo data by means of a refinable scaling factor.

The XAFS measurements using the transmission mode have been performed at the XAFS beamline of Elettra synchrotron in Trieste, Italy. The XAFS beamline is installed on a bending magnet source and it is dedicated to the X-ray absorption spectroscopy experiments between 2.4 and 27 keV (Di Cicco A. 2009). A homogenous pellet for the ground FeMo sample was prepared by mixing a fixed amount of FeMo together with Polytetrafluoroethylene membrane and then the mixture was subjected to low applied pressure to prepare a solid disk. The XAFS measurements were done at the K edge of Fe (i.e. E = 7112 eV) while the energy scan ranged from 6912 eV to 8638 eV, with an energy step varying from 0.2 at the near edge region to 5 eV at the extremes of the spectra. The incident and transmitted intensities were measured by two ionization chambers, respectively before and after the sample. For better statistics, several scans were collected on the sample at room and at liquid nitrogen temperatures.

Further details are reported in the article (Scardi P 2017)

3.4 Numerical Simulations

Atomistic simulations of a cluster made of iron nanocrystals were performed via Molecular Dynamics, using LAMMPS and EAM. An ideally crystallographic microstructure of 50 iron crystallites was generated by dividing the space within a cubic box with periodic boundary conditions (PBC) using a modified Voronoi tessellation algorithm (A. S. Leonardi 2012) and filling each tessellation cell with randomly oriented periodic structure (i.e., bcc 2.86650 Å unit cell). The space tessellation was evolved (A. L. Leonardi 2013) by constraining the cluster to follow the lognormal distribution of diameters experimentally determined by XRPD. Thus, the ideal system was energy minimized by iteratively adjusting atom coordinates, and then equilibrated with a 0.6 ns dynamics up to reaching a steady state at constant pressure (0 Pa) and temperature (300 K), using Nose-Hoover style non-Hamiltonian thermostat (Martyna 1994) (Parrinello M. 1981) (Shinoda 2004) (Tuckerman Alejandre 2006) with a 1 fs time integration and Fe EAM pair potential (Mendelev M.I. et al. 2003). Next, a set of uncorrelated arrangements of atomic positions in space (i.e., frames) were recorded at 2 ps time steps for 0.2 ns long dynamics

(i.e, 100 frames time trajectory). The time average configuration was thus computed to cancel the dynamic component out of the lattice distortion field.

PBC employed in MD simulations were removed, recovering the continuity of the structure within the crystalline domains. Furthermore, the crystallites were rigidly translated by the PBC length so to minimize the surface-to-volume ratio of the resulting polycrystalline microstructure (i.e., an average spherical shape). Next, XRPD patterns were simulated by the Debye Scattering Equation for all the frame configurations and their average over the time trajectory. The profiles for the uncorrelated frames were finally summed to obtain an experimental-like XRPD pattern, accounting for an effective real-life measurement time. Normalized by the number of frames and atoms, respectively the averaged positions (AP) and time average (TA) profiles were therefore different only for the dynamic contribution to the line broadening (i.e., Thermal Diffuse Scattering,). XRPD patterns for every single crystal were also recorded while calculating the profiles for the whole microstructures. Thus, the XRD pattern for an ideal powder made of monodisperse domains like a randomly chosen crystallite was obtained, neglecting inter-crystallite interference contribution to the observed XRPD profiles.

The Radial Pair Distribution Function was calculated over 100 frames along the MD trajectory, using the software VMD.

3.5 Results and Discussion

Diffraction data collected at the three temperatures (100, 200, 300K) were analyzed by WPPM, following the procedure outlined in (Rebuffi L. 2016). Line profiles of the *bcc* FeMo phase ($I_{hkl}(Q)$) were modelled assuming their Fourier Transform to be made of three contributions, respectively from IP ($A^{IP}(L)$), finite domain size ($A^{S}(L)$), and inhomogeneous strain, or microstrain, ($A^{D}_{hkl}(L)$) (P. Scardi, Microstructural Properties: Lattice Defects and Domain Size Effects 2008):

$$I_{hkl}(Q) \propto \int A^{IP}(L)A^{S}(L)A^{D}_{hkl}(L)\, exp(iQL)\, dL \qquad (3\text{-}2)$$

where *hkl* are the Miller indices of the modelled peak profile, $Q = 4\pi\sin(\theta)/\lambda$, with θ as the diffraction angle and λ the X-ray wavelength, and *L* the Fourier length, distance between any two scattering centers along [hkl]. The proportionality factor includes the usual trigonometric terms of the Lorentz-polarization factor with known constants and the square modulus of the structure factor corrected for temperature effects by the DW factor (Warren, X-Ray Diffraction 1990). Crystalline domains were assumed to be spherical, with diameters distributed according to a lognormal distribution with lognormal mean (μ) and standard deviation (σ) as refinable parameters.

The microstrain term can be expressed according to the Krivoglaz-Wilkens theory of dislocation line broadening, with average dislocation density, ρ, and effective outer cut-off, Re, as refinable parameters. Dislocations are expected in the primary slip system of iron, $\{110\}\langle 111\rangle$ (Burgers vector modulus $\left|\underline{b}\right| = a_0\sqrt{3/2}$, with unit cell parameter a_0), for which the average contrast factor is known (D'Incau 2007) for edge and screw type dislocations, so that the fraction of edge type dislocations, f_E, can also be refined. However, as pointed out recently (Rebuffi L. 2016) this model tends to overestimate the dislocation density, with 1.5÷2 dislocations per domain, well beyond the evidence of TEM. In this specific sample, as it is also probably true of many ball-milled metals, the inhomogeneous strain responsible for the anisotropic line broadening is only partly caused by line defects in the crystalline domains, whereas a large part of the effect is due to grain boundary regions, where dislocations get to in the deformation process, and to grain-grain interactions. It is therefore more appropriate to express the strain broadening result in terms of Warren plot, i.e., r.m.s. displacement of couples of unit cells, $\sqrt{\sigma_{hkl}^2}(L)$, for any given distance *L* in the crystalline domain along the [hkl] scattering direction. This provides a quantitative measurement but leaves open the interpretation of the microstrain effect as resulting from one or more sources (Rebuffi L. 2016).

The main focus of this work is on the Debye-Waller coefficient of the ball-milled FeMo powder, so the role of MSD/B was considered in detail. The DW coefficient appears in the traditional thermal factor depressing the Bragg intensity, which for a monoatomic cubic phase reads (Guinier 1963):

$$e^{-q^2 B_{ISO}/8\pi^2} = e^{-q^2\overline{u^2}/3} = e^{-q^2\overline{u_s^2}} \qquad (3\text{-}3)$$

where $\overline{u_S^2}$ is the projection of $\overline{u^2}$ along the [hkl] scattering vector direction for the given diffraction peak. In addition to this term, B also appears in the diffuse scattering component, which can be included in the WPPM following Warren's theory, as modified by Beyerlein *et al.* (Beyerlein 2012) to account for the phonon confinement effect enforced by the finite (small) domain size. Including the Temperature Diffuse Scattering (TDS) in the WPPM is important, as it gives more reliable B values as well as a more accurate modelling of the line profiles, without increasing the number of refined parameters.

Data modelling was made simultaneously on the patterns collected at different temperatures, sharing the same microstructural (size-strain) model, while independently refining for each pattern the DW coefficient ($B_{ISO}(T)$) and the unit cell parameter ($a_0(T)$). WPPM also included a second phase, a small fraction (≈2%) of austenitic (fcc) iron, undetected by previous studies. Besides a scaling factor, only the unit cell parameter of the austenitic phase was added as refinable parameter, all other microstructural and thermal parameters being shared with the main bcc phase, so to limit the number of free parameters.

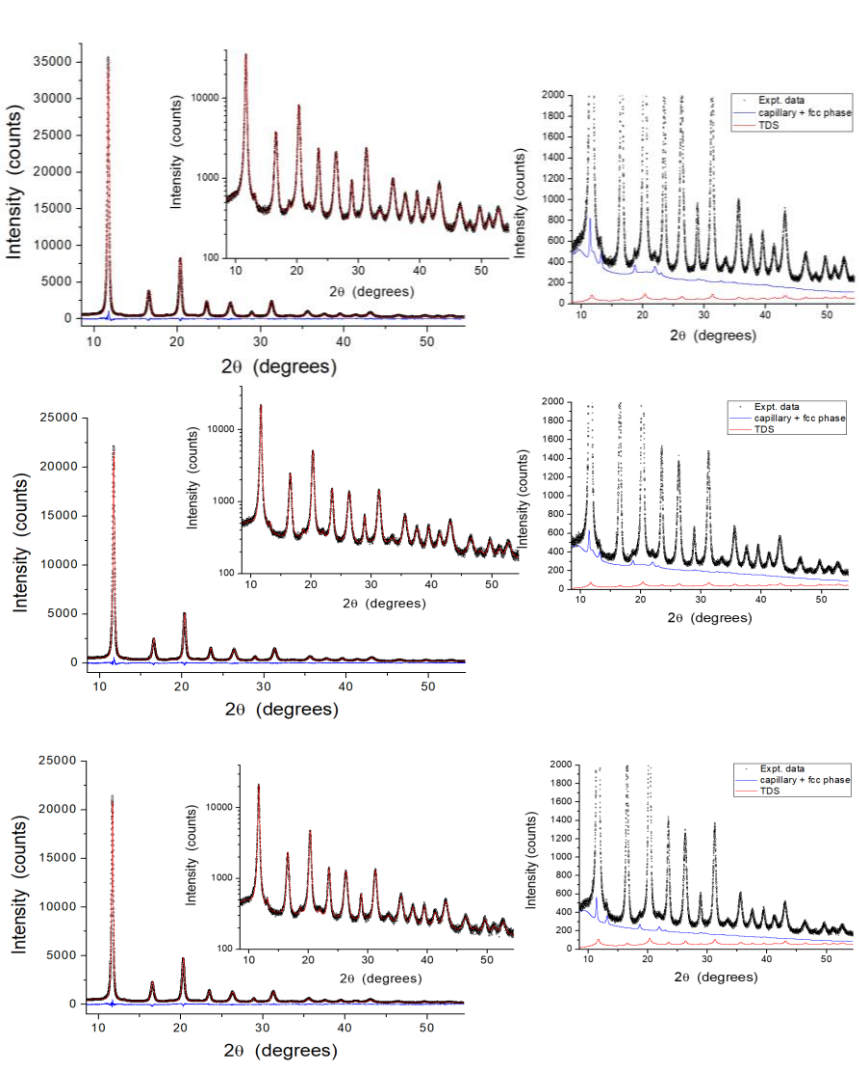

Figure 3-1

X-ray diffraction patterns of ball-milled FeMo powder at 100K (a), 200K (b), and 300K (c). Experimental data (circle) are shown together with the modelling (line), and their difference (residual, line below). WPPM details are shown in the left insets in log scale, whereas insets on the right show contributions from capillary and fcc minor fraction, and from the temperature diffuse scattering.

The XRPD patterns of the ball-milled FeMo sample are displayed in Figure 3-1 for the three studied temperatures (300K, 200K, 100K, respectively in (a), (b), (c)) together with the WPPM results. Insets highlight details in log scale (left), and a comparison of experimental data with the TDS, and the signal from capillary summed to the minor fraction of fcc phase (right). Further details on TDS and capillary contributions are reported in the Supplementary Materials.

Results of the WPPM are shown in Figure 3-2 (a)for the temperature-dependent parameters (B_{ISO}(T) and a_0(T)), whereas domain size distribution and Warren plot for three significant directions ([h00], [hh0] and [hhh]) are shown in Figure 3-2 (b). Mean domain size (8.2(2) nm) is smaller than in (Rebuffi L. 2016) (9.3(8)), as the present analysis includes the TDS, with the simultaneous modelling of patterns collected at three different temperatures with higher X-ray energy, and the austenitic phase. This minor fraction of fcc phase was likely stabilized by the Nickel contamination from the milling vial (Rebuffi L. 2016), and could only be detected for the high-quality counting statistics of the 11bm data. The r.m.s. displacement in Warren's plot, instead, is nearly identical with results of (Rebuffi L. 2016).

B_{ISO}(T) values for the ball-milled sample are about 20% higher than the reference values for bulk iron, also shown in Figure 2a as a dash line, together with the value for the pristine FeMo powder at ambient T: B_{ISO}(300K) for the pristine FeMo powder is 0.358(10) Å^2, whereas the literature value for bulk Fe is 0.35(1) Å^2 with Θ_D=431(6)K (Butt 1988), against 0.417(3) Å^2 for the ball milled FeMo. It is worth mentioning here that the 1.5wt%Mo in the ball milled powder, equivalent to 0.88 at%Mo, gives a negligible contribution to the average DW factor (using a rule of mixtures, B_{ISO}(300)=0.349 Å^2 for the bulk FeMo phase), so we refer to pure-iron data with no further specification in the context of this work.

Both trends in Figure 3-2 (a), B_{ISO}(T) and a_0(T), show the expected non-linearity toward the low T limit, where quantum effects, and zero-point energy in particular, become relevant. Since the experimental evidence we could gather is limited to three data points, only modelling of B_{ISO}(T) we can credibly afford is by the Debye theory. In fact, MSD/B can be modelled as:

$$B(T) = B_S + B_0(\Theta_D) + B_T(\Theta_D, T) \qquad (3\text{-}4)$$
$$= B_S + \frac{6h^2}{m\, k_B \Theta_D}\frac{1}{4} + \frac{6h^2}{m\, k_B \Theta_D}\left(\frac{T}{\Theta_D}\right)^2 \int_0^{\frac{\Theta_D}{T}} \frac{\xi}{exp(\xi) - 1} d\xi.$$

With B_S, the static component of the DW coefficient, and Θ_D, as parameters to be adjusted. The best fit, shown in Figure 3-2 (a) as a full line, gives B_S=0.02 and Θ_D=420K. It can be noticed that the difference between the bulk reference (dash) and the ball-milled sample (line) tends to increase slightly toward high (300K) temperature, which is a detail already mentioned in the cited works based on LEED and Mössbauer spectroscopy. This is a consequence of the surface softening effect, which determines the lower Debye temperature with respect to the bulk reference.

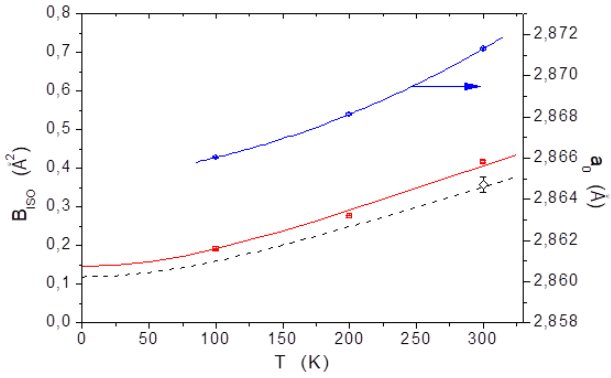

a)

Figure 3-2

Temperature dependent parameters from the modelling of Figure 3-1: $B_{ISO}(T)$ (left axis) and $a_0(T)$ (right axis) (a); $B_{ISO}(T)$ trend from best it of eq. (3-4) (line) is shown together with the literature data for bulk Fe (Butt 1988)(dash), whereas the $a_0(T)$ trend (line) is a parabolic function just to drive the eye. Domain diameter distribution (left axis) and Warren plots (right axis) are shown in (b). See text for details

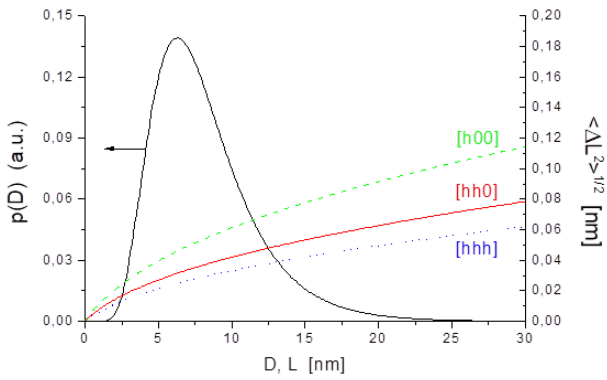

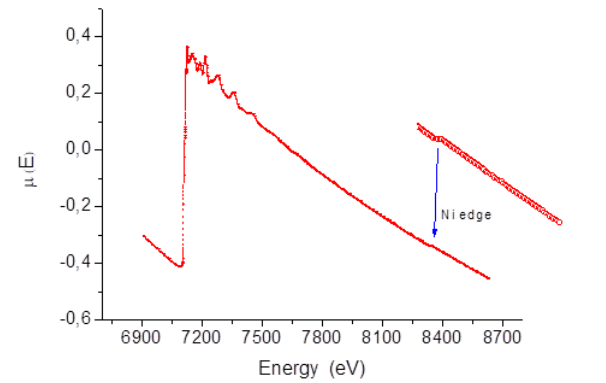

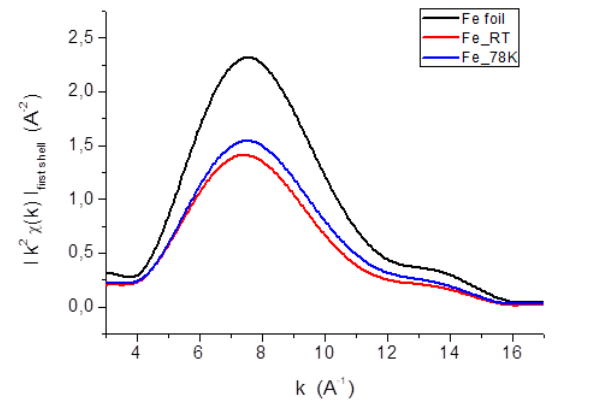

Figure 3-3

EXAFS measurements around the Fe K edge at 7110 eV, with detail of the additional edge by the nickel contaminant (a); the amplitude signal of the back Fourier transform of $k^2\chi(R)$ corresponding to the first shell. (b).

Similar evidence is provided by EXAFS measurements made on the same capillary with ball milled FeMo powder and, for comparison, on a pure Fe thin foil used as standard. As shown in Figure 3-3, absorption was measured around

the Fe K edge at 7.11 keV. The same measurement confirms the presence of Ni contamination from the mill (jar), which is deemed responsible for the formation of a minor fraction of austenitic γ-phase.

EXAFS data were analyzed considering the first coordination shell, using a Fe foil as standard material with known structural parameters (Sevillano E. 1979). According to the Ratio Method (Schnohr C.S. 2015), the amplitude of Fourier transform of the normalized EXAFS function $\chi(k)$ Figure 3-3 (b) for the first shell of the ball milled FeMo was divided by the corresponding amplitude for the foil; the result is a linear function of the square of the wavenumber vector modulus (*k*), whose slope gives the difference of Debye-Waller factors.

The DW coefficients of EXAFS and XRPD have quite different meaning (Dalba G. 1997) (Fornasini 2014), the main difference arising from the different average involved in the corresponding definitions. While the EXAFS value of our study refers to the first coordination shell (eight neighbours in the ideal bcc Fe), the XRPD value is an average over the whole system, which according to Debye's model involves all 3N vibration modes in a bcc domain with N iron atoms.

The DW coefficient of EXAFS is a parallel MSRD, $\overline{\sigma_{\parallel}^2}$, defined as the variance of the distribution of distances between absorber and back scattering atoms (Calvin 2013). For totally uncorrelated atomic displacements (Einstein oscillators), the MSRD is equal to twice the MSD component projected along the direction joining absorber and back scattering atom, which is equivalent, with a good level of approximation, to $\overline{u_s^2}$, the DW coefficient provided by XRPD. In the general case where atomic displacements are correlated, the MSRD can be written as:

$$\overline{\sigma_{\parallel}^2} = \mathrm{MSRD} = 2 \cdot \overline{u_s^2} - DCF \qquad (3\text{-}5)$$

Which is analogue to eq. (1-21)

In eq. (3-5) the difference between twice the MSD and MSRD defines the Displacement Correlation Function (DCF). Experimentally determined $2 \cdot \overline{u_s^2}$, from B_{ISO} values and eq.(3-1), and MSRD for iron first shell are shown in Figure 4 as a function of temperature. While the first-shell MSRD is weakly affected by the temperature, $2 \cdot \overline{u_s^2}$ increases quite steeply, the difference between the

two quantities being caused by the strong correlation of atomic displacements in the first coordination shell.

As shown by Jeong et al. (Jeong 2003), atomic vibrations of bulk iron can be described by a Born–von Karman (BvK) force model (Born M 1954). By solving the dynamical matrix using up to the fifth nearest-neighbor interatomic force parameters, the DCF of the first shell is 42% of $2 \cdot \overline{u_s^2}$. Then, according to Eq. (3-5), Butt's value of $\overline{u_s^2}$ = 0.00443 Å^2 for reference bulk iron (Butt 1988) corresponds to a first shell MRSD = 2·0.00443·(1 - 0.42) = 0.00511 Å^2, in good agreement with the experimental EXAFS results of Sevilliano (0.00506 Å^2) and following literature (Jiménez-Villacorta 2004).

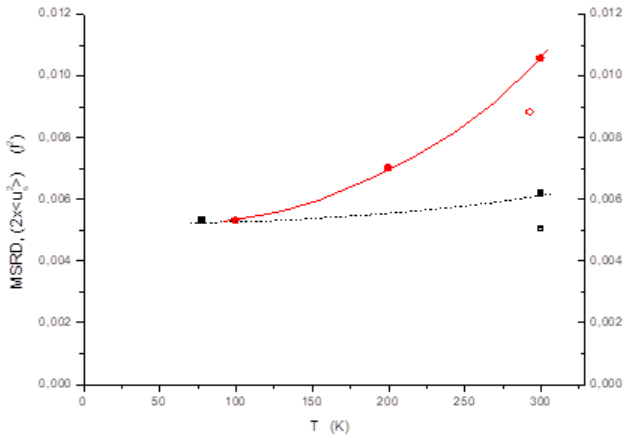

Figure 3-4

MSRD of Fe first coordination shell from EXAFS measurements at 77K and 298K (Figure 3-2 and Figure 3-3) (square).

Values of $2 \cdot \overline{u_s^2}$ (circle) are obtained from XRPD values of B_{ISO} in Figure 3-2, using eq.(3-1). Full symbol: ball milled FeMo; open symbols: pure iron foil (EXAFS, square) and literature value for bulk iron (circle) [Butt].

If the same argument is used for the ball-milled FeMo, a similar agreement is obtained between first shell MSRD from BvK model and EXAFS experiments. More in detail, the MSRD shows a 20% increment from bulk reference (Figure 4, empty square, 0.00504(5) Å^2) to ball milled FeMo (full square, 0.00619(1) Å^2), thus confirming the effect of the static disorder component also according to EXAFS, in the same amount shown by the XRPD results ofFigure 3-2(a). XRPD and EXAFS results of DW coefficient are therefore in good agreement, pointing out a static disorder component compatible with LEED and Mössbauer observations (Kuwano H. 1992). Quite differently, literature data of B_{ISO} appear overestimated (Azzaza S. 2015), probably because of experimental as well as modelling errors. XRD measurements of B_{ISO} require a strict control of all

factors – absorption as first - affecting the diffracted intensity; moreover, as pointed out by Vetelino et al. (Vetelino J.F. 1972), accounting for the TDS in the XRPD data modelling is important, and failing to do so could be a further reason for the quite high B_{ISO} values reported in the literature (Zhao 1999) (Azzaza S. 2015) (Sirdeshmukh D.B. 1993) (Purushotham E. 2010).

To add a further point of view and interpretation of the experimental results, and to assess the origin of the observed increase in DW coefficient, a system similar to the ball milled FeMo was simulated by Molecular Dynamics. As explained in the Numerical Simulations paragraph, a cluster of 50 grains was generated by a modified Voronoi tessellation procedure. Atomistic model of iron grains are polyhedra with same volume as the spherical grains of the distribution of Figure 2b refined by WPPM. Grain number 5, highlighted in Figure 3-5, is the average-size crystalline domain with 66874 Fe atoms. The 50 grain cluster in Figure 3-5 is shown with the detail of each grain, but in the actual MD simulations PBC were enforced, so that each grain, and grain number 5 in particular, experience an environment similar to that of the real material.

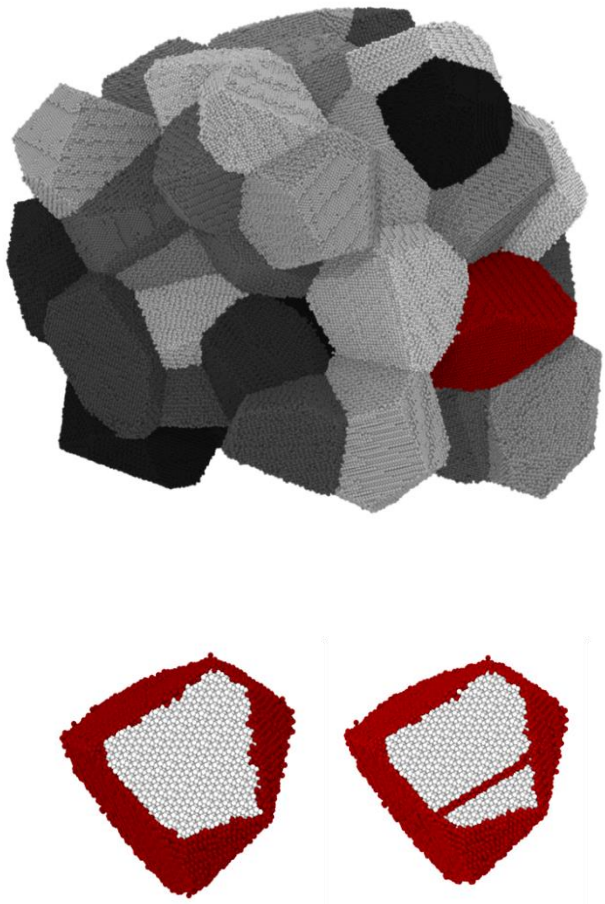

Figure 3-5

Molecular Dynamics model of the studied system, made of 50 grains of Fe with a size distribution mapped on the experimental result of WPPM shown in Figure 3-2 (b).

Below, detail of grain number 5, the average-size crystallite with 66874 Fe atoms (left), and the same grain with an edge dislocation (right). See text for details

To assess the effect of the microstructure on B_{ISO} /MSD we followed a procedure similar to that of (Rebuffi L. 2016). The XRPD patterns of an ideal powder made of crystalline domains like those observed in HRTEM images for the ball-milled FeMo powder sample (Rebuffi L. 2016) were simulated and investigated. Simulated patterns were treated as 'experimental' patterns, and analyzed by the same WPPM used for the experimental data of the ball-milled FeMo powder. In this case, however, the crystalline domain is known so the domain size effect can be modelled to perfection by using the CVF for the specific polyhedral shape of the grain. As an example, Figure 3-6 (a) shows the 'experimental' pattern and WPPM when the size effect only is present, that is

for an isolated (geometrical) model of grain number 5, with atomic positions matching a perfect bcc lattice (no MD potential used yet). The match between data and modelling is nearly perfect, showing that the domain size/shape effect is correctly treated by WPPM using the CVF of the studied grain. Figure 3-6 (b) shows the modelling result after energy minimization and equilibration of the system free of line defects, e.g., after 0.6 ns of MD trajectory, time sufficient to drive the 50 grain cluster in a steady state under the EAM potential at 300K. The TA powder pattern, obtained from the atomic coordinates of the same grain sampled at several time steps along the MD time trajectory, includes static and dynamic disorder, the former being caused by the grain boundary and grain-grain interactions, while the latter is the effect of temperature. Using again the same modelling as for the experimental ball-milled FeMo powder, the refined DW coefficient is B_{ISO} = 0.4513 Å^2. This is slightly higher than the experimental value of Figure 3-2(a), and the discrepancy can be ascribed to the model as well as to the EAM potential, which is not specifically designed and optimized for thermal properties of iron (Mendelev, private communication). However, the interesting point is that when the procedure is repeated on the AP powder pattern, simulated using average atomic coordinates (i.e., by averaging coordinates of the same grain sampled at different instants along the MD trajectory) so to average out all dynamic effects, B_{ISO} falls down to 0.082 Å^2. This refined value can be taken as an estimate of the static-disorder component of B/MSD, due to the effect of grain boundary and grain-grain interactions in the 50 grain cluster. B_{ISO} for the dynamic disorder can be estimated as 0.4513-0.082 = 0.369 Å^2, not far from the experimental value for bulk iron (0.35 (Butt 1988)). Therefore, B_{ISO} from the AP powder pattern is about 20% of B_{ISO} for dynamic disorder only, in good agreement with the experimentally observed increment of B_{ISO} and MSRD of ball milled FeMo with respect to reference bulk Fe.

MD simulations also provide a direct measurement of the MSRD, given by the variance of the distributions centred about each shell in the Radial Pair Distribution Function of grain number 5.

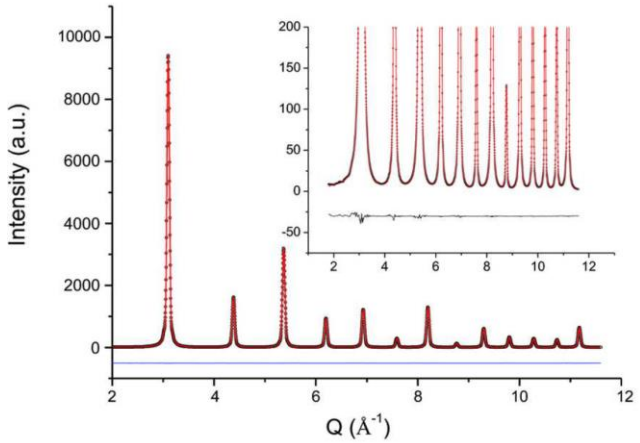

a)

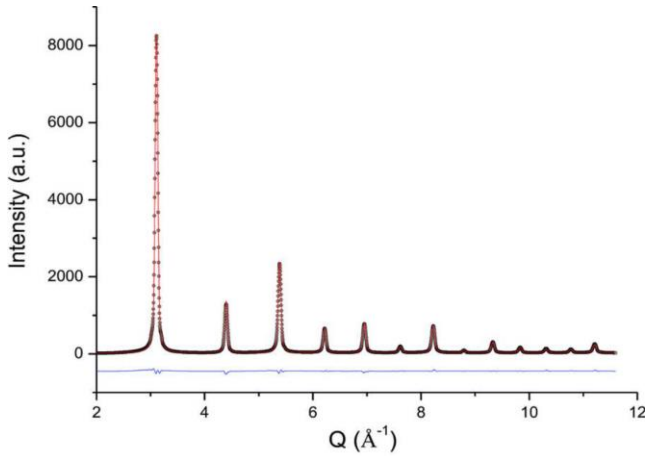

b)

Figure 3-6

X-ray Powder Diffraction Patterns generated by the Debye Scattering Equation using atomic coordinates of MD simulations (circle) with corresponding WPPM result (line) and difference (residual, line below) for: geometrical (ideal perfect crystal) model of grain number 5, with details in the inset (a); same grain after energy minimization and MD trajectory (b); same grain as in (b), with an edge dislocation across (c); same as (c) with $c_V = 10^{-3}$ vacancy concentration (d).

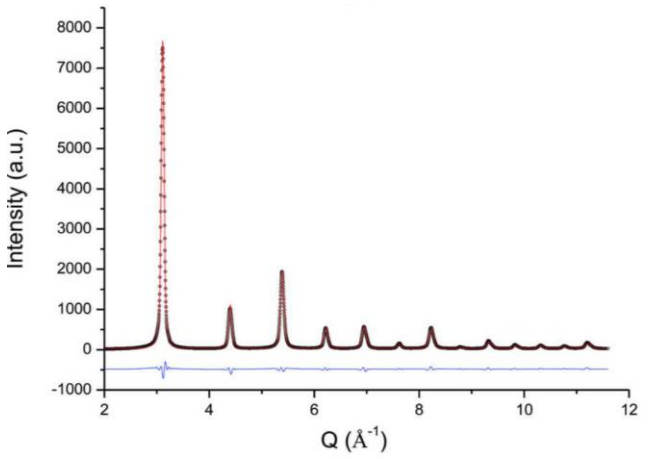
Intensity (a.u.)
8000
7000
6000
5000
4000
3000
2000
1000
0
-1000
2
4
6
8
10
12
Q (Å^{-1})

c)

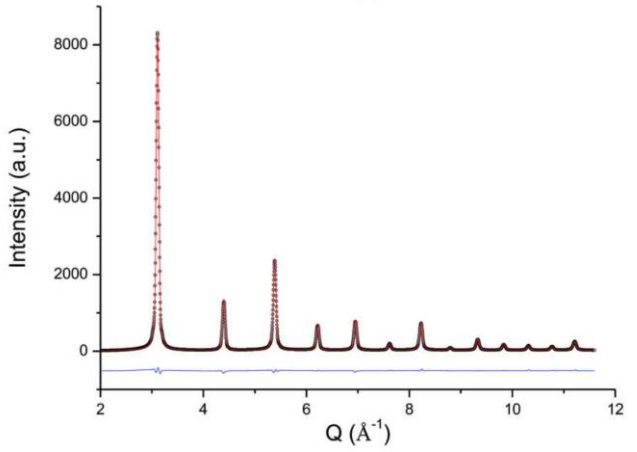
Intensity (a.u.)
8000
6000
4000
2000
0
2
4
6
8
10
12
Q (Å^{-1})

d)

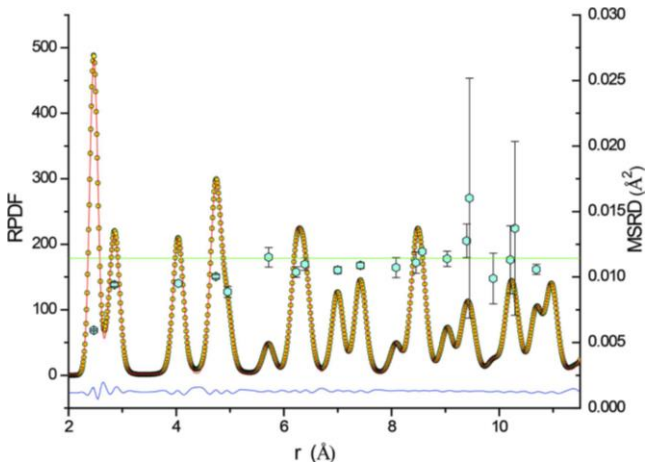

Figure 3-7

Left axis: Radial Pair Distribution Function from MD simulation of grain number 5 (circle), and fitting with Gaussian distributions (red line) centred about the shell radii of neighbour atoms at increasing distance (first 20 neighbours); the difference (residual) is shown by the line below. Right axis: corresponding MSRD values, given by the variance of the Gaussian distributions (diamonds), and asymptotic value, $2 \cdot \overline{u_s^2}$ from the refined value of DW coefficient, $B_{ISO} = 8\pi^2\overline{u_s^2}$ = 0.4513 Å² (green horizontal line).

As shown in Figure 3-7, despite the anharmonicity of the EAM potential, symmetrical Gaussians give an acceptably good fit. As expected, atomic vibrations of first neighbours are strongly correlated, with the asymptotic value of $2 \cdot \overline{u_s^2}$ (horizontal line, provided by the refined value of $B_{ISO} = 8\pi^2\overline{u_s^2}$ = 0.4513 Å²) far from being approached by the MSRD of the nearest neighbour shells. The trend is in good agreement with that reported by Jeong *et al.*, with a first shell DCF about 5% larger than reported by those authors [Jeong]. Discrepancy can be attributed to the different models (MD with EAM potential vs BvK model up to fifth nearest neighbour), but also to the finite dimensions of grain number 5, as opposed to the perfect bulk Fe of Jeong *et al.*.

Simulation results add credit to the interpretation according to which the observed increase of B_{ISO} is due to the grain boundary under-coordination, as also pointed out by LEED and Mossbauer experiments (Inagaki M. 1983) (Clark B.C. 1965) (VanHove M.A. 1986) (Eynatten G. Von 1977) (Kuwano H. 1992), and other studies on plastically deformed materials (Valiev R.Z. 2000).The MD approach described above is also useful to assess the effect of lattice defects of

lower dimensionality. Once the grain boundary effect is known, we can repeat the procedure with an edge dislocation created and stabilized by MD inside the same grain (Figure 3-5(c)). The powder pattern was simulated according to the procedure explained above, to produce 'experimental' data now including thermal effects, grain boundary and grain-grain interaction, and the effect of an edge dislocation in the primary slip system of iron. The WPPM result, shown in Figure 3-6 (c), gives a B_{ISO} increment of just 2% for the presence of the dislocation.

The same procedure and refinement was then made including vacancies in the cluster. With a vacancy formation enthalpy ΔH_v = 1.41 eV for iron (Buyers 1978), the thermodynamically stable fraction at 300K would be totally negligible. Even at melting point (1808K) vacancy concentration is just $c_V = 1.2\ 10^{-4}$, which corresponds to a few vacant sites only in grain number 5. In order to give an upper bound to the possible effect of vacancies on B_{ISO}, simulations were made overestimating the concentration, considering extrinsic contributions like generation of excess vacancies by the dislocation dynamics during plastic deformation. A concentration $c_V = 10^{-3}$ was used, corresponding to 75 vacant sites over the 66874 atoms of grain number 5. The result of the modelling of the powder pattern including thermal effects, grain boundary and grain-grain interaction, and the effect of the overestimated vacancy fraction is shown in Figure 3-6 (d). Vacancy effects on the modelling were just minor, with no measurable increase in B_{ISO} (<1%) with respect to the same powder pattern with no vacancies at all.

These results clearly point out the dominating effect of coordination on the value of DW coefficient. In fact, the experimentally observed increase of B_{ISO} from reference bulk Fe to ball-milled FeMo, matches quite well the static disorder component that MD proved to be caused by a surface effect, were 5642/66874 atoms are involved in the surface (under-coordinated Fe atoms on the surface of grain number 5). When a full dislocation line is included in grain number 5, that amounts to removing 999/66874 atoms, with a much lower under-coordination effect than grain boundary, increasing B_{ISO} by just a 2%. Finally, when randomly removing atoms to create point defects, even well above the equilibrium concentration (75/66874 atoms), effects on B_{ISO} refined by WPPM are below the sensitivity of the technique.

Therefore, there appears to be a hierarchy in the effect of lattice defects on B_{ISO}, mostly determined by the different, increasing amount of under-coordinated atoms, following the sequence point-line-surface defects. As shown in this work, and in agreement with earlier research based on surface-sensitive techniques like LEED and Mossbauer, the experimentally observed increase of B_{ISO}/MSD in nanocrystals and plastically deformed nanocrystalline aggregates should not be directly related to a generic 'microstrain' effect. The correlation between B_{ISO} and increased microstrain, frequently proposed in the literature, appears to be just coincidental, as the microstrain frequently increases inversely proportional to the domain size. Domain size and extension of grain boundary (or free surface) is indeed the real quantity determining the static disorder, for the under-coordination effect of grain boundary or surface atoms.

As a further test to assess the contribution of grain boundary to static disorder and increased DW coefficient, the powder pattern and WPPM analysis of Figure 3-6 (b) was repeated after removing 1, 2 or 3 layers of atoms from the surface of grain number 5. As shown in Figure 3-8, B_{ISO} decreases quickly with the surface layer removal, tending to the asymptotic value for bulk Fe. The same decreasing trend is obtained both with TA patterns (which include static and dynamic disorder) and with AP patterns (where dynamics effect is averaged out). The layer removal procedure has a peculiar effect on the powder pattern. If patterns are plotted in Log scale to highlight the low-counts region, it is quite evident that removing atomic shells from the grain boundary region inward drastically reduces the TDS; in addition to a slower decay of Bragg scattering intensity with Q, the patterns show a lower diffuse background when atom layers are removed from the surface. This detail further confirms the importance of a proper evaluation of the TDS if reliable values of DW coefficient are of interest.

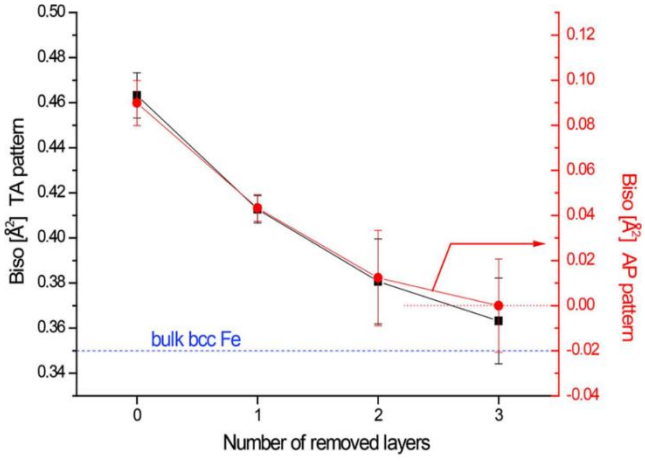

a)

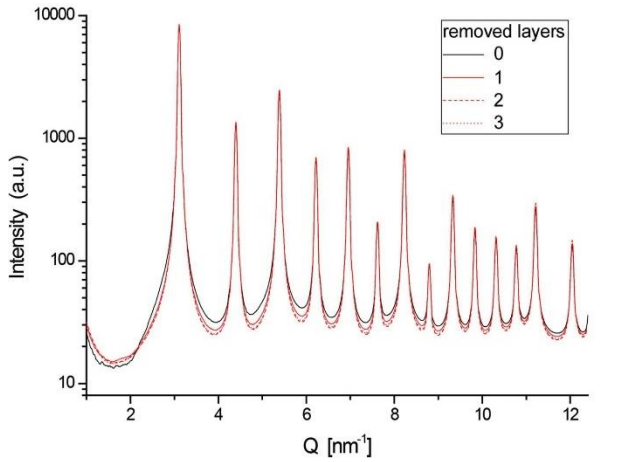

b)

Figure 3-8

B_{ISO} values from WPPM of powder patterns generated by the DSE using MD atomic coordinates, for grain number 5 after removal of increasing number of surface layers (from 0 to 3 layers); results in (a) are shown for TA patterns (left axis) and AP patterns (right axis), with quite similar trends; dash line shows the reference value of B_{ISO} for bulk iron [Butt]. DSE simulated patterns for grain number 5 and after progressive shell removal are shown in (b).

3.6 Concluding Remarks

Synchrotron radiation XRPD and EXAFS patterns from an extensively ball-milled FeMo powder were collected at different temperatures. Measurements and data analysis were made paying special attention to all effects influencing the

scattered intensity, as possible sources of errors in the determination of the DW coefficients. Main points of interests are:

(i) despite the intrinsic differences between DW coefficients of XRPD and EXAFS, both show a ~20% increase between bulk reference iron and ball milled FeMo powder; this increment is compatible with experimental observations made by LEED and Mossbauer spectroscopy, more sensitive to the surface layers than XRPD and EXAFS, which provide information based on average over the studied volume of crystalline domains;

(ii) B_{ISO}/MSD values of our study are markedly lower then reported in many literature studies based on XRPD; according to the evidence shown by this work, literature values of B_{ISO} for nanocrystalline iron appear to be overestimated, either for experimental errors (e.g., due to unaccounted absorption effects) or for lack of consideration of the Temperature Diffuse Scattering;

(iii) the present results, in agreement with the conclusions of LEED and Mossbauer studies, support an interpretation according to which the increased B_{ISO}/MSD in ball milled nanocrystalline FeMo is mostly caused by the under-coordination of atoms in the grain boundary region. This result is confirmed by atomistic modelling of the studied system. A cluster of plastically deformed nanocrystalline domains of mean size around 8-9 nm was treated by Molecular Dynamics using the Embedded Atom Model; the analysis of powder diffraction patterns simulated by the Debye Scattering Equation using atomic coordinates from MD trajectories demonstrates the main role of surface effects in determining the static disorder contributions to B_{ISO}/MSD.

APPLICATION: CORRELATED DEBYE MODEL FOR ATOMIC MOTIONS IN METAL NANOCRYSTALS

Part of this chapter is based on the published article:

"Correlated Debye model for atomic motions in metal nanocrystals", P. Scardi, A. Flor, *Philosophical Magazine.Volume 98, Issue 15, 1412-1435. January 2018.*

https://doi.org/10.1080/14786435.2018.1435918

4.1 INTRODUCTION

Interatomic forces are responsible for correlated atomic motions which constrain the vibrational modes and amplitudes in crystals and influence the thermal properties. Several models have been proposed to study this effect in near-neighbour coordination shells, like the classical Born–von Karman force model (Jeong 2003) and, in more recent times, atomistic simulations. MD, for example, can simulate relatively large (millions of atoms) portions of simple inorganic materials as well as complex biological systems (Briki F. 1994) (Kamberaj H. 2009) (Molecular Dynamics - Studies of Synthetic and Biological Macromolecules 2012). In the context of polycrystalline inorganic materials, EXAFS is the reference technique to study the local atomic motion, providing detailed information on the Debye-Waller coefficients parallel and perpendicular to the bond axis, for the innermost coordination shells (Fornasini 2014). Besides X-ray absorption, elastic scattering can also give information on correlated motions by the Total Scattering approach (pair distribution function analysis (Jiawei Zhang 2016) (Egami T. 2003) or pattern modelling by the Debye Scattering Equation (DSE) (a. L. Scardi P. 2016)), although the relevance of the information is more statistical, averaged over all coordination shells, while EXAFS has a strong point in resolving the local atomic environment of the inner shells.

Since the early times of EXAFS, accounting for lattice dynamics has been a known issue, and the complexity of the problem of analysing powder (polycrystalline) materials has led to the Correlated Debye (CD) model (Beni G. 1976) to approximate the degree of correlation of atomic vibrations as a

function of the distance between the atoms. The model, although limited by the harmonic approximation, is still popular today (Vaccari M. 2006) and provides an expression for the mean-square relative displacement (MSRD) according to the classical Debye model, under the same hypothesis of the well-known theory of specific heat (Dove M. 2003).

The CD model of Beni & Platzman has been derived for an infinite lattice, which is an approximation suitable to analyse data from bulk crystals. In the analysis of small crystals it is generally recognised that the vibrational properties change (Di Cicco A. M. Berrettoni 1994) (Suzuki Y. 2005) (M. N. Miyanaga T. 2012), and the DW factor, e.g. in metals, tends to increase when the crystalline domain size decreases (see (Kuzmin A. 2014) (Agostini G. 2013) and references therein), an effect so far unaccounted for by the CD model. As shown in this work, an extension of the CD model to nanocrystalline materials is straightforward. Even if the traditional CD is discussed in the literature, part of the derivation is proposed again here, to underline all approximations and introduce the extension to the nanoscale. Examples are shown for the specific case of MD simulations of Pd, but the validity of the model extends to any simple metal. Besides MD simulations, the model was tested on experimental data for nanocrystalline Pt (Shi C. 2013).

4.2 Mean square displacement and traditional Correlated Debye model

To introduce the formalism of the Correlated Debye Model, it is better to reformulate the expressions of paragraph 1.4.1.

Atomic positions can be written in terms of an average (constant) position, $\underline{r_i}$, plus a time dependent displacement, $\underline{u_i}$, such that the distance between any two atoms is:

$$\underline{r'}_i(t) - \underline{r'}_j(t) = \underline{r}_i - \underline{r}_j + \left[\underline{u}_i(t) - \underline{u}_j(t)\right], \qquad (4\text{-}1)$$

or, in compact form,

$$\underline{r'}_{ij}(t) = \underline{r}_{ij} + \underline{u}_{ij}(t).$$

As already pointed out, some spectroscopic techniques provide information on the correlation between atomic displacements. This often concerns a projection of the displacement along a given direction, like $\hat{r}_{ij} \cdot \underline{u}_{ij}$, expressing the difference of atomic displacement of any two atoms, $\underline{u}_{ij}$, projected along their distance, represented by versor $\hat{r}_{ij}$ (see Figure 4-1). The variance of the distribution of such displacements is the parallel MSRD, given by:

$$\overline{\sigma_{ij}^2} = \overline{\left[\hat{r}_{ij} \cdot (\underline{u}_i - \underline{u}_j)\right]^2}. \qquad (4\text{-}2)$$

Eq.(4-2) can also be expanded as

$$\overline{\sigma_{ij}^2} = \overline{(\hat{r}_{ij} \cdot \underline{u}_i)^2} + \overline{(\hat{r}_{ij} \cdot \underline{u}_j)^2} - 2\overline{(\hat{r}_{ij} \cdot \underline{u}_i)(\hat{r}_{ij} \cdot \underline{u}_j)}, \qquad (4\text{-}3)$$

where the first two terms on the right side are the (uncorrelated) *MSD*, respectively of atoms *i* and *j*, along their distance, and the last term is twice the *DCF*, also related to (i.e., projected along) the distance of the two atoms (Beni G. 1976). In monoatomic crystals,

$$\overline{\sigma_{ij}^2} = 2\,MSD_r - 2\,DCF \qquad (4\text{-}4)$$

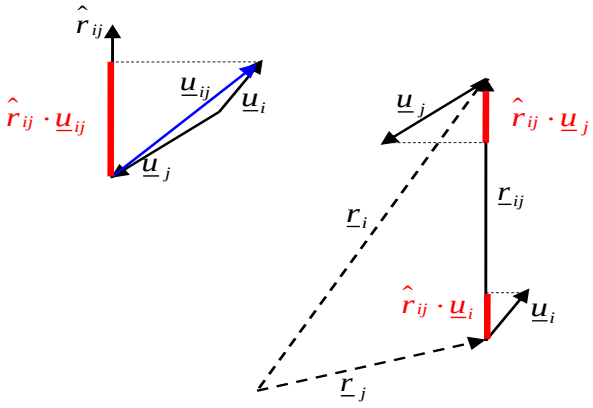

Figure 4-1

Atomic positions and displacement (centre).

Graphical representation of $\hat{r}_{ij} \cdot \underline{u}_{ij}$ (left) and of $\hat{r}_{ij} \cdot \underline{u}_j$ (right); $\hat{r}_{ij}$ is the versor (unit vector) along $\underline{r}_{ij}$ direction. See text for details.

It is worth underlying that the MSRD refers to couples of atoms, whereas the MSD, labelled as MSD_r, in this context refers to individual uncorrelated atoms;

and in both cases the displacement component considered is projected along a given direction. This consideration is of importance when comparing eq. (4-3) or (4-4) with the mean square displacement in three dimensions, as one might obtain, for example, by following individual atomic positions along a trajectory of a Molecular Dynamics simulation.

Within the limits of classical theory and harmonic approximation, the displacement of an atom can be represented by a sum of contributions from vibration waves (sum over normal modes), written as (Dove M. 2003) (Willis B. T. M. 1975) (Warren, X-Ray Diffraction 1990):

$$\underline{u_i} = \sum_{k=1}^{N} \sum_{\lambda=1}^{3} a_{k\lambda} \hat{e}_{k\lambda} \cos\left(\omega_{k\lambda} t - \underline{k} \cdot \underline{r_j} - \delta_{k\lambda}\right) = \\ = \sum_{k,\lambda} a_{k\lambda} \hat{e}_{k\lambda} \cos\left(\omega_{k\lambda} t - \underline{k} \cdot \underline{r_j} - \delta_{k\lambda}\right), \tag{4-5}$$

where $a_{k\lambda}$ is the wave amplitude and $\hat{e}_{k\lambda}$ the versor of vibration mode *k* (running from 1 to the number of atoms, *N*), polarization λ (for the three spatial directions), and circular frequency $\omega_{k\lambda}$.

Last term in the cosine argument, $\delta_{k\lambda}$, accounts for the lack of phase relations among thermal vibrations, which keep starting and stopping randomly in time, changing amplitude sign and direction. Eq.(4-5) can be used in eq. (4-2) to calculate the $MSRD_{\parallel}$ as:

$$\overline{\sigma_{ij}^2} = \overline{\left[\hat{r}_{ij}\cdot\left(\underline{u}_i - \underline{u}_j\right)\right]^2} \qquad (4\text{-}6)$$
$$= \overline{\left\{\sum_{k,\lambda}\left(\hat{r}_{ij}\cdot\hat{e}_{k\lambda}\right) a_{k\lambda}\, cos\left(\omega_{k\lambda}t - \underline{k}\cdot\underline{r}_i - \delta_{k\lambda}\right)\right.}$$
$$\left. - \sum_{k',\lambda'}\left(\hat{r}_{ij}\cdot\hat{e}_{k'\lambda'}\right) a_{k'\lambda'}\, cos\left(\omega_{k'\lambda'}t - \underline{k}'\cdot\underline{r}_j - \delta_{k'\lambda'}\right)\right\}^2.$$

Eq.(4-6) involves independent waves (kλ and k'λ'), so that the average of cross product, $\overline{cos\left(\omega_{k\lambda}t - \underline{k}\cdot\underline{r}_i - \delta_{k\lambda}\right) cos\left(\omega_{k'\lambda'}t - \underline{k}'\cdot\underline{r}_j - \delta_{k'\lambda'}\right)}$, is zero. Moreover, the average of products $\overline{a_{k\lambda}^2\left[cos(\ldots_i) - cos\left(\ldots_j\right)\right]^2}$ can be written as a product of averages; this is justified by the random nature of thermal vibrations, such that the average amplitude (changing sign randomly in time) is null, whereas, of course, $\overline{a_{k\lambda}^2}$ is not. Then eq.(4-6) reads:

$$\overline{\sigma_{ij}^2} = \sum_{k,\lambda}\left(\hat{r}_{ij}\cdot\hat{e}_{k\lambda}\right)^2 \overline{a_{k\lambda}^2} \qquad (4\text{-}7)$$
$$\cdot\, \overline{\left[cos\left(\omega_{k\lambda}t - \underline{k}\cdot\underline{r}_i - \delta_{k\lambda}\right) - cos\left(\omega_{k\lambda}t - \underline{k}\cdot\underline{r}_j - \delta_{k\lambda}\right)\right]^2}.$$

By standard trigonometric transformation the previous expression can be recast as:

$$\overline{\sigma_{ij}^2} = \sum_{k,\lambda}\left(\hat{r}_{ij}\cdot\hat{e}_{k\lambda}\right)^2 \overline{a_{k\lambda}^2}\left\{1 - \overline{cos\left[\underline{k}\cdot\left(\underline{r}_i - \underline{r}_j\right)\right]}\right. \qquad (4\text{-}8)$$
$$\left. - \overline{cos\left[2\omega_{k\lambda}t - 2\underline{k}\cdot\left(\underline{r}_i + \underline{r}_j\right) - 2\delta_{k\lambda}\right]}\right\}$$
$$= \sum_{k,\lambda}\left(\hat{r}_{ij}\cdot\hat{e}_{k\lambda}\right)^2 \overline{a_{k\lambda}^2}\left\{1 - cos\left[\underline{k}\cdot\left(\underline{r}_i - \underline{r}_j\right)\right]\right\},$$

where in the last equality it is recognized that the time average of the second cosine is zero. For harmonic oscillators the mean square amplitude can be related to the energy distribution. The kinetic energy of the crystal is:

$$E_K = \sum_i \frac{1}{2} m\dot{u}_i^2 = \sum_i \frac{1}{2} m \left[-\sum_{k,\lambda} a_{k\lambda}\omega_{k\lambda} \sin\left(\omega_{k\lambda} t - \underline{k}\cdot\underline{r_i} - \delta_{k\lambda}\right)\right]^2. \quad (4\text{-}9)$$

Then the average kinetic energy reads:

$$\overline{E_K} = \sum_i \frac{1}{2} m\overline{\dot{u}_i^2} = \sum_{k,\lambda} \frac{1}{4} Nm\omega_{k\lambda}^2 \overline{a_{k\lambda}^2}, \quad (4\text{-}10)$$

The mean kinetic energy of harmonic oscillators is equal to the mean potential energy, so the mean total energy, $\overline{E_T}$, can be written simply as twice the mean kinetic energy:

$$\overline{E_T} = \sum_{k,\lambda} \overline{E_{k\lambda}} = \sum_{k,\lambda} \frac{1}{2} Nm\omega_{k\lambda}^2 \overline{a_{k\lambda}^2}. \quad (4\text{-}11)$$

Based on eqs.(4-10) and (4-11), the mean square amplitude can be written as:

$$\overline{a_{k\lambda}^2} = \frac{2\overline{E_{k\lambda}}}{Nm\omega_{k\lambda}^2} = \frac{2}{Nm\omega_{k\lambda}^2} \hbar\omega_{k\lambda} \left(\frac{1}{e^{\frac{\hbar\omega_{k\lambda}}{k_B T}} - 1} + \frac{1}{2} \right) = \frac{2\hbar}{Nm\omega_{k\lambda}} \left[n(\omega_{k\lambda}) + \frac{1}{2} \right], \quad (4\text{-}12)$$

where the average energy of a harmonic oscillator, $\overline{E_{k\lambda}}$, is written according to the Bose-Einstein distribution, with phonon number $n(\omega_{k\lambda})$. (Dove M. 2003) Eq.(4-10) then takes the form:[1]

$$\overline{\sigma_{ij}^2} = \frac{2\hbar}{Nm} \sum_{k,\lambda} \frac{\left(\hat{r}_{ij}\cdot\hat{e}_{k\lambda}\right)^2}{\omega_{k\lambda}(\underline{k})} \left[n\left(\omega_{k\lambda}(\underline{k})\right) + \frac{1}{2} \right] \left[1 - cos\left(\underline{k}\cdot\underline{r_{ij}}\right)\right], \quad (4\text{-}13)$$

[1] An equivalent expression can be obtained by assigning atom *j* phase $e^0 = 1$, and atom *i* phase $e^{i\underline{k}\cdot\underline{r}_{ij}}$; this leads to the same result as in eq.(8) and (13), given that $\frac{1}{2}\left|e^{i\underline{k}\cdot\underline{r}_{ij}} - 1\right|^2 = 1 - cos\left(\underline{k}\cdot\underline{r_{ij}}\right)$

where the dependence of $\omega_{k\lambda}$ on $\underline{k}$, i.e., the phonon dispersion relation, is specifically reported.

This expression can be simplified under the assumptions of Debye's model. This leads to the CD model originally developed by Beni & Platzman for applications to EXAFS data analysis. As already pointed out, the CD model provides for a simple, although approximated, representation of $MSRD_{\parallel}$ as a function of the distance from a central atom (according to definitions in EXAFS theory and radial distribution function), which is also the distance of the different coordination shells. As shown below, despites all approximations, and even if based on the refinement of just a single parameter (the Debye temperature, Θ_D), the CD model correctly captures the progressive loss of correlation of atomic vibrations for increasing distance between atoms.

The traditional Debye model relies on the assumption of Figure 4-2, according to which the phonon density of states (aka Vibrational Density of States (VDOS), g(v), or g(ω) for circular frequency) is replaced by a parabolic approximation, which elegantly captures the detail of the acoustic (low frequency) component.

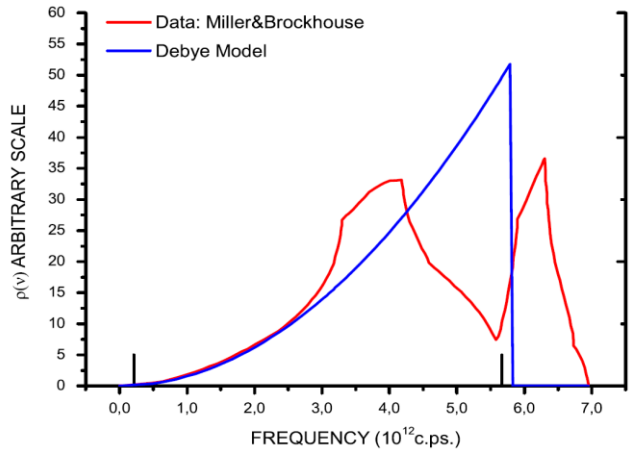

Figure 4-2

Vibrational Density of States (VDOS), ρ(ν), for Palladium and corresponding Debye model. The two ticks mark, respectively, low (ν_s) and high (ν_L) cut-off frequencies for a truncated-edge cube of Pd with 10715 atoms (eqs.(29)-(32), see text for details).

This feature of Debye's approximation is relevant, as the CD model fundamentally relies on the acoustic phonon spectrum, under the harmonic hypothesis. According to the traditional Debye's model we make no distinction between longitudinal and transversal vibration modes. We further assume a

linear relation for the phonon dispersion of acoustic waves (valid in the limit for k→0 (Dove M. 2003)), which is then just a scalar relation:

$$\omega_{k\lambda}(\underline{k}) = \omega(k) = c\,k, \tag{4-14}$$

where *c* is the average velocity of sound. As shown by Willis & Pryor, this simple linear approximation can be replaced by a sine law, which is exact for the case of monoatomic crystals. In the following we adopt eq.(4-14) as it is computationally simpler and appropriate to the level of approximation of the theory.[2] Results can easily be extended to other dispersion relations.

The first Brillouin Zone (BZ), of volume $\frac{(2\pi)^3}{V}$,[3] is replaced by a sphere containing the same number of points (3N, for as many wavevectors), so that the radius of the spherical volume is:

$$k_D = \left(\frac{6\pi^2 N}{V}\right)^{\frac{1}{3}}. \tag{4-15}$$

The sum over *k* in eq.(4-13), can then be replaced by an integral over the first BZ,

$$\overline{\sigma_{ij}^2} = \frac{2\hbar}{Nm}\frac{V}{(2\pi)^3}\int_{BZ}\sum_{\lambda}\left(\hat{r}_{ij}\cdot\hat{e}_{k\lambda}\right)^2\frac{1}{ck}\left[n(k)+\frac{1}{2}\right]\left[1 - cos\left(\underline{k}\cdot\underline{r}_{ij}\right)\right]d\underline{k}. \tag{4-16}$$

Eq. (4-15) can be used to introduce k_D by substituting for $\frac{V}{N(2\pi)^3}$; then, performing the integration in spherical coordinates:

[2] The correct dispersion relation for a monoatomic crystal reads: $\omega_{k\lambda}(\underline{k}) = c\left(\frac{2k_D}{\pi}\right)sin\left(\frac{\pi k}{2k_D}\right)$

[3] V is the volume of the *primitive* unit cell. For *fcc* Pd, V is ¼ of the volume of the conventional unit cell with unit cell parameter a_0=3.8907 Å

$$\overline{\sigma_{ij}^2} = \frac{6\hbar}{2\pi m k_D^3}\int_0^{2\pi}\int_0^{\pi}\int_0^{k_D}\frac{1}{ck}\left[n(k)+\frac{1}{2}\right]\left[1 - cos\left(kr_{ij}\,sin\,\theta\right)\right]k^2 dk\,sin\,\theta\,d\theta\,d\phi$$
$$= \frac{6\hbar}{mk_D^3}\int_0^{k_D}\frac{k}{c}\left[n(k)+\frac{1}{2}\right]\left[1-\frac{sin\left(kr_{ij}\right)}{kr_{ij}}\right]dk, \qquad (4\text{-}17)$$

where we used the closure-completeness relations [11,22], $\sum_\lambda\left(\hat{r}_{ij}\cdot\hat{e}_{k\lambda}\right)^2 = 1$. Integration of eq.(4-17) is straightforward, and can also be performed in terms of circular frequency as integration variable; as shown by Sevigliano *et al*. [24], according to eq.(4-14):

$$\overline{\sigma_{ij}^2} = \frac{6\hbar}{m\omega_D^3}\int_0^{\omega_D}\omega\left(\frac{1}{e^{\frac{\hbar\omega}{k_BT}}-1}+\frac{1}{2}\right)\left[1-\frac{sin\left(\frac{\omega r_{ij}}{c}\right)}{\frac{\omega r_{ij}}{c}}\right]d\omega =$$
$$= \frac{2\hbar}{3Nm}\int_0^{\omega_D}\frac{\rho(\omega)}{\omega}\left(\frac{1}{e^{\frac{\hbar\omega}{k_BT}}-1}+\frac{1}{2}\right)\left[-\frac{sin\left(\frac{\omega r_{ij}}{c}\right)}{\frac{\omega r_{ij}}{c}}\right]d\omega. \qquad (4\text{-}18)$$

In the last expression (eq.(4-18)) we have introduced the Debye distribution, shown in Figure 4-2 for Pd, defined as:

$$\rho(\omega)d\omega = \frac{9N\omega^2}{\omega_D^3}d\omega \qquad (4\text{-}19)$$

Integration gives:

$$\overline{\sigma_{ij}^2} = \frac{6\hbar}{m\omega_D^3}\left\{\frac{\omega_D^2}{4}+\int_0^{\omega_D}\frac{\omega d\omega}{e^{\frac{\hbar\omega}{k_BT}}-1}+\frac{c^2}{2r_{ij}^2}\left[cos\left(\frac{\omega_D r_{ij}}{c}\right)-1\right]\right.$$
$$\left.-\frac{1}{\frac{\omega_D^2 r_{ij}}{c}}\int_0^{\omega_D}\frac{sin\left(\frac{\omega r_{ij}}{c}\right)d\omega}{e^{\frac{\hbar\omega}{k_BT}}-1}\right\}. \qquad (4\text{-}20)$$

It is now convenient to introduce the Debye temperature, Θ_D, defined as:

$$\hbar\omega_D = k_B\Theta_D(=\hbar ck_D) \qquad (4\text{-}21)$$

where the last equality is valid according to the phonon dispersion of acoustic waves (eq.(4-14)). Eq.(20) can then be written in terms of T, $\hbar\omega/k_B$ and Θ_D by a change of variable ($x = \left(\frac{\omega}{\omega_D}\right)\left(\frac{\Theta_D}{T}\right)$):

$$\overline{\sigma_{ij}^2} = \frac{6\hbar^2}{mk_B\Theta_D} \cdot \left\{ \left[\frac{1}{4} + \left(\frac{T}{\Theta_D}\right)^2 \int_0^{\frac{\Theta_D}{T}} \frac{x\,dx}{e^x - 1} \right] + \frac{cos\left(\frac{k_B\Theta_D r_{ij}}{\hbar c}\right) - 1}{2\left(\frac{k_B\Theta_D r_{ij}}{\hbar c}\right)^2} - \left(\frac{T}{\Theta_D}\right)^2 \int_0^{\frac{\Theta_D}{T}} \frac{sin\left(\frac{k_B x r_{ij} T}{\hbar c}\right)}{\left(\frac{k_B r_{ij} T}{\hbar c}\right)} \frac{dx}{e^x - 1} \right\} \quad (4\text{-}22)$$

Integrals in eq.(4-22) can be calculated numerically, e.g., by series expansion, unless specific functions are available in the computer libraries.

4.3 Correlated Debye model in finite crystalline domains

The expressions derived so far implicitly refer to crystals of large dimension: the VDOS in Figure 4-2, for example, was measured on a single crystal of Pd, specifically grown for neutron scattering measurements in the shape of a boule, 3" long by ca 0.75" diameter (Miller A.P. 1971).

Nanocrystals are quite different, and their finiteness makes phonon confinement (max allowed vibration wavelength) and surface vibration modes important. The VDOS of a finite body must account for the additional modes arising from surfaces – in terms of limiting planes, edges and even corner points – and include the appropriate wavelength cut-off for the size and shape of the domain. In turn this influences the way the DW coefficient should be calculated. After the early studies of Bolt, Maa and Roe around 1940 (Bolt 1939) (Maa 1939) (Roe 1941) much of the theory has been reviewed by Schoening (Schoening 1968) and by Urban (Urban 1975) : the following results rely directly on the cited literature.

Since the original studies of Bolt, Maa and Roe it was clear that the finite size of the studied volume reflects into an upper bound of phonon wavelength. A typical example is plane standing waves between two opposite walls, where the wavelength cannot exceed twice the distance between the walls, L:

$$\lambda_{max} = 2L \tag{4-23}$$

This upper limit corresponds to a low-frequency limit, $2\pi\nu_{min} = \omega_{min} = \frac{2\pi c}{\lambda_{max}} = \pi c\,/L$ (using the dispersion relation of eq. (4-14) for acoustic waves), to enforce in the VDOS calculation and in the Debye approximation of Figure 4-2. It is worth underlying that low-frequency /long-wavelength phonons have the largest influence on X-ray scattering, so we can expect visible effects of the λ_{max} threshold in XRD patterns (Warren, X-Ray Diffraction 1990). Proper consideration must also be given to the way the BZ is replaced by a corresponding spherical volume in Reciprocal Space, including 3N vibration modes (points). For finite crystalline domains one has to account for the surface modes in addition to the volume modes. Edges and corner points, if present in the domain shape, also contribute additional modes, but the importance of the latter terms, however, decreases for decreasing dimensionality (in the order: surface, line, point). As a consequence, surface terms only are retained in most calculations of practical use.

The VDOS in the Debye model, according to Schoening (Schoening 1968), can be rewritten as:

$$\rho(\nu)d\nu = \left(\frac{4\pi V\nu^2}{c_3} + \frac{\pi S\nu}{2c_2} + \frac{L}{8c_1}\right)d\nu \tag{4-24}$$

The expression above refers to a cubic crystal so one could write $S = 6L^2$ and $V = L^3$, to express the equation as function of one common variable (cube edge, L). Neglecting the linear term:

$$\rho(\nu)d\nu \cong \left(\frac{4\pi V\nu^2}{c_3} + \frac{\pi S\nu}{2c_2}\right)d\nu = L^2\left(\frac{4\pi L\nu^2}{c_3} + \frac{3\pi\nu}{c_2}\right)d\nu \tag{4-25}$$

where c_i define different average wave velocities (*l*, *t* and *m* stand for *longitudinal*, *transversal* and *mean* respectively):

$$c_3^{-1} = c_l^{-3} + 2c_t^{-3} = 3c_m^{-3}, \qquad (4\text{-}26)$$

$$c_2^{-1} = c_l^{-2} + 2c_t^{-2} = 3\gamma c_m^{-2},$$

and

$$\gamma = \frac{1}{3}\left(1 + \frac{2c_l^2}{c_t^2}\right)\left[\frac{3}{\left(1 + \frac{2c_l^3}{c_t^3}\right)}\right]^{\frac{2}{3}}. \qquad (4\text{-}27)$$

Values of γ are around unity for most metals: details are given in the Appendix. The VDOS in eq.(4-25) can be normalized to get the upper bound frequency by solving (Huang W.J. 2008):

$$\int_{\nu_s}^{\nu_L} \rho(\nu)d\nu \cong \int_{\nu_s}^{\nu_L} \left(\frac{4\pi V \nu^2}{c_3} + \frac{\pi S \nu}{2c_2}\right) d\nu = 3N, \qquad (4\text{-}28)$$

where the lower bound is given by eq.(4-23), generalized as:

$$\nu_s = \frac{1}{2}\frac{c_m}{V^{1/3}}. \qquad (4\text{-}29)$$

Eq.(4-29) refers to a cube with clamped surfaces, from the previously cited case of standing sound waves between parallel walls. As pointed out by Schoening, this lower cut-off frequency could be different for free surfaces and for different domain shapes, not to mention the fact that a constant velocity for all modes is of course a rather coarse simplification. This is one of the most drastic simplifications of the CD model, so that the linear dispersion of eq.(4-14) appears also justified to the overall level of approximation. Eq.(4-28) can be solved to give ν_L,

$$\nu_L \cong c_m \left(\frac{3N}{4\pi V}\right)^{\frac{1}{3}}\left[1 - \frac{\gamma\pi}{2\sqrt[3]{N}}\left(\frac{3}{4\pi}\right)^{\frac{2}{3}}\right]. \qquad (4\text{-}30)$$

In the integration of eq., besides neglecting the last term of the VDOS of eq.(4-24), the lower limit of integration was set to zero, and terms of the order of $N^{-\frac{2}{3}}$ and smaller were neglected [28].
Results of eq.(4-29)and (4-30) can be expressed in terms of equivalent temperatures, so that:

$$\Theta_s = \frac{h\nu_s}{k_B} = \Theta_D \left(\frac{4\pi}{3}\right)^{\frac{1}{3}} \frac{1}{2\sqrt[3]{N}}, \tag{4-31}$$

$$\Theta_L = \frac{h\nu_L}{k_B} = \Theta_D \left(1 - \frac{\gamma b}{2\sqrt[3]{N}}\right), \tag{4-32}$$

where $b = \pi \left(\frac{3}{4\pi}\right)^{\frac{2}{3}}$. The Debye temperature is then equivalent to Θ_L in the limit for large crystals, i.e., for $N \to \infty$:

$$\lim_{N\to\infty} \Theta_L = \lim_{N\to\infty} \Theta_D \left(1 - \frac{\gamma b}{2\sqrt[3]{N}}\right) = \Theta_D = \frac{\hbar c k_D}{k_B}. \tag{4-33}$$

As an example, low (ν_s) and high (ν_L) cut-off frequencies are shown in Figure 4-2, for a nanocube of Pd with truncated edges and corners (10715 atoms, approximately 5 nm edge; more details are reported in the next section).
In the following expressions it is convenient to introduce:[4]

$$A_1 = \frac{6\hbar^2}{m k_B \Theta_D} \left(1 - \frac{\gamma b}{2\sqrt[3]{N}}\right)^2, \tag{4-34}$$

$$A_2 = \frac{6\hbar^2 \gamma b}{m k_B \Theta_D \sqrt[3]{N}} \left(1 - \frac{\gamma b}{2\sqrt[3]{N}}\right), \tag{4-35}$$

[4] In calculations: m is given by the molar weight divided by Avogadro's number (e.g., 106.42x10-3 /6.022x1023 for Pd); h = 6.26606896x10-34 ($\hbar = \frac{h}{2\pi}$) and kB = 1.3806504x10-23; if lengths are given in Å units then A_1 and A_2 should be multiplied by a factor of 1020.

Eq.(4-18) for $\overline{\sigma_{ij}^2}$, can now be extended to the case of a finite crystal as:

$$\overline{\sigma_{ij}^2} = \frac{2\hbar}{3Nm}\int_{\omega_s}^{\omega_L}\frac{\rho(\omega)}{\omega}\left(\frac{1}{e^{\frac{\hbar\omega}{k_BT}}-1}+\frac{1}{2}\right)\left[1-\frac{sin\left(\frac{\omega r_{ij}}{c}\right)}{\frac{\omega r_{ij}}{c}}\right]d\omega, \tag{4-36}$$

which worked out gives:

$$\begin{aligned}\sigma_{ij}^2 = A_1\Bigg\{&\frac{1}{4}\left[1-\left(\frac{\Theta_s}{\Theta_D}\right)^2\right]+\left(\frac{T}{\Theta_L}\right)^2\int_{\frac{\Theta_s}{T}}^{\frac{\Theta_L}{T}}\frac{xdx}{e^x-1}\\ &+\frac{cos\left(\frac{rk_B\Theta_L}{\hbar c_m}\right)-cos\left(\frac{rk_B\Theta_s}{\hbar c_m}\right)}{2\left(\frac{rk_B\Theta_L}{\hbar c_m}\right)^2}\\ &-\left(\frac{T}{\Theta_L}\right)^2\Psi_1(r,T,\Theta_L,\Theta_s)\Bigg\}+A_2\Bigg[\frac{1}{2}\left(1-\frac{\Theta_s}{\Theta_L}\right)+\frac{T}{\Theta_L}ln\left(\frac{1-e^{-\frac{\Theta_L}{T}}}{1-e^{-\frac{\Theta_s}{T}}}\right)\\ &+\frac{\hbar c_m}{2rk_B\Theta_L}\left(\int_0^{\frac{rk_B\Theta_s}{\hbar c_m}}\frac{sin\,x\;dx}{x}-\int_0^{\frac{rk_B\Theta_L}{\hbar c_m}}\frac{sin\,x\;dx}{x}\right)\\ &-\frac{T}{\Theta_L}\Psi_0(r,T,\Theta_L,\Theta_s)\Bigg].\end{aligned} \tag{4-37}$$

With

$$\Psi_1(r,T,\Theta_L,\Theta_s) = \int_{\frac{\Theta_s}{T}}^{\frac{\Theta_L}{T}}\frac{sin\left(\frac{rk_BTx}{\hbar c_m}\right)}{\left(\frac{rk_BTx}{\hbar c_m}\right)}\frac{xdx}{e^x-1}, \tag{4-38}$$

$$\Psi_0(r,T,\Theta_L,\Theta_s) = \int_{\frac{\Theta_s}{T}}^{\frac{\Theta_L}{T}}\frac{sin\left(\frac{rk_BTx}{\hbar c_m}\right)}{\left(r\frac{k_BTx}{\hbar c_m}\right)}\frac{dx}{e^x-1}. \tag{4-39}$$

As with eq.(4-18), (4-20), (4-22), integrals in eq.(4-37)-(4-39) can be solved numerically or by series expansion of the argument.

4.4 Testing the Correlated Debye model

Application of the CD model to nanocrystalline systems requires proper consideration of additional effects caused by the finiteness of crystalline domains. For one, surface tension forces invariably affect nanoparticles, with increasingly more significant effects the smaller the crystalline domains. More generally we can consider the effects of surface relaxation, responsible for changes of atomic distances, and sometimes even arrangement of surface atomic bonds which can differ from those of the ideal (perfect crystal) bulk structure. Surface relaxation effects extend beyond the surface region, inside the nanoparticle. Most often the first order effect stems from the different (usually lower) coordination causing atomic displacement, which decays more or less slowly toward the interior of the crystalline region (K. B. Gelisio L. 2013)

Nanoparticles can be studied with MD. The initial nanoparticle was carved out of a large volume of *fcc* Pd perfect lattice. After activating the potential, the simulation started with the particle, assumed at T=0K, treated as an NVT canonical ensemble (constant number of atoms, N, system volume, V, and temperature T). Employing Langevin dynamics, the system was thermalized with a chain of Nosé-Hoover thermostats, until reaching equilibrium at T=300K. The system was then considered an NVE ensemble (lifting the constraint on T, i.e. by removing the thermostat) and left isolated for a total time of 2.5 nanoseconds, with simulation timestep of 1 fs, so that the whole thermalization process took 2.500.000 steps.

After all this procedure, 500 frames were sampled along 0.5 ns of simulation. Each frame contains coordinates of all atoms, dumped every 1000 steps along the MD simulations. The series of frames constitute the MD trajectory of the system.

Simple models have been proposed to describe this displacement field. For example, according to Pauling's idea (Pauling 1947), displacement can be calculated from the coordination number, lower on the surface than in the

bulk. Further details can be added to Pauling's model by considering elastic anisotropy (Perez Demydenko C. 2017).

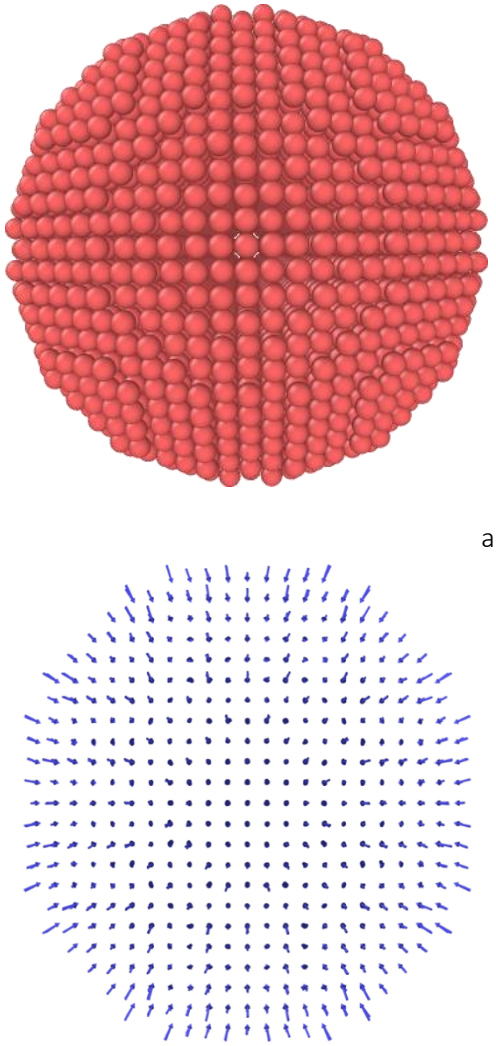

Figure 4-3

Displacement field in a Pd (quasi)spherical nanoparticle (a); [h00],[0k0] cross-section; arrows are drawn according to a MD simulation, portraying the displacement of each atom from the starting position of the perfect face centred cubic (fcc) lattice (see text for details) (b).

In most metals, and Pd among them (Figure 4-3), the main effect of finiteness is a contraction of the nanoparticle, an effect sometimes interpreted in terms of specific surface energy and Young-Laplace equation. This contraction is far from being uniform across the crystalline domain. This is made quite evident in Figure 4-3 by the varying length of the arrows representing the modulus of the displacement; displacement direction is mainly radial, but this specific feature

(displacement direction) changes with the nanoparticle shape (see (a. L. Scardi P. 2016), and references therein). The point of interest here is that the surface relaxation does not contribute just a uniform contraction: average atomic distances are reduced, but the displacement field is inhomogeneous, thus introducing a static contribution to the atomic displacement disorder, in addition to a rescaling of average atomic distances. This contribution, within the limits of a good approximation, can be assumed as independent of the dynamic effect of temperature, so that static and dynamic effects refer to independent displacement distributions. As a reasonable assumption (exact for Gaussian distributions) we can write (Guinier 1963) (Humphrey W. A. Dalke 1996):

$$\overline{\sigma_{ij}^2} = \overline{\sigma_{ij}^2}_0 + \overline{\sigma_{ij}^2}_T \qquad (4\text{-}40)$$

where $\overline{\sigma_{ij}^2}_T$, according to the CD model, is given by eq.(4-37), whereas $\overline{\sigma_{ij}^2}_0$ is a temperature-independent term. Generally, both terms are function of the size of the crystalline domain, its shape, and elastic properties. This is represented, although in a simplified manner, by the CD model for the thermal component, while no general theory is available for the static component (Born M 1954).

Insights on the extension and relevance of the effects contributing to eq.(4-40) can be obtained from the Radial Pair Distribution Function (RPDF), readily available from MD simulations. Figure 4-4 (a) shows the RPDF for a simulated system where atomic coordinates of each atom were averaged over (500) different time steps in the stationary portion of the MD trajectory (equilibrated and thermalized NVE system). In this way the dynamic (thermal) disorder is averaged out and static disorder only is left. Broadening of the RPDF peaks – which in an ideal, perfect crystal would be Dirac's delta functions – is caused by the inhomogeneous nature of the static disorder contributed by surface relaxation; in fact, a *homogeneous* displacement would just shift the Dirac's delta functions. The test system of Figure 4-4 is a pseudo-cubic domain (a cube with truncated edges and corners) of 10715 Pd atoms, with a nominal edge length of 5 nm. The distribution variance can be taken as a measure of $\overline{\sigma_{ij}^2}_0$.

The RPDF of the same system was calculated after MD simulation at 300K, by taking the average of 500 RDPFs over as many snapshots along the steady state

trajectory (same snapshots used before, to calculate average coordinates and the corresponding RPDF of Figure 4-4 (a)). This average RPDF mimics what would be observed in a real experiment, i.e., it includes both static and dynamic terms of eq.(4-40). As shown in Figure 4-4 (b), peaks for the different coordination shells can be modelled reasonably well by Gaussian curves, thus providing estimates of $\overline{\sigma_{ij}^2}$. In particular, peak widths from top and bottom plots give, respectively, $\overline{\sigma_{ij}^2}_0$, and the overall contribution, $\overline{\sigma_{ij}^2}_0 + \overline{\sigma_{ij}^2}_T$.

Based on the RPDF and fitting results like those of Figure 4-5, the CD model of eq.(4-37) can be tested by adding a term representing the static disorder as in eq.(4-40). The latter is much smaller than the thermal contribution at 300K, so that a constant $\overline{\sigma_{ij}^2}_0$ term may be appropriate as a first-order approximation; eventually this basic model could be improved, when testing more extended ranges of distances, by assuming a slowly varying function of *r* for the static component to match the sloping trend of $\overline{\sigma_{ij}^2}_0$, in Figure 4-5.

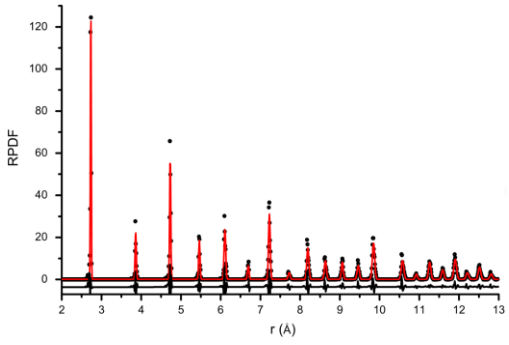

a)

Figure 4-4

RPDF after MD simulation of a truncated edge-corner cube of ca 5 nm edge length, 10715 Pd atoms (bottom right). RPDF from time-averaged atomic coordinates (a) in a stationary MD trajectory at 300K; for the same system, RPDFs were calculated at several spaced time-steps in the same stationary MD trajectory, and then averaged (b), thus simulating a real system, i.e., including both static and dynamic disorder effects. Red line in both plots refers to the fit using Gaussian line profiles. RPDF curves were obtained using VMD (Humphrey W. A. Dalke 1996)

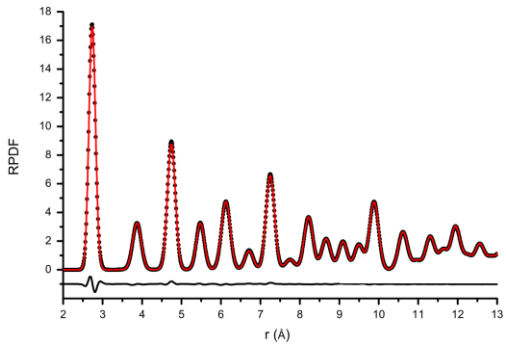

b)

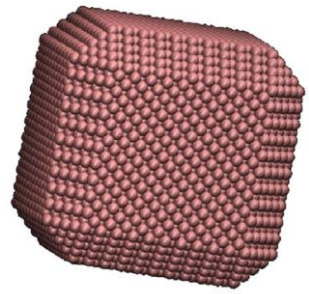

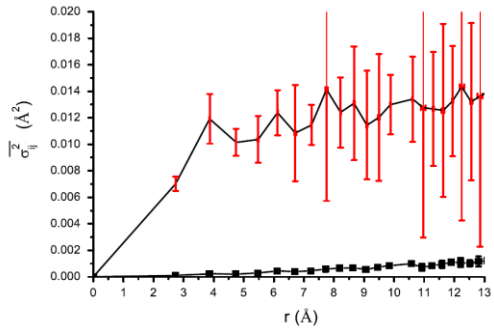

Figure 4-5

Trends of $\overline{\sigma_{ij}^2} = \overline{\sigma_{ij}^2}_0 + \overline{\sigma_{ij}^2}_T$ *(red circle) and* $\overline{\sigma_{ij}^2}_0$ *(black square) as a function of the shell distance, r. Data from the best fit of Gaussian curves to the RPDF peaks in Figure 4-4, calculated for a truncated edge-corner cube of ca 5 nm edge length, 10715 Pd atoms. Lines are drawn just to drive the eye. Large error bars result from the Gaussian modelling of the RPDF peaks, which is affected by peak overlapping, increasingly more severe for growing shell distances*

The reference value of Debye temperature for a bulk crystal - i.e., a crystal with no static disorder and no finite domain effect on the thermal disorder - is Θ_D=272K from literature (Veisz B. 2002). However, when testing the CD model on MD data the Debye temperature should be adjusted to the specific EAM potential used, and a similar need arises in experimental studies. That means refining values of Θ_D and $\overline{\sigma_{ij}^2}_0$, a task more reliably performed on a set of simulations rather than on a single one. For this reason the truncated cube of Figure 4-4 and Figure 4-5 was scaled, i.e., size was changed while keeping the same shape, to nominal sizes (with number of atoms in parenthesis) of: 3 nm (4244), 4 nm (7468), 10 nm (64695), 15 nm (197587) and 20 nm (505373), in addition to the 5 nm (10715) already discussed.

Data like those of Figure 4-4 and Figure 4-5 were obtained for each cube size and the trends modelled by the CD model for the corresponding crystal sizes, according to the conditions on $\sqrt{N}$ in eqs.(4-30)-(4-35). Best values of Θ_D and $\overline{\sigma_{ij}^2}_0$ were obtained by a non-linear least squares fitting of all trends. Convergence is straightforward and gives Θ_D=262K, not far from the experimental value of Butt *et al*. (Butt 1988).

The trend of $\left(\overline{\sigma_{ij}^2}\right)^{1/2}$ (RMSRD, Root Mean Square Relative Displacement), including both thermal and static contributions according to the models of eq.(4-37) and (4-40), is shown in Figure 4-6. The two simulations shown are those with largest differences, namely: smallest cube, 3 nm (4244 Pd atoms, orange cross for MD data, line for CD model), and largest cube, 20 nm (505373 Pd atoms, blue cross for MD data, line for CD model). Figure 4-6 also shows the trend for a corresponding infinite-size Pd system . This was calculated according to eq.(4-22), assuming the Debye temperature as in the previous modelling, and no static component (black line). The experimental value from literature data on bulk Pd (see Appendix) is $\left(\overline{\sigma_{ij}^2}\right)^{1/2}$ =0.107 Å, shown in Figure 4-6 as a horizontal grey line, and agrees quite well with the asymptotic value of the CD model for the infinite-size Pd case.

As expected the trend of $\left(\overline{\sigma_{ij}^2}\right)^{1/2}$ vs *r* decreases with increasing nanoparticle size, tending to the asymptotic value for infinite systems. The contribution of static disorder, the intercept at $r = 0$, increases for smaller sizes. Asymptotic values of $\left(\overline{\sigma_{ij}^2}\right)^{1/2}$, the square root of eq.(40), calculated for the maximum length across the nanoparticle ([111] diagonal), are, respectively, 0.1201 Å (orange line) and 0.1136 Å (blue line). Trends are shown in Figure 4-7 for the six domain sizes considered in the simulations. In the limit for N→infinity, eq.(4-37) is equivalent to eq.(4-22), the expression of the traditional CD model for an infinite system. As shown in Figure 4-6, eq.(4-22) asymptotically matches the experimental RMSRD value, and as a consequence, the asymptotic RMSRD values for the thermal component (red circles in Figure 4-7) approach the experimental value for very large number of atoms, i.e., for bulk crystals.

So far $\overline{\sigma_{ij}^2}_0$ was assumed constant, independent of the atomic distance, which may appear as a crude approximation of the trend in Figure 4-5. To test the effect on this assumption on the validity of the proposed approach, Figure 4-8 shows the CD model of eq.(4-37) and (4-40) for the 5 nm truncated cube (red line) and MD results (black cross), compared with the trend obtained by replacing the constant $\overline{\sigma_{ij}^2}_0$ term with a linear function of *r* (green line). Differences are visible but acceptably small, because the main effect of a static component growing with the distance affects far distance coordination shells, which are not so relevant in the present context, where nearest-neighbours are mostly considered.

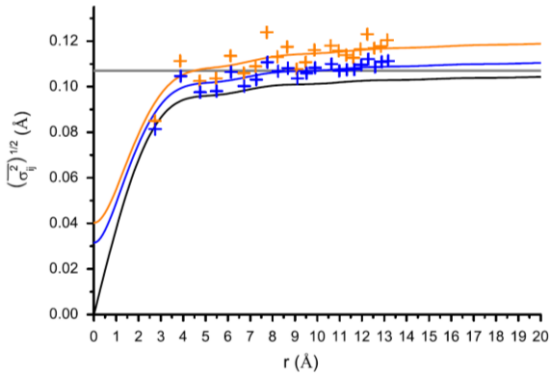

Figure 4-6

Results of CD model (eq.(4-37) and (4-40)) expressed as Root Mean Square Relative Displacement (RMSRD), $\left(\overline{\sigma_{ij}^2}\right)^{1/2}$, for truncated-edge-corner cubes: nominal size 3 nm (4244 Pd atoms, orange cross, CD model: orange line), and 20 nm (505373 Pd atoms, blue cross, CD model: blue line). Corresponding result for an infinite-size system (black) and experimental value for Pd (0.107 Å, grey line). See text for details.

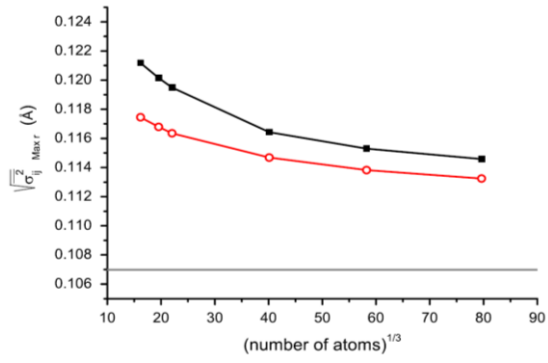

Figure 4-7

Trend of the asymptotic (largest r in crystal) value of root mean square relative displacement, $\left(\overline{\sigma_{ij}^2}\right)^{\frac{1}{2}}_{Max\ r}$, as a function of the cubic root of the number of atoms (proportional to a length parameter). CD model result with both terms in eq.(40) (black square) and with thermal component only (red circle). Horizontal line for the experimental value for bulk Pd.

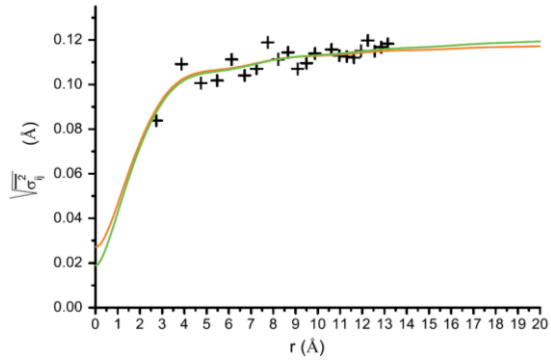

Figure 4-8

Comparison of CD models for the 5 nm truncated cube (black cross) using a constant (red line) or a linear function of r (green line) to model $\overline{\sigma_{ij}^2}_0$.

As a further application of the CD model, we can consider the "full" MSRD calculation (as detailed in paragraph 1.4.1) and the different components, static and dynamic. Three examples are shown in the figures: 6nm diameter sphere (Figure 4-9), 7nm diameter sphere (Figure 4-10), 9nm diameter sphere (Figure 4-11) and 20% truncated cube of 4nm edge (Figure 4-12).

The CD model (eq. (4-37)) can furthermore be used and compared to the results of paragraph 1.4.2, where an expression to single out the purely dynamical component of the MSRD was presented (eq. (1-29)). In this case the thermal component has been calculated directly for all coordination shells in the MD simulated particle and it is not extracted from the fitting of the RPDF.

This different and more complete approach will be extended in a simple model for the MSRD in chapter 5.

Figure 4-9, Figure 4-10, Figure 4-11 and Figure 4-12 show the various components of the MSRD. Best values of Θ_D have been obtained, and the CD model matches well the MD calculated thermal components up to the final part (large distances), where agreement is hindered by the erratic contribution of the surface. The Modified CD model takes indeed into consideration the finite size of the particle, but does not provide for the fine details of the surface that Molecular Dynamics on the contrary can account for.

In all figures (for example, Figure 4-9(b)) the result of adding the static component to the CD model is shown, together with the full MSRD calculated from MD simulations. The agreement of the two functions is good, demonstrating that (i) the Mean Square Radial Displacement inherits its trend from the static component that, in turn, (ii) it is strictly dependent on the shape of the nanoparticle (as also discussed in paragraph 1.4).

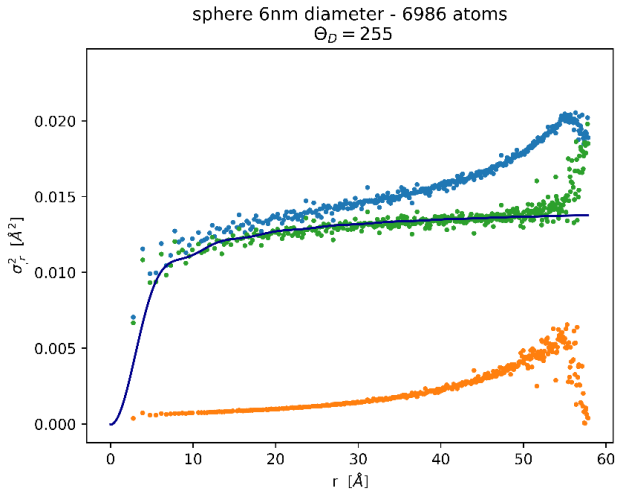

a)

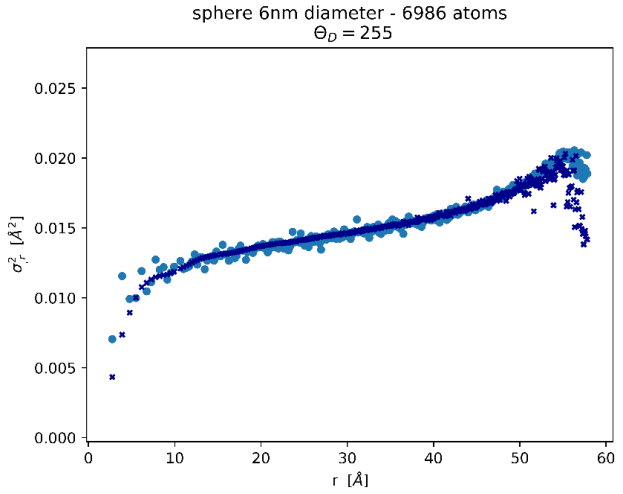

b)

Figure 4-9

MSRD in a sphere of 6nm diameter (6986 atoms).

a) Comparison between the dynamical component of the MSRD (green) and the modified Correlated Debye function (dark blue), calculated with eq. (4-37), with the best fit for $\Theta_D = 255K$.

b) Full MSRD calculated by adding the static component (orange in (a)) δ_{SR}^2 to the CD model (dark blue) and fully calculated MSRD (light blue)

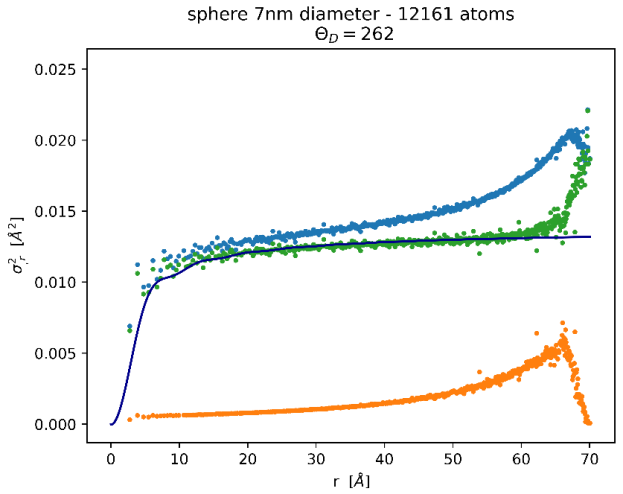

a)

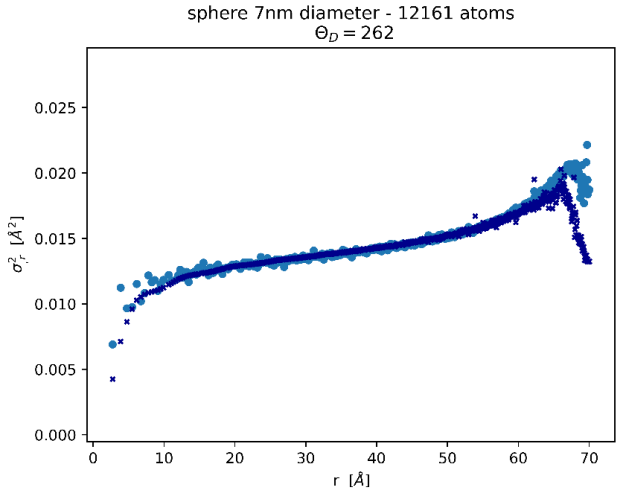

b)

Figure 4-10

MSRD in a sphere of 7nm diameter (12161 atoms).

a) *Comparison between the dynamical component of the MSRD (green) and the modified Correlated Debye function (dark blue), calculated with eq. (4-37), with the best fit for* $\Theta_D = 262K$.

b) *Full MSRD calculated by adding the static component (orange in (a)) δ_{SR}^2 to the CD model (dark blue) and fully calculated MSRD (light blue)*

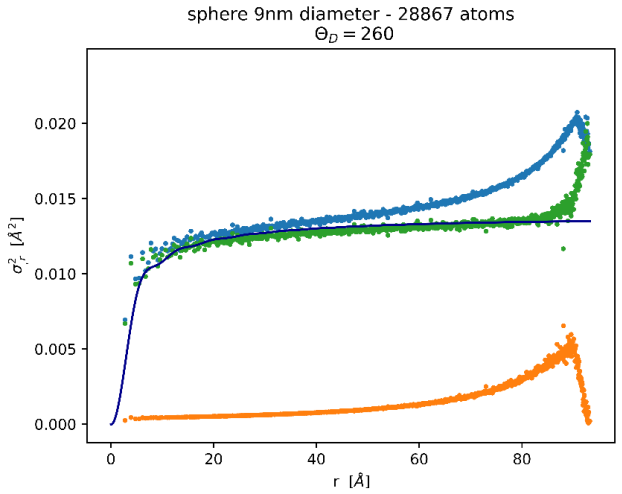

a)

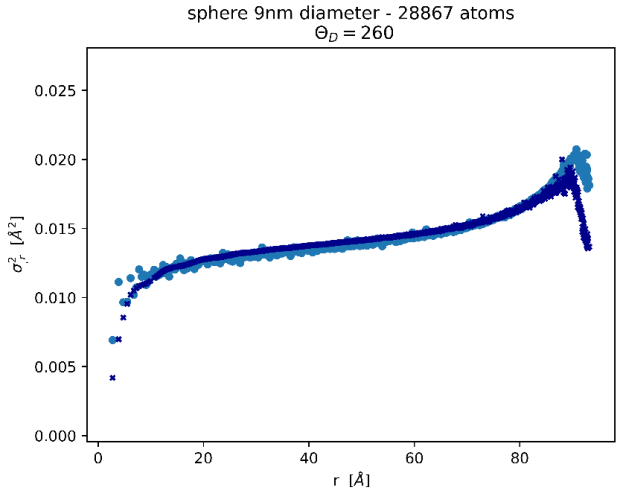

b)

Figure 4-11

MSRD in a sphere of 9nm diameter (28867 atoms).

c) *Comparison between the dynamical component of the MSRD (green) and the modified Correlated Debye function (dark blue), calculated with eq. (4-37), with the best fit for* $\Theta_D = 260K$.

d) *Full MSRD calculated by adding the static component (orange in (a)) δ_{SR}^2 to the CD model (dark blue) and fully calculated MSRD (light blue)*

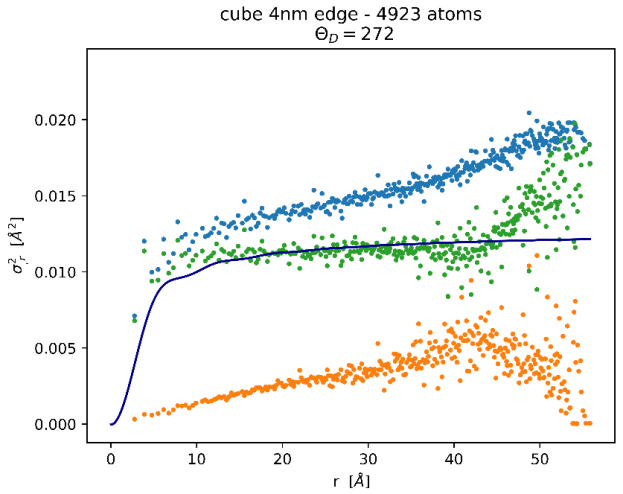

a)

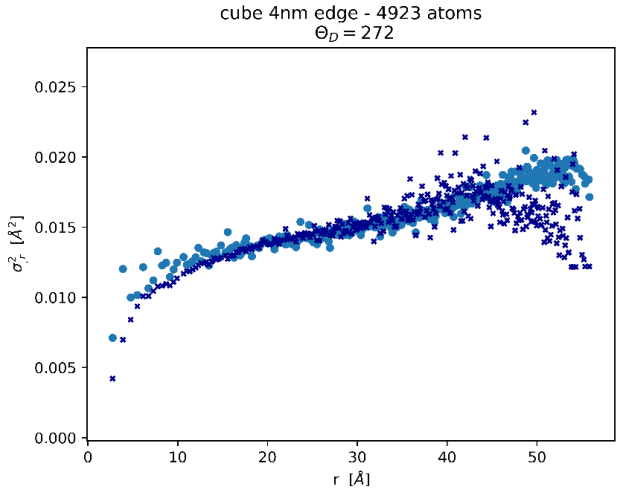

b)

Figure 4-12

MSRD in a 20% truncated cube of edge 4nm (4923 atoms).

a) Comparison between the dynamical component of the MSRD (green) and the modified Correlated Debye function (dark blue), calculated with eq. (4-37), with the best fit for $\Theta_D = 272K$.

b) Full MSRD calculated by adding the static component (orange in (a)) δ_{SR}^2 to the CD model (dark blue) and fully calculated MSRD (light blue)

4.5 EXPERIMENTAL

To test the new model with an experimental case study we considered recently published data on spherical Pt nanocrystals (Shi C. 2013). The study reports U_{ISO} coefficients (equivalent to the MSD_r of eqs. (3) and (4)) from X-ray Total Scattering data for five powder samples with average diameters, D_{sphere} = 1.78, 2.47, 3.06, 3.72 and 11.2 nm, respectively (see Figure 4-2 and Table 1 in (Shi C. 2013)). The experimental U_{ISO}, being an average value obtained by modelling the PDF with a traditional (constant) Debye-Waller factor, can be related to an average MSRD as:

$$2U_{ISO}^2 \cong \overline{MSRD} = \frac{\int_0^{r_{max}} \overline{\sigma_{ij}^2}(r) g(r)\, r^2\, dr}{\int_0^{r_{max}} g(r)\, r^2\, dr} \qquad (4\text{-}41)$$

(by mistake the r^2 in eq. (4-41) was missing in the original article (F. A. Scardi P. 2018)).

The average of the MSRD in eq. (4-41) is made over all shells within the maximum distance in the crystal, r_{max}, and is weighted over the population of each shell, given by the Radial Pair Distribution Function (RPDF), $g(r)$. The last can be calculated using the already cited software VMD for simulated spherical Pt crystals with a number of atoms N, given by (A. O. Shafai G. 2012):

$$N = \left(\frac{D_{sphere}}{1.105 D_{at}}\right)^3 \qquad (4\text{-}42)$$

where $D_{at}=a/\sqrt{2}$, with a = 3.92 Å, average unit cell parameter for platinum.

Therefore, given the literature value of the Debye temperature for Pt (Θ_D=237K), the condition of eq (4-41) can be applied to the CD model of eq. (4-37) and (4-40) to determine the static component of the MSRD, $\overline{\sigma_{ij}^2}_0$. This procedure is straightforward if the same simplifying assumption of a constant static component is used. Results are shown in Figure 4-13 (a), where the RMSRD is plotted as a function of r for the five Pt nanocrystals of Shi *et al*. (Shi C. 2013), whereas corresponding values of $\sqrt{\overline{\sigma_{ij}^2}_0}$ are shown in Figure 4-13 (b).

As already observed for simulated Pd nanocrystals in Figure 4-6, also the RMSRD for the Pt nanocrystals rises to values increasingly larger than the bulk for decreasing nanocrystal size. This increase in RMSRD is due to dynamic and static components, as prescribed by eq (4-40). According to the CD model we can single out the effect of the static component which, as shown in Figure 4-13 (b), markedly depends on the nanocrystal size. As expected, $\sqrt{\overline{\sigma_{ij}^2}_0}$ increases steeply for small nanocrystals, for the increasing relevance of the static disorder in the surface region; the observed trend correctly points out the static component tending asymptotically to zero for large (bulk) crystal size.

Contrary to most models in the literature which refine a size-dependent Debye temperature to deal with vibrational effects in nanocrystals, in the present CD model Θ_D is kept constant to the bulk value. The dynamical component of the MSRD is uniquely determined by the nanocrystal size, for the corresponding phonon confinement effect, so that the static MSRD can be singled out. In the present application to the Pt data $\overline{\sigma_{ij}^2}_0$ was assumed constant, but more complex, *r*-dependent models can easily be implemented in eq. (4-40).
The analysis presented above for Pt nanocrystals is just an example of a possible application of the new CD models. A better and more consistent procedure would require the introduction of the CD model directly in the analysis of the PDF, so that an *r*-dependent MSD_r would replace the traditional constant DW coefficient, and the analysis might refine a constant Debye temperature for all nanocrystal sizes and different static components for the different diameters. This approach will be tested in future experimental studies on the PDF of nanocrystalline metal catalysts.

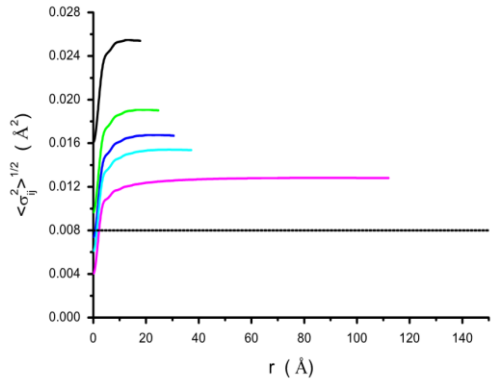

Figure 4-13

RMSRD ($\sqrt{\overline{\sigma_{ij}^2}}$) as a function of the distance in five samples of nanocrystalline Pt from (Shi C. 2013), with average diameters: 1.78 nm (black line), 2.47 nm (green line), 3.06 nm (blue line), 3.72 nm (light blue line), and 11.2 nm (magenta line); the straight dash line is the literature value for bulk Pt [42] (a); the corresponding static component of the RMSRD ($\sqrt{\overline{\sigma_{ij}^2}_0}$) as a function of the nanocrystal diameter (D_{sphere}) is shown in (b).

4.6 Concluding Remarks

The Correlated Debye model was originally developed for bulk (strictly speaking, infinite) crystals, to calculate the Debye-Waller coefficient for the inner coordination shells, where the effect of correlated atomic motions is strongest. As shown in this chapter, the finite size of the crystalline domain introduces a lower cut-off in the VDOS, caused by the maximum allowed vibrational wavelengths. The new CD model accounts for this phonon confinement effect and introduces an upper bound in the VDOS, which is also a function of the crystalline domain size.

Although based on rather basic approximations, the revised CD model correctly encodes the main effect of domain size on the vibrational properties of nanocrystals. By further introducing a static displacement component resulting

from undercoordination of the surface atoms, the new model matches the mean square relative displacement calculated from Molecular Dynamics simulations of cubic Pd nanocrystals, as well as results of an experimental study on spherical Pt nanocrystals.

Moreover, the definition for the purely thermal component of the MSRD (eq. (1-29)) is in accord with the modified CD model described in this chapter. This cross validation is fundamental for the simple model developed in the following chapter.

APPLICATION: VIBRATIONAL PROPERTIES OF PD NANOCUBES

Part of this chapter is based on the published article:

"Vibrational properties of Pd nanocubes", Flor, A.; Feliu, J.M.; Tsung, C.-K.; Scardi, P. Vibrational Properties of Pd Nanocubes. *Nanomaterials* 2019, *9*, 609

https://doi.org/10.3390/nano9040609

5.1 INTRODUCTION

This chapter investigates the thermal behaviour of Pd nanocubes, about 24 nm edge. The synchrotron radiation beamline 11BM at the Advanced Photon Source (APS) of Argonne National Laboratory (ANL) supports the measurement of high quality XRPD patterns from which B_{ISO} values can be obtained by modelling the line profiles collected at three temperatures: 100, 200, and 300K. As expected, DW coefficients are larger than those reported for bulk Pd, and the difference can be explained by varying contributions from the dynamic and the static disorder. MD simulations show the origin of the two contributions, and the role of the correlated displacements of neighbouring atoms. The trend of the MSRD (Mean Square Relative Displacement) can be obtained as a function of the radius of the coordination shells in the nanocrystals, showing the effect of the size and shape of the nanocrystals, providing the means to single out static and dynamic contributions. A simple model, requiring just a single adjustable parameter for each contribution, is used to fit the experimental data. While the first model, concerning static disorder, stems directly from the trend of the MSRD obtained from MD simulations, the second one follows a recent extension of the correlated Debye model accounting for the effect of the finite size of the nanocrystals, chapter 4 (F. A. Scardi P. 2018)

5.2 EXPERIMENTAL

Pd nanocubes were produced following a procedure derived from (Jin M. 2011).

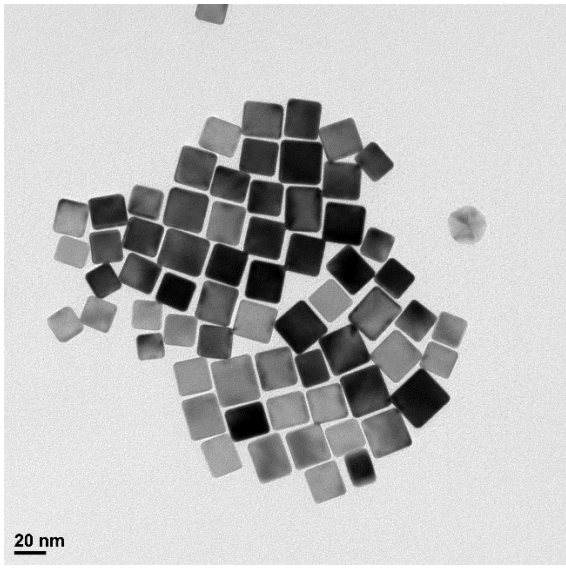

(a)

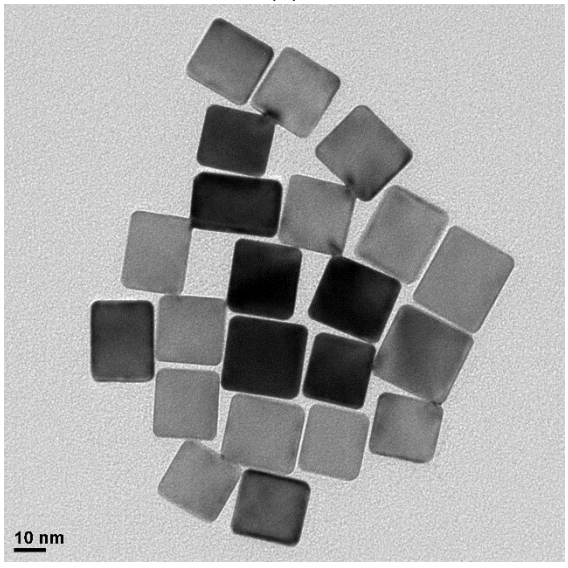

(b)

Figure 5-1

TEM pictures of the Pd nanocubes (see Supporting Information in (Solla-Gullón J. 2015)*).*

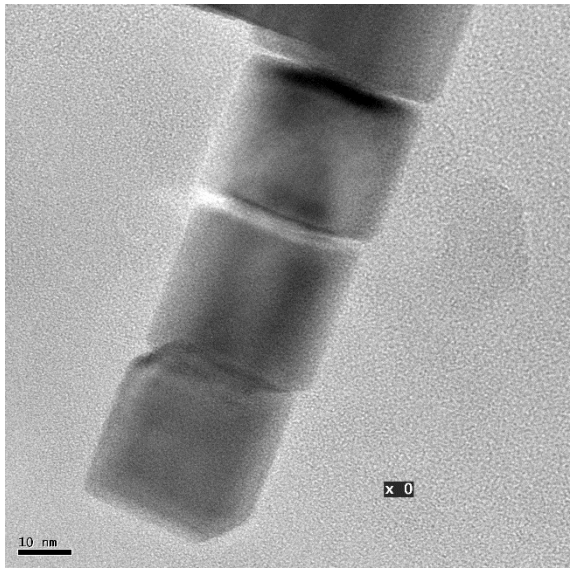

(c)

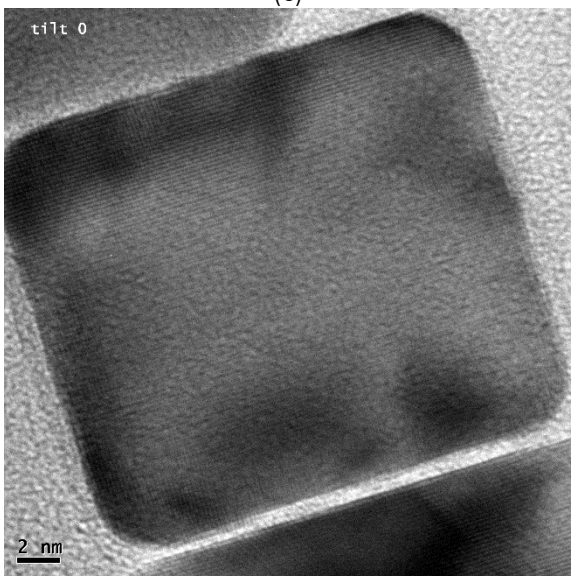

(d)

Diffraction data were obtained from capillaries (Kapton tubes, 0.8 mm diameter) loaded with concentrated nanocrystal dispersion, allowed to dry for a few days and then sealed with epoxy. Data were collected at 11-BM, the powder diffraction beamline of APS-ANL, using 30 keV radiation (actual wavelength from calibration procedures with standard Si powder: λ = 0.0413692 nm) with the traditional Debye-Scherrer geometry: full details on

11-BM operating conditions can be found in (Wang J. 2008) and website of the facility. The capillary, rotated at 4200 rpm, was analysed at three temperatures: 100, 200, and 300 K; measurements were made on a spot previously selected for the low absorption ($I/I_0 \leq 0.02$), such that no intensity corrections are necessary in the modelling of the patterns.

The XRD patterns collected at the three temperatures were analysed together, using the Whole Powder Pattern Modelling (WPPM) approach in a modified version of the PM2K software ((A. R.-D. Scardi P. 2018) and references therein). The instrumental profile was acquired by modelling the pattern of standard LaB_6 powder (NIST SRM-660b), whereas the pattern of the sample holder was obtained from an empty kapton capillary, modelled by pseudoVoigt curves (a. L. Scardi P. 2016) and adapted to the Pd filled capillary by means of an adjustable scale parameter.

Size and strain broadening models were the same for the three temperatures: domain shape, as suggested by TEM, is a truncated cube (thus exposing 110 and 111 facet in addition to the 100 cube faces); the modelling allows the refinement of the truncation level, in addition to the mean and variance of a lognormal distribution of edge lengths (A. L. Leonardi 2012); for the strain component the Popa-Adler-Houska (PAH) model has been used (Scardi P 2017) (A. R.-D. Scardi P. 2018), which adapts well to the case of nanocrystals (A. L.-K. Scardi P. 2015), providing also for the anisotropy of atomic displacement in the nanocubes. Besides scale parameters and coefficients of the (Chebyshev) polynomial background, Pd unit cell parameter and DW coefficients were refined independently, for each of the three patterns, to account for the effect of temperature. B_{ISO} enters the traditional DW factor decreasing the Bragg scattering intensity, as well as the Thermal Diffuse Scattering (TDS). The TDS was modelled according to (Beyerlein 2012), to take into account the effect of finite size of the crystalline domains.

5.3 ATOMISTIC MODELLING

5.3.1 Molecular Dynamics, MSD and MSRD

Nanocrystal models were constructed by replicating the primitive unit cell (with the unit cell parameter of bulk Pd, a_0 = 0.3890 nm (WebElements n.d.)) in ideal atomic arrangements, until the space was filled. A condition was enforced to the atomic coordinates, in order to keep only those atoms belonging to the desired geometrical shape. This system was the starting step for MD simulations, run as described in paragraph 1.3.

MD provides the trajectory in time of each atom in the nanoparticle, $r_i(t)$, from which time average position, $\overline{r_i}$, and variance (MSD), $\overline{\sigma_i^2}$, can be easily derived. Likewise, the distance between any two atoms, $r_{ij}(t)$, can be used to obtain the MSRD, $\overline{\sigma_{ij}^2}$. For monoatomic systems for which $\overline{\sigma_i^2}$ can be assumed constant throughout the particle (which is clearly an approximation), the two squared displacements are related by:

$$\overline{\sigma_{ij}^2} = 2\overline{\sigma_i^2} - 2\overline{\sigma_i \cdot \sigma_j} \qquad (5\text{-}1)$$

where the second term is the DCF. The DCF accounts for the correlation of atomic motions and is significantly different from zero for the first (innermost) coordination shells. As it is known, the DW coefficient used in traditional XRD models is proportional to the MSD, whereas other spectroscopies, like XAS, provide the MSRD, and a richer information on the local atomic environment of the innermost coordination shells (Calvin 2013) (Fornasini 2014).

The actual quantities to compare with experimental results must involve a spatial (configuration) average, i.e., an average over all atoms or couples of atoms. From the MD trajectory the MSRD can be calculated as a function of the number of unique atom pairs, N_{S_r}, and radius, *r*, of the coordination shells S_r in the nanocrystal

$$\overline{\sigma_r^2} = \frac{1}{N_{S_r}} \sum_{i,j \in S_r} \overline{\sigma_{ij}^2} = < \overline{\sigma_{ij}^2} >_r . \qquad (5\text{-}2)$$

MD also provides the means to single out the static component of displacement, in a way inaccessible to experiments. In fact, given the MD trajectory, made of a series of "snapshots" of the nanoparticle in time, the spatial average of eq. (5-2) can be calculated for the time average of distances, $\overline{r_{ij}}$:

$$\sigma_{0,r}^2 = \frac{1}{N_{S_r}} \sum_{i,j \in S_R} \left(\overline{r_{ij}} - \frac{1}{N_{S_r}} \sum_{i,j \in S_R} \overline{r_{ij}} \right)^2 = < \left(\overline{r_{ij}} - < \overline{r_{ij}} > \right)^2 >_r . \quad (5\text{-}3)$$

While Equation (5-2) provides the overall MSRD, including all (static and dynamic) components of the displacement, Equation (5-3) gives the static component only. It is; therefore, possible to obtain a good estimate of the dynamic (thermal) component alone from the difference between Equations (5-2) and (5-3), assuming that the two MRSDs can be treated as variances of independent distributions:

$$\overline{\sigma_{T,r}^2} \simeq \overline{\sigma_r^2} - \sigma_{0,r}^2 = < \overline{r_{ij}^2} >_r - 2 < \overline{r_{ij}}^2 >_r + < \overline{r_{ij}} >_r^2 . \quad (5\text{-}4)$$

Figure 5-2(a) shows the trend of the MSRD, according to Equations (5-2)–(5-4), as a function of *r* in a spherical Pd nanoparticle of about 5 nm diameter (N = 6986 atoms). Similar calculations can be performed for any desired particle shape. Figure 5-2(c), (d) refer to a Pd cube, about 4 nm edge (N = 4923 atoms), with truncated corners and edges. This is the shape suggested by TEM images and by the modelling of the XRD patterns of this study; indeed, the extent of the truncation is that obtained by WPPM (see below), while the size in the simulation is smaller than in the experimental sample to limit the computation time. The last is not a limitation because, quite interestingly, the trends are characteristic of the nanoparticle shape: By increasing the nanocube size the MSRD trends are the same, provided that the abscissa (shell radius) is stretched to match the edge length (or the diameter for spherical nanoparticles). The scalability of the MSRD trends is demonstrated in Figure 5-3 for the static MSRD component (equation Figure 5-4) in a selection of spheres and truncated cubes of increasing size.

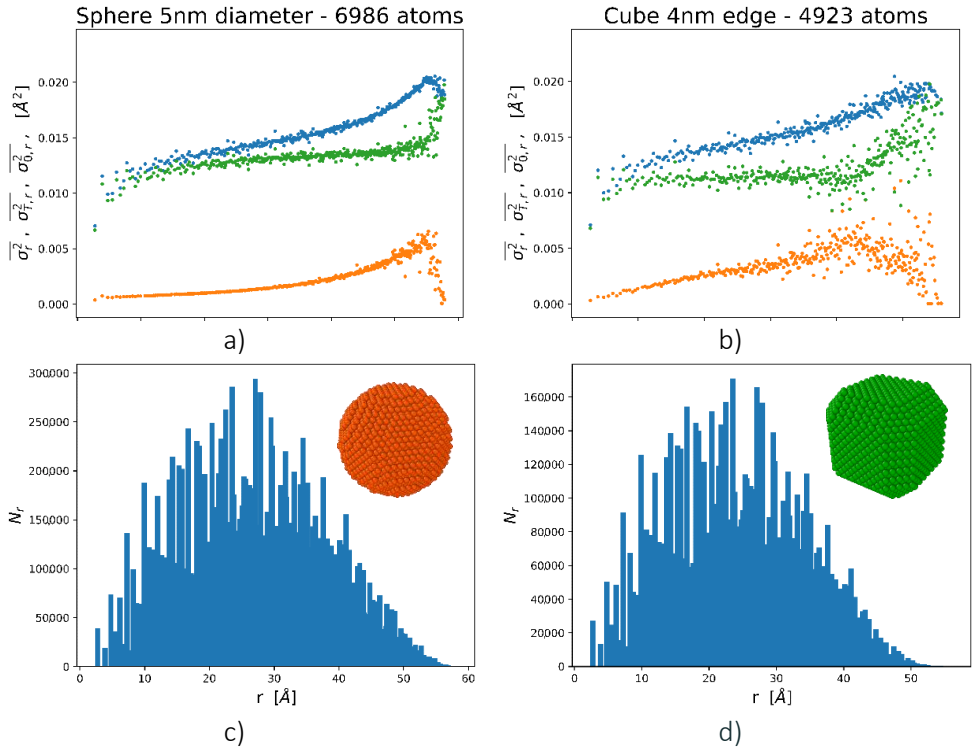

Figure 5-2

*Trends of the Mean Square Relative Displacement (MSRD) for a spherical (**a**) and truncated cube (**b**) crystal, N = 6986 and N = 4923 Pd atoms, respectively; corresponding number of atom pairs (N_r) is shown by histograms in (**c**) and (**d**). MSRD is shown for the total (blue), static (orange), and thermal (green) components, as of Equation(5-2), (5-3), and (5-4), respectively. Insets in (**c**) and (**d**) show images of the nanoparticle shapes.*

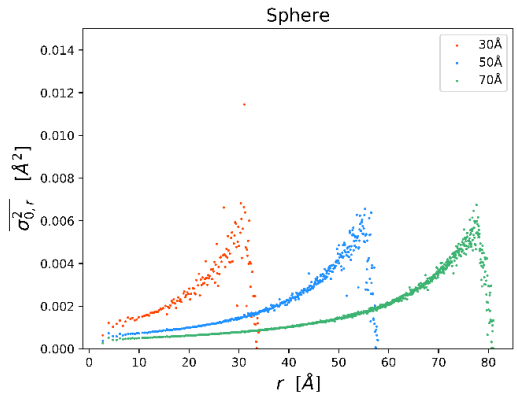

a)

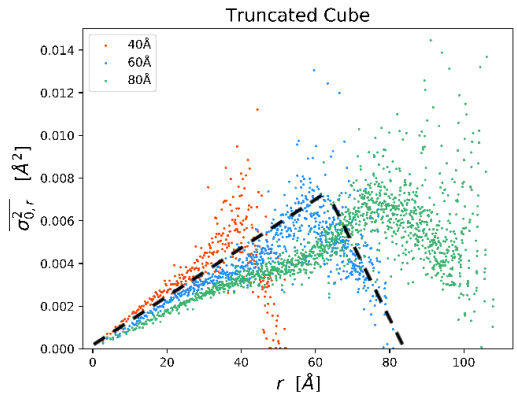

b)

Figure 5-3

*Static MSRD component from Molecular Dynamics (MD) simulations for three spheres (**a**) and three truncated cubes (**b**) of increasing size. The dotted line is the trend according to the parametric model of Equation (5-6).*

As already pointed out, different spectroscopies can access different aspects of the disorder and the vibrational characteristics of the nanocrystals. XRD generally gives the MSD, which can be related to the average of the trends in Figure 5-8., weighted over N_{S_r},

$$B_{ISO} = \frac{8}{3}\pi^2 < u^2 > \simeq 8\pi^2 \frac{1}{N_S} \sum_{r}^{r_{MAX}} N_{S_r} \frac{\overline{\sigma_r^2}}{2} \qquad (5\text{-}5)$$

where $N_S = \sum_r^{r_{MAX}} N_{S_r} = N\frac{(N-1)}{2}$ is the total number of unique atom pairs in a crystal with *N* atoms. EquationFigure 5-9 can also be used to assess the separate contributions of the static or the thermal components, as better illustrated in the following.

5.3.2 Modelling the MSRD components

While MD simulations provide full details of disorder for each coordination shell, experiments have a much more limited scope, and generally allow the measurements of fewer, global parameters, like B_{ISO} in eq. (5-5) . However, by introducing some reasonable approximations, the MSRD trends can also be related to the experimental evidence from XRD. The thermal component, $\overline{\sigma_{T,r}^2}$, can be described by a Correlated Debye (CD) model (Beni G. 1976) (Vaccari M. 2006), as adapted to nanocrystals in chapter 4: given the number of atoms (or equivalently, the nanoparticle size and shape) and temperature, the trend of $\overline{\sigma_{T,r}^2}$ can be modelled by adjusting a single parameter, the Debye temperature.

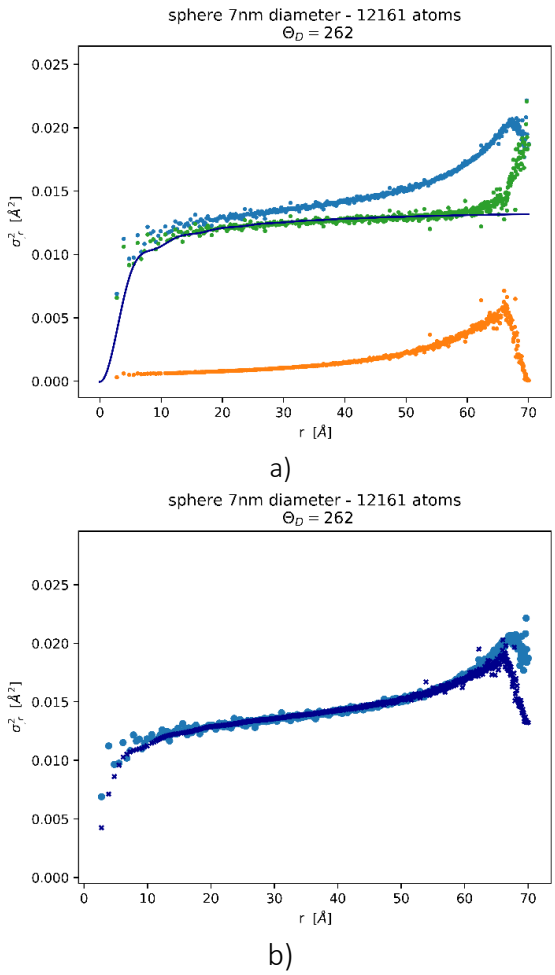

Figure 5-4

*. MSRD trends for a spherical Pd nanocrystal with 7 nm diameter (N = 12161 Pd atoms): total (blue), static (orange), and thermal (green) components of MSRD, with the best fit of the Correlated Debye (CD) model (line) (**a**). The sum of CD model and static component (dark blue) is compared with the total MSRD (blue) (**b**).*

As an example, Figure 5-4 (a) shows the data for a spherical Pd nanoparticle of diameter 7 nm, with N = 12161 Pd atoms. Besides the two (static and dynamic) components and the total MSRD, the figure also shows the trend of the CD model. The best fit of the thermal MSRD component was obtained for Θ_D = 262 K, in agreement with the results of (F. A. Scardi P. 2018) for a system of Pd nanoparticles from 3 to 20 nm. The value is not far from the experimental bulk value of 272 K (Butt 1988). The difference is justified, by inevitable discrepancies between EAM potential and reality, but also by the fact that Pd atoms on the surface vibrate with a larger amplitude than in the core, so that the average MSD and MSRD increase slightly, and consequently Θ_D decreases. In Figure 5-4 (b) we can see that the sum of CD model and static MSRD (dark

blue symbol) matches quite well the total MSRD from the MD simulation. Discrepancies are observed for more distant shells, involving atoms on the surface which, as already pointed out, have a larger vibration amplitude. However, given the decaying trend with distance of the weight function N_{S_r} (Figure 5-2 (b), (d)), the effect of such deviations on observables like B_{ISO} (equation (5-5)) is small.

For the static component we can exploit the scalability property demonstrated in Figure 5-3: $\overline{\sigma_{0,r}^2}$ values start from zero at $r = 0$, go through a maximum and then drop to zero again for the longest distance in the particle. As already pointed out and shown in Figure 5-3, changing the size has only the effect of stretching the trend to longer distances, whereas the maximum $\overline{\sigma_{0,r}^2}$ value is comparable among different sizes.

It is; therefore, tempting to approximate the observed trends for the truncated cubes (Figure 5-3 (b)) by a simple linear model. The maximum value is found for a distance of the order of the cube edge, i.e. when most of the pairs of atoms are composed of a surface atom and a second distant atom, but in the core region. Static MSRD falls to zero for the maximum distance in the nanocube (i.e., when pairs are made of atoms on opposite surfaces, thus displaced in similar way).

In a practical implementation of this model, if the nanocrystal size and shape are known (from simulations or from experiments), the trends in Figure 5-3 (see the dotted line) can be easily parameterized leaving the maximum, $\sigma_{0,max}^2$, as the only adjustable parameter:

$$\overline{\sigma_{0,r}^2}\begin{cases} \sigma_{0,max}^2\,(r/D) & if\ 0 \le r \le D \\ \sigma_{0,max}^2\,(r - D_{max})/(D - D_{max}) & if\ D \le r \le D_{max} \\ 0 & if\ r \ge D_{max} \end{cases} . \qquad (5\text{-}6)$$

Cube edge (D) and maximum distance in the truncated cube (D_{max}) are obtained from the size broadening of the Bragg peaks in the experimental XRD patterns. Indeed, WPPM refines values of mean size (D) and truncation level, from which total number of atoms and D_{max} are readily determined.

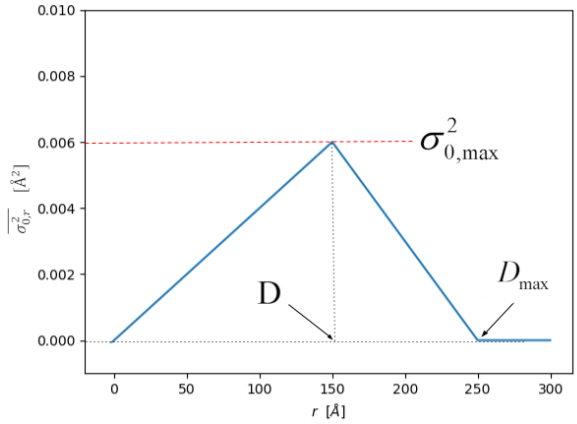

Figure 5-5

Graphical explanation of equation (5-6)*. The function is a simplification of the static component trend calculated from MD simulations*

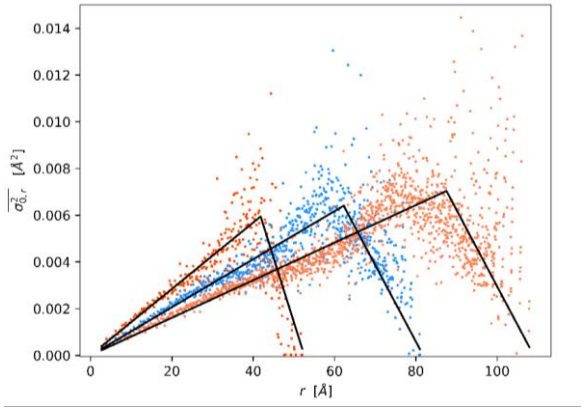

Figure 5-6

Static MSRD results from Figure 3 in the main text with static model of equation (5-6). Best fit of $\sigma^2_{0,max}$ are, respectively, 0.00594 (D = 41.84 Å), 0.00640 (D = 62.26 Å), and 0.00703 (D = 87.54 Å).

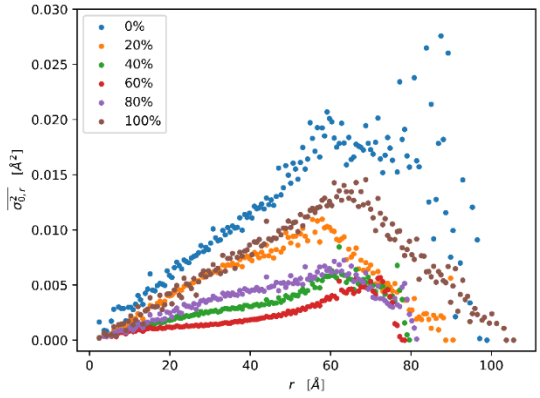

a)

Figure 5-7

Static MSRD results for nanoparticle of roughly the same number of atoms of a cube of edge 6 nm (15,000 atoms), but with different degrees of truncation (0% is a cube, 100% an octahedron). The overall shape is always similar to the expression (5-6)*, except for the case of more "spherical" shapes (truncation 40% and 60%) that exhibit a trend closer to the sphere (*Figure 5-3 *in main text). Compared to previous images, the data have been presented with larger bins for a better visualization of the trends.*

In this way, the experimental values of B_{ISO} obtained in the present study at different temperatures can be matched by a model with the maximum static MSRD, $\sigma^2_{0,max}$, and the Debye temperature for the thermal MSRD, as adjustable parameters:

$$B_{ISO}^{exp\,t}(T) \simeq 4\pi^2 \frac{1}{N_S} \sum_{r}^{r_{MAX}} N_{S_r} \left[\overline{\sigma^2_{T,r}}(T; N, \Theta_D) + \overline{\sigma^2_{0,r}}(N, \sigma^2_{0,max}) \right] \quad (5\text{-}7)$$

5.4 Results & Discussion

WPPM results for the patterns collected at 100, 200 and 300K are shown in Figure 5-8.. The inset in (a) shows details of the peak tail region in intensity log scale, whereas the contribution of the TDS, increasing as expected with the temperature, is shown in (b); the inset in (c) shows the refined particle shape. Size and strain broadening (Figure 5-9) give the lognormal distribution of nanocube edges, *D*, (a) and the microstrain due to the inhomogeneous atomic displacement caused by the surface effect (b). In the last it is apparent the effect of the elastic anisotropy of Pd: like most *fcc* metals, Pd is stiffer along [hhh] than [h00], so that microstrain is correspondingly higher along [h00] than [hhh], with [hh0] on intermediate level. These results, obtained from the modelling of patterns at three temperatures, are not far from those of (A. L.-K. Scardi P. 2015)obtained from RT data only.

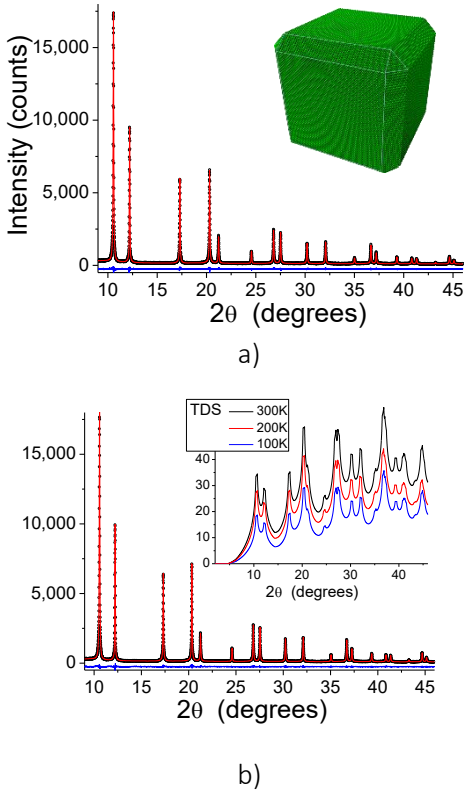

Figure 5-8.

WPPM results. XRD patterns (circle), model (line) and difference (residual, line below) at 100K (a), 200K (b) and 300K (c). Insets: in (a), intensity log scale plot; in (b), TDS component at 100K (blue), 200K (red) and 300K (black); in (c), refined shape of the truncated nanocube.

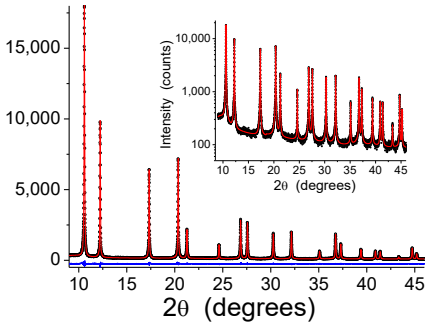

c)

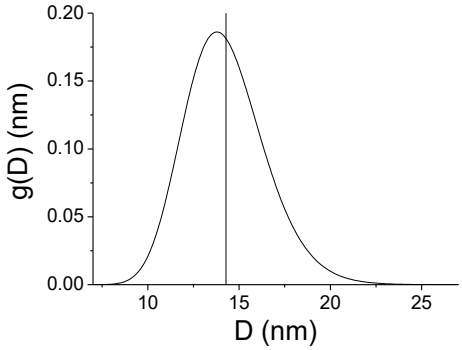

a)

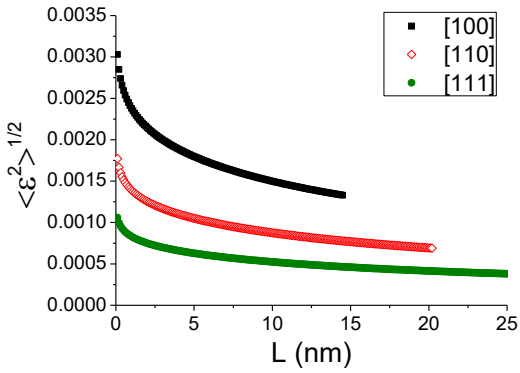

b)

Figure 5-9

*WPPM results. Lognormal distribution of cube edges, D (**a**) and microstrain distribution along three crystallographic directions: [100] (black), [110] (red), [111] (green) (**b**).*

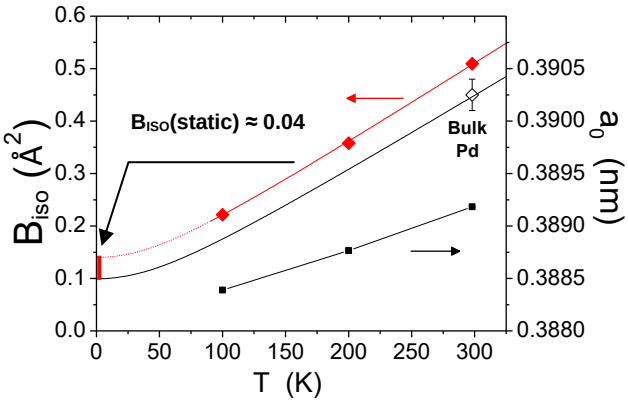

Figure 5-10

Left axis: Debye-Waller coefficient, B_{ISO}, from the XRD patterns collected at 100, 200, and 300K (♦) for the Pd nanocubes and corresponding room temperature (RT) value for bulk Pd (◊) (Butt 1988). Red line is the combined model of equation (5-7), black line is the extrapolation according to the Debye model for the literature bulk value. The arrow highlights the increase in the static component. Right axis: Unit cell parameter measured from the XRD patterns (▪). See text for details.

Figure 5-10 shows the results for the temperature dependent parameters, DW coefficient and unit cell parameter. They both increase with the temperature, but while the trend of the unit cell parameter is predictable on the basis of simple thermal expansion, the B_{ISO} values are significantly higher than those of bulk Pd. This feature, common to many nanocrystalline metals (Shi C. 2013) (Kuzmin A. 2014) (Agostini G. 2013), can be explained both qualitatively and quantitatively with the models discussed above, even though the latter is purely indicative with just three data points; collecting more data on a wider temperature range is priority for our future work.

However, it is interesting to show how the approach works. According to the CD model, the MSRD increases for smaller nanocrystals, for the effect of the decreasing number of atoms and of a reduced Debye temperature for the larger amplitude of the surface atom vibrations (F. A. Scardi P. 2018); the static component of the MSRD also increases because, as shown in Figure 5-3, the maximum region weights more on the average (measured) B_{ISO} for decreasing size. Therefore, both static and dynamic components of the MSRD (and B_{ISO}) increase for decreasing domain size.

The best fit of the model of equation (5-7) is shown as a red line in Figure 5-10, together with the experimental B_{ISO} values. As already mentioned, the number of atoms (N in equation (5-7)) is given by the WPPM, from the mean value of the edge length distribution (Figure 5-9 (a)), whereas $\sigma^2_{0,max}$ = 0.0015 Å^2 and

Θ_D = 271 K are obtained by the best fit of equation (5-7), using the CD model and equation (5-6). Once again, we underline that the results are purely indicative, as a credible fit would require more data points over a wider range of temperatures. However, it is quite evident that the refined value of $\sigma^2_{0,max}$ is lower than the maximum static MSRD given by the MD simulations (Figure 5-2, Figure 5-3 and Figure 5-4).

The present results suggest that EAM potentials may not be entirely appropriate to describe details of the surface properties of the crystals, which is not a surprise, and indeed a known limitation of EAM (Zhou L. G. 2012). EAM results differ even by changing the potential (e.g., using Sheng potential (Sheng H. 2018) instead of Zhou potential (Zhou X.W. 2004)). But it is also likely that the condition of the surface of real crystals, with the capping CTAB layer and the environment quite different from the vacuum assumed in the MD simulations, also play an important part. More investigations and extensions of the atomistic modelling to account for surface effects will be required, but the general principle can be put forward that DW coefficients of nanocrystals and their vibrational properties should be evaluated both based on dynamic (thermal) and static contributions.

5.5 Concluding Remarks

This chapter presents an approach to study the vibrational properties of large assemblies of nanocrystals, based on the combined use of a MSRD model and information from the XRD patterns collected at different temperatures. The XRD data, through the whole powder pattern modelling, provide detailed indications on the crystalline domain size and shape, as well as the trend with temperature of unit cell parameter and DW coefficient.

By separating the MSRD of the nanocubes into two contributions, we can highlight the effects of the static component and; therefore, gain a better understanding of the purely thermal proprieties of the nanocrystals. In fact, if the increase in MSRD is entirely attributed to the vibrational part, the Debye temperature tends to be underestimated. The present procedure, instead, returns values for ΘD that are closer to the bulk value, since part of the deviation in the finite size case is attributed to the static component (i.e., the

parameter $\sigma_{0,max}^2$ in the parametric model of equation (5-6)). Interestingly, the static component of the MSRD is peculiar to the nanoparticle shape (in this work, sphere or truncated cube), thus giving a different perspective on the increase of BISO.

Even if not correct in the finer details, like anisotropy and anharmonicity, the proposed model is sufficiently simple and informative to be flexibly used for most nanocrystalline systems, to grasp the main effects of the static and dynamic disorder on spectroscopic results. For best results, BISO data should be collected for different values and over a wide temperature range, a condition that requires more experimental efforts in the future.

FINAL CONCLUSIONS

This thesis proposes a new methodological paradigm to the study of nanocrystalline materials, where the interpretation of results from different analytical techniques is directly supported by atomistic models and computational simulations. This not only allows the calculation of observable properties, but also provides a new and original point of view: contributions to the observed properties can be singled out in a way impossible to experiments. Moreover, once the results of a simulation are validated by the experimental evidence it is directly possible to run more simulations. This allows us, as far as enough computational power is available, to build large sets, potentially an infinite amount, of simulated samples, a possibility clearly precluded to real experiments.

This work has proved the importance of the nanoparticle shape, besides and even beyond the more familiar effect of the size. A strong point of simulation has been exploited: as all the atom trajectories can be stored during simulation, whatever quantity based on atomic positions and velocity can be calculated, an option exploited to study the thermal contribution to the MSRD.

The work has also shown that MSRD, and its static directional variant σ^2_{hkl}, provides the means to discern nanoparticles shapes and their surface disorder. It is also a quantity that can naturally bridge different experimental techniques, giving insights on the microstructure (e.g., as seen in chapter 3: "Application: Debye-Waller coefficient of heavily deformed nanocrystalline iron ").

Moreover, the total (full) MSRD can be approximated, reasonably well, as the sum of two components, a dynamic and a static one. While the former behaves similarly to a bulk system and it is therefore obtainable from literature or existing models (like the Correlated Debye displacement model), the latter is peculiar to the nanoparticle shape but follows nonetheless a defined trend and it can also be calculated or described by simple analytical approximation.

More refined potentials or even more detailed numerical techniques, like Density Functional Theory, could be employed, especially to obtain more realistic results for the surface behaviour of the nanoparticle. The order of the steps to undertake, and in general the overall procedure, is nonetheless identical to the one employed in this work, even if more complex.

Albeit not complete in its description, the use of EAM potentials gives qualitatively sound results, and these are of uttermost importance as a benchmark for future, and more complex, potentials aiming to better describe the nanoparticle surface interaction with the external agents.

APPENDIX

7.1 SURFACE AND VOLUME OF TRUNCATED CUBE (WITH TRIANGULAR FACET {111})

All the particle renderings in figures are made with OVITO (Stukowski A. 2010)

Definition: a truncated cube with triangular facet is a cube where edges and vertices are partly removed. The truncation is a number $\mathrm{p} \in [0,1]$ such that p=0 for a perfect cube of edge l, and p=1 for an octahedron of edge $\mathrm{a} = l/\sqrt{2}$.

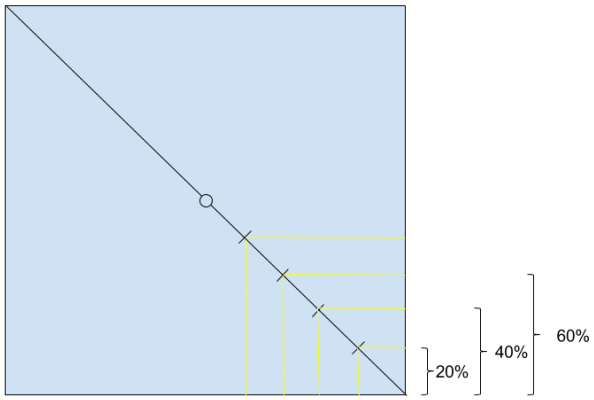

Figure 7-1

Naming convention for different degrees of truncation, based on the fractions of the face diagonal.

A cube corresponds to a truncation value of 0%, while 100% truncation yields an octahedron.

This kind of truncation is obtained by defining 3 points for each cube vertex for a total of 24 points, that are the vertices of the triangular facets. The convex volume delimited by the 24 point is considered the **truncated cube**.

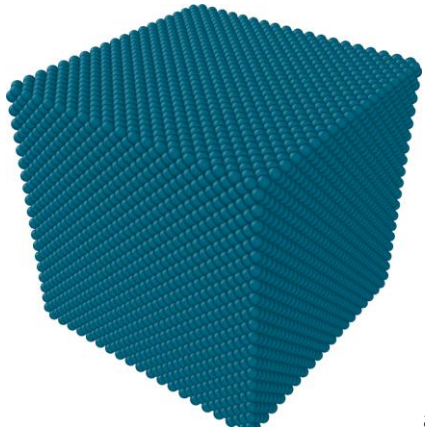

a)

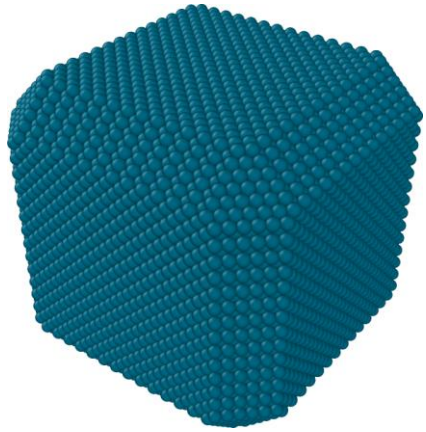

b)

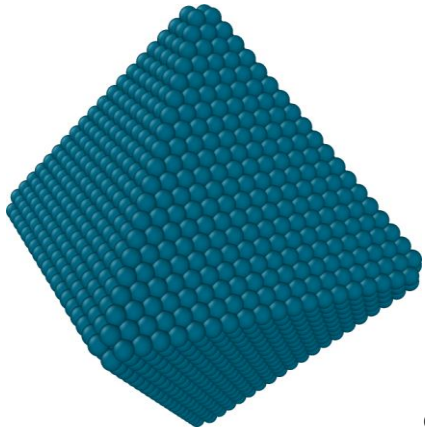

c)

Figure 7-2

Nanoparticles with three different degrees of truncation:

a) Truncation 0% (p = 0)
b) Truncation 30% (p = 0.3)
c) Truncation 98% (p = 0.98)

If the cube is centred in the origin, **cube** vertices are in positions $(\pm l/2, \ \pm l/2, \ \pm l/2)$. One can just focus on the $x > 0, \ y > 0, \ z > 0$ region, thus leaving 7 regions with identical properties. Let us call this subsection of the cube **eighth of truncated cube**.

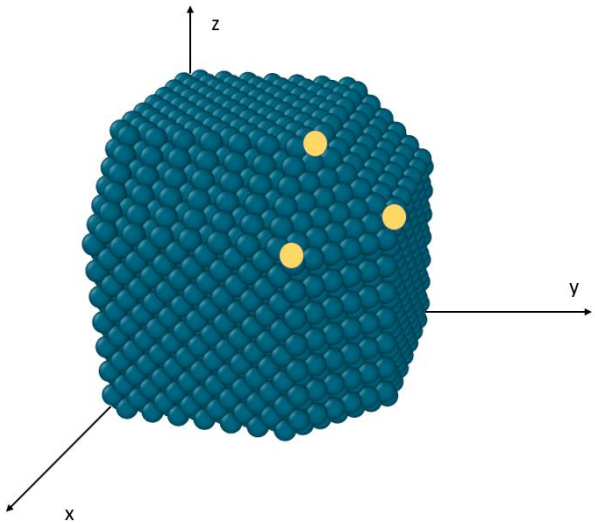

Figure 7-3

The three delimiting points. For every cube vertex three similar points are defined. The particle will be the space region (maximum convex volume) delimited by the planes containing all 24 points.

In this region, the facet vertices are in positions:

$$v_1 = (l(1-p)/2,\ l/2,\ l(1-p)/2)$$
$$v_2 = (l/2,\ l(1-p)/2,\ l(1-p)/2)$$
$$v_3 = (l(1-p)/2,\ l(1-p)/2,\ l/2) \quad (7\text{-}1)$$

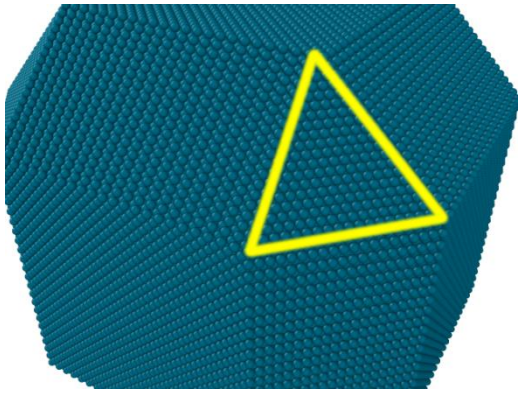

Figure 7-4

The triangular facet along the direction [111]

This kind of truncation is obtained by defining 3 points for each cube vertex for a total of 24 points, that are the vertices of the triangular facets. All the convex volume delimited by the 24 point is considered the **truncated cube**.

7.1.1 Surface:

The surface of the shape is eight times the surface of the eighth. The surface of the eighth is given by 3 squares (S1), 3 rectangles (S2) and 1 triangle (S3).

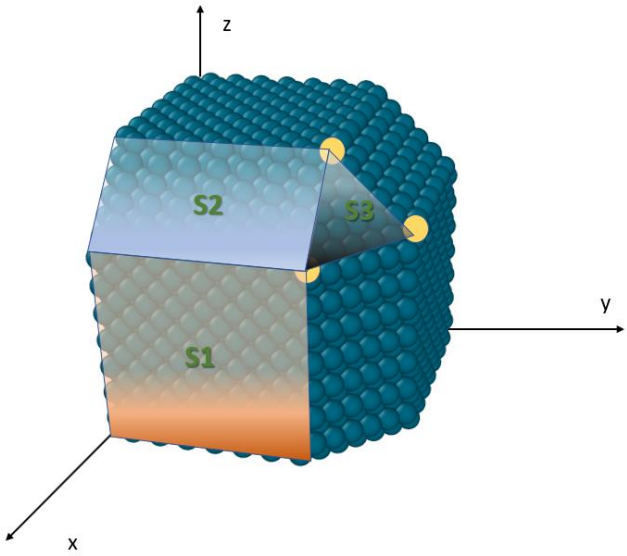

Figure 7-5

The three main kind of surfaces in a truncated nanocube, highlighted and labelled as in the main text.

The three elements have dimensions:

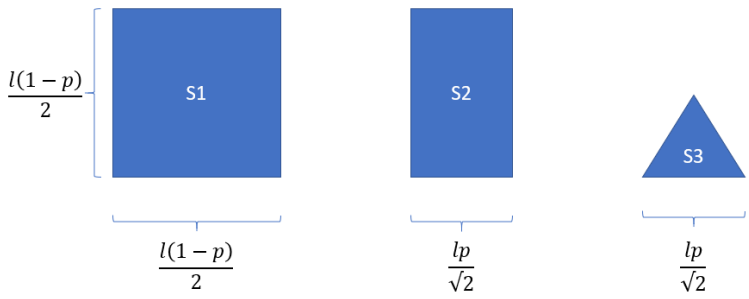

Figure 7-6

Area of the different faces as function of the cube edge l and truncation parameter p.

The total surface is

$$S_{tot} = 8 \cdot \left\{ 3 \cdot \left[\frac{l(1-p)}{2} \right]^2 + 3 \cdot \left[\frac{l(1-p)}{2} \frac{\sqrt{2}lp}{2} \right] + \frac{\sqrt{3}}{8} l^2 p^2 \right\} \qquad (7\text{-}2)$$

S1 S2 S3

7.1.2 Volume:

To calculate the volume it is better to calculate the full volume without truncation and subtracting the missing part (Figure 7-7).

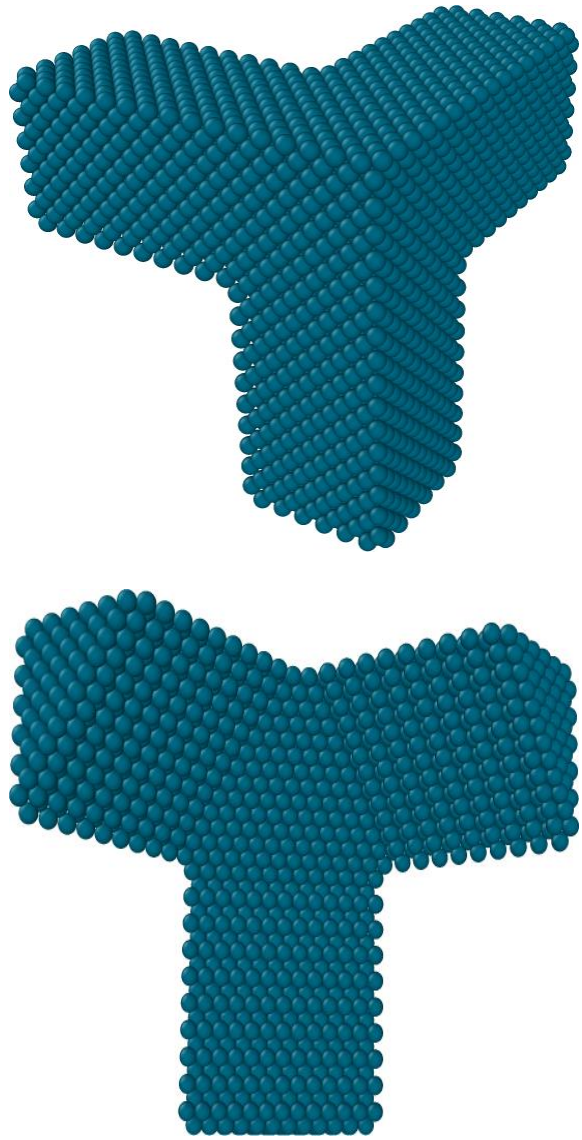

Figure 7-7

The missing volume of a truncated cube carved out of a bigger perfect cube.

This missing volume can be divided in the contribution of 3 triangular parallelepipeds:

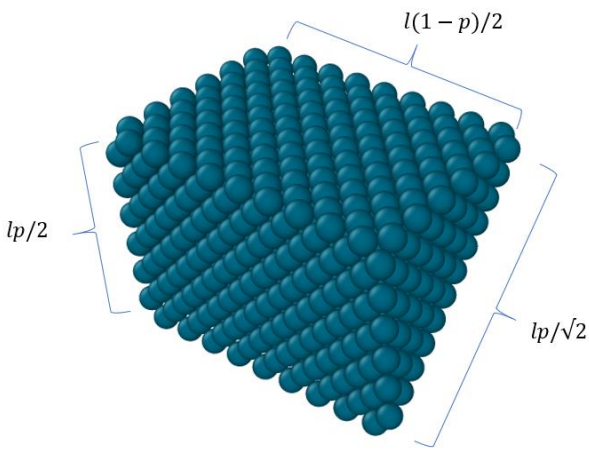

Figure 7-8

Volume of the one missing part as a function of cube edge and truncation parameter.

and a smaller cube with a missing pyramid:

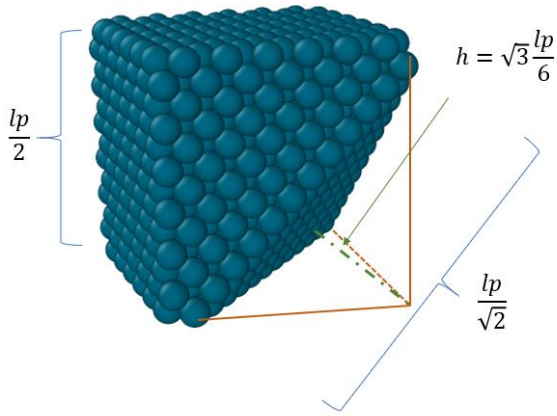

Figure 7-9

Volume of the one missing part as a function of cube edge and truncation parameter.

The last volume (Figure 7-9) is the volume of the full cube $(lp/2)^3$ minus the volume of the pyramid, which is $l^3p^3/48$.

Te total volume for the whole truncated cube is eight times the volume calculated up to this point:

$$V_{tot} = 8 \cdot \left\{ \underbrace{\left(\frac{l}{2}\right)^3}_{\text{Volume of perfect cube}} - 3 \cdot \underbrace{\left[\frac{1}{16} l^3 p^2 (1-p)\right]}_{\text{Volume of parallelepiped}} - \underbrace{\left(\frac{lp}{2}\right)^3 \left(1 - \frac{1}{6}\right)}_{\text{Volume of smaller cube minus pyramid volume.}} \right\} \quad (7\text{-}3)$$

From the expression we see that:

- For p= 0 (perfect cube) the volume is just l^3.
- For p=1 (octahedron of side $l/\sqrt{2}$) the volume is $l^3/6$, as expected.

7.2 Details on Truncation

A critical aspect in building models of nanocubes is the truncation. If atoms are left at the edges and vertices, during the simulation these atoms will behave erratically, affecting the displacement function in a rather strong and unpredictable way. From experimental observations (e.g., TEM images) it can be seen that real nanoparticles present no sharp edges, and for rather energetic reasons tend to have blunted extremes. When simulating cubic shaped nanoparticles, even if close to a geometrical cube, it is therefore better to remove the atoms at the extremes, characterized by too low coordination and thus unstable.

To prove that surface atoms play a major role in determining the vibrational properties, we focus on the case of a perfect cube. From a cube we can remove the 8 atoms at the corners, or we can remove the whole edges (12 lines of atoms). The results in the Warren Plot (shown for the direction [111] which is along the cube body diagonal) change drastically in the 3 cases.

Perfect cube:

Keeping all atoms, even the most under-coordinated atoms at the 8 corners (coordination is down to 3). We see from the image below that some kind of "splitting" takes place for different sizes (Figure 7-10). The behavior of long-distance pairs does not follow a common trend.

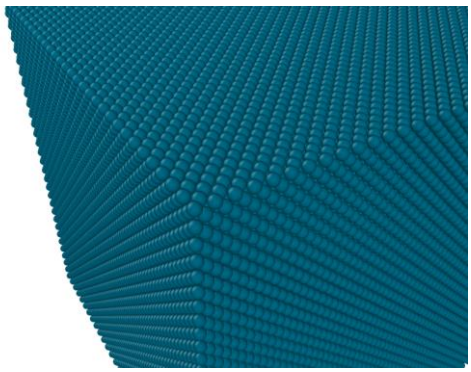

a)

Figure 7-10

a) Detail of a cubic model with atoms at the vertices
b) σ_{hkl}^2 for "perfect" cubes of different sizes. (the abscissa is normalized to unity as described in the previous chapter)

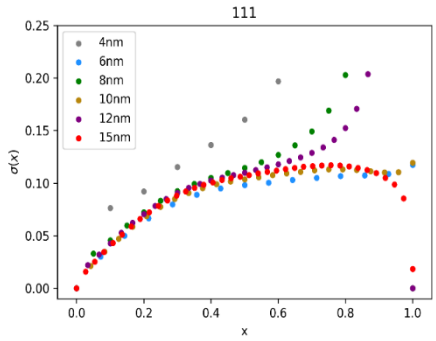

b)

Vertices removed:

Just by removing 8 atoms from vertices it can be seen that all trends become more similar (Figure 7-11); however, there is still a "splitting" of the trends, but it is confined only to the most distant coordination shells.

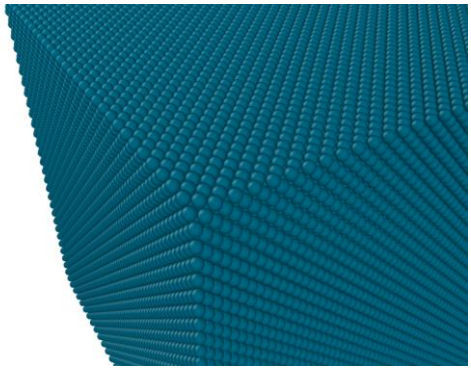

a)

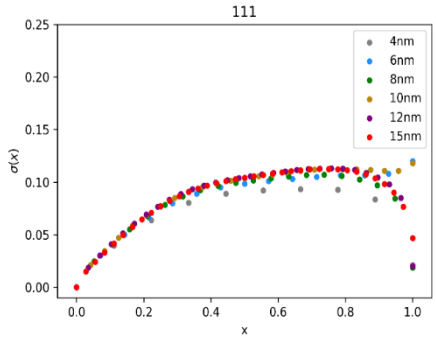

b)

Figure 7-11

a) Detail of a cubic model without the atoms at the vertices, but still with sharp edges
b) σ_{hkl}^2 for cubes of different sizes, with 8 atoms at vertices removed.

Edges removed:

In the last case (Figure 7-12), where atoms in corners and edges are removed, the trends in the Warren plot are similar for all sizes.

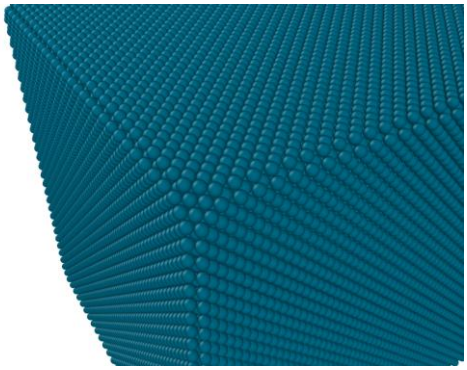

a)

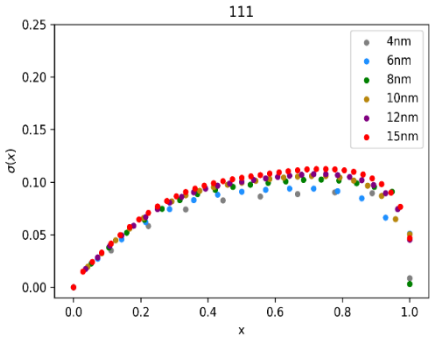

b)

Figure 7-12

a) Detail of a cubic model without the atoms at the vertices and along the edges
b) σ_{hkl}^2 for cubes of different sizes, 8 vertices and 12 edges removed.

The way one chooses to cut the nanoparticle can substantially alter the results of the simulations. This is not only true to avoid uncontrolled effects (Figure 7-10 b), but also to allow comparison between particle of different sizes but similar shape. The concept of geometrical similarity, especially at the small sizes typical of metal nanocrystals, is of uttermost importance. In particular, it is important to understand how much even just a row of atoms can alter the results.

7.3 WARREN PLOT CALCULATED FROM MOLECULAR DYNAMICS TRAJECTORIES

As explained in paragraph Real Powder sample vs MD simulation: the correction to $\langle \Delta \boldsymbol{L^2} \rangle$2.1.3, most literature simply refers to $\langle \Delta L^2 \rangle$ in the Warren Plot. This is an approximation that turns out to be exact in the case of samples with a null average $\langle \Delta L \rangle$. This is generally true of powder sample or nanoparticle suspended in a capping agent.

For molecular dynamics simulations of nanoparticles in a vacuum, an arbitrary lattice parameter is chosen and quantity like pair displacement are calculated with respect to that starting value.

It is therefore mandatory to use the correct expression for the Warren Plot, which corrects the variance for a non-zero $\langle \Delta L \rangle$.

$$\sigma^2_{hkl}(L) = \langle \Delta L^2 \rangle - \langle \Delta L \rangle^2 \qquad (7\text{-}4)$$

This point is better illustrated with references to two different EAM potentials, both constructed for Palladium with parameters tuned on the bulk properties. The potentials are Sheng (Sheng H.W. 2011) and Zhou (Zhou X.W. 2004), respectively.

When the same ideal configuration is simulated, the resulting real-dynamic trajectory differs considerably. The two spectra (calculated from the atomic coordinates, using the Debye Scattering Equation) (C. A. Gelisio L. 2010) are compared in Figure 7-13. One potential contracts the particle, while the other expands it, and obviously the final configurations differ drastically from the starting one and so $\Delta L \neq 0$.

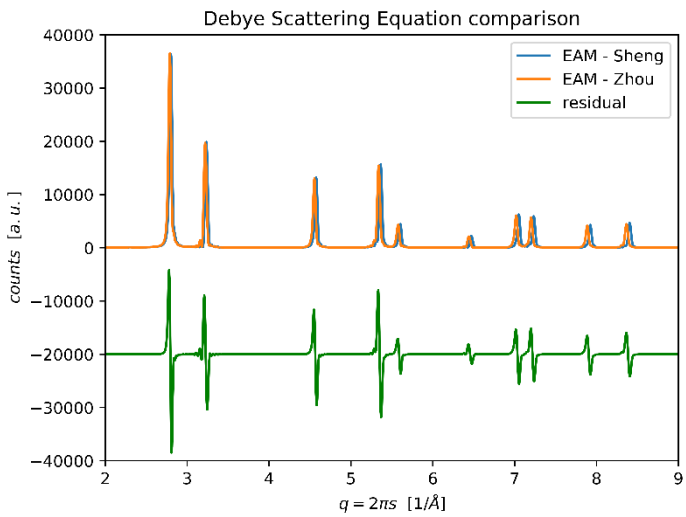

Figure 7-13

Comparison of the simulated powder patterns for the same nanoparticle (4nm 60% truncation cube with 4501 atoms) simulated with the two different EAM potentials (Sheng H.W. 2011) (Zhou L. G. 2012).

The most prominent difference is an overall decrease of the size with Sheng potential (the average lattice parameter is smaller than the starting bulk value, 3.89), while in the Zhou case there is an average increase in the interatomic distances.

If we calculate the value for $\langle \Delta L^2 \rangle$ for the 2 cases we find strikingly different trends (Figure 7-14). If instead of $\langle \Delta L^2 \rangle$ alone, the full variance $\langle \Delta L^2 \rangle - \langle \Delta L \rangle^2$ is used (Figure 7-15), the values provided by the two potentials are at least qualitatively similar. This specific case, showing the difference between two EAM potentials, highlights the importance of using equation (2-4) for Warren Plots.

Figure 7-15 shows also an important point, of interest in the practical application of the MD results discussed in this Thesis. The two trends for σ_{hkl}^2 obtained with the two EAM potentials have a finite difference but the overall shape is the same. This supports the implementation of a free parameter in the parametric description of the WP (equation (2-4)), ultimately making the quantity, σ_{hkl}^2, independent of the initial reference.

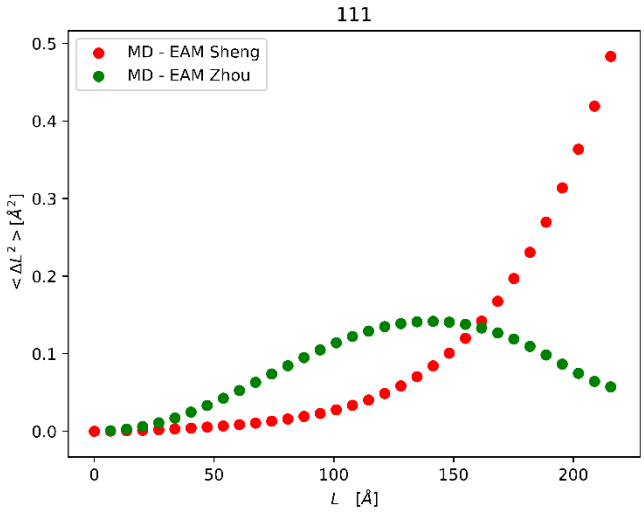

Figure 7-14

Comparison of the two different potentials for the quantity $\langle \Delta L^2 \rangle$ for a 4nm 60% truncation cube with 4501 atoms simulated with (Sheng H.W. 2011) and with (Zhou L. G. 2012) EAM potentials.

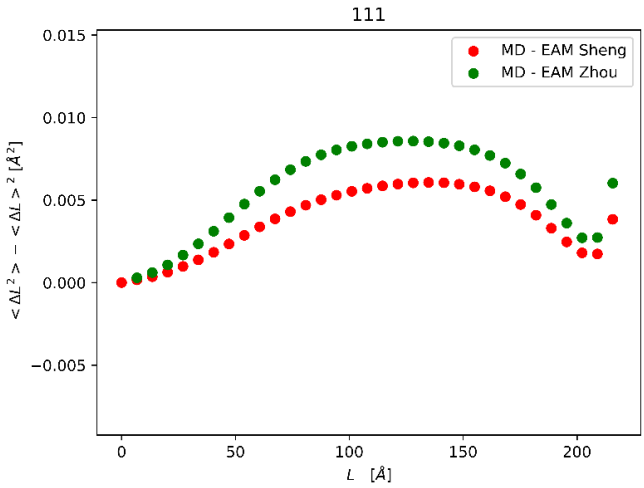

Figure 7-15

Comparison of two different EAM potentials for Pd. Trends of ${\sigma_{hkl}}^2$ for a 4nm 60% truncation cube with 4501 atoms simulated with (Sheng H.W. 2011) and with (Zhou L. G. 2012) EAM potentials.

REFERENCES

2012. In *Molecular Dynamics - Theoretical Developments and Applications in Nanotechnology and Energy*, a cura di L. Wang. InTechOpen.

2012. In *Molecular Dynamics - Studies of Synthetic and Biological Macromolecules*, a cura di L. Wang. InTechOpen.

Adler, T. & Houska, C. R. 1979. *J. Appl. Phys* (50): 3282–3287.

Agostini G., R. Grisenti, C. Lamberti, A. Piovano, and P. Fornasini. 2013. «Thermal effects on Rhodium nanoparticles supported on carbon.» *J. Phys. Conf. Ser.* (430).

Allen M.P., D.J. Tildsley. 1989. *Computer Simulation of Liquids.* Oxford: Oxford University Press.

Allen R.E. & F.W. DeWette. 1969. «Mean-Square Amplitudes of Vibration at a Surface.» *Phys. Rev.* (186): 1320-1323.

Azzaza S., S. Alleg, J.-J Sunol. 2015. «Microstructure characterization and thermal stability of the ball milled iron powders.» *J Therm. Anal. Calorim.* (119): 1037-1046.

Bai H.Y., J.L. Luo, D. Jin & J.R. Sun Bai. 1996. «Particle size and interfacial effect on the specific heat of nanocrystalline Fe.» *J. Appl. Phys.* (79).

Beni G., and P.M. Platzman. 1976. «Temperature and polarization dependence of extended x-ray absorption fine-structure spectra.» *Phys. Rev. B* (14): 1514-1518.

Beyerlein K.R., R. L. Snyder, M. Li, and P. Scardi. 2012 . *Nanosci. Nanotechnol Vol. 12, No. 11* 8554-8560.

Beyerlein, K. R., Leoni, M. & Scardi, P. 2012. «Temperature diffuse scattering of nanocrystals.» *Acta Crystallogr. Sect. A* (Acta Crystallogr. Sect. A) (68): 382–392 .

Blazhynska M. M., Alexander Kyrychenko & Oleg N. Kalugin. 2018. «Molecular dynamics simulation of the size-dependent morphological stability of cubic shape silver nanoparticles.» *Molecular Simulation* 12 (44): 981-991.

Blazhynska Margaret M., Alexander Kyrychenko & Oleg N. Kalugin. 2018. «Molecular dynamics simulation of the size-dependent morphological stability of cubic shape silver nanoparticles.» *Molecular Simulation* 12 (44): 981-991.

Bolt, R.H. 1939. «Normal Modes of Vibration in Room Acoustics: Angular Distribution Theory.» *J. Acoust. Soc. Amer.* (10).

Born M, . and K. Huang,. 1954. *Dynamical Theory of Crystal Lattices.* London: Oxford University Press.

Briki F., and D.Genest. 1994. «Canonical analysis of correlated atomic motions in DNA from molecular dynamics simulation.» *Biophys. Chem.* (52): 35-43.

Broseghini M., M D'Incau, L Gelisio, NM Pugno, P Scardi. 2016. «Effect of jar shape on high-energy planetary ball milling efficiency: Simulations and experiments.» *Materials & Design* (110): 365-374.

Butt, N. M., Bashir, J., Willis, B. T. M. & Heger, G. 1988. «Compilation of temperature factors of cubic elements.» *Acta Crystallogr. Sect. A* (44): 396–399 .

Buyers, Kim S M & W J L. 1978. «Vacancy formation energy in iron by positron annihilation.» *J. Phys. F: Metal Phys.* (8): L103-L108.

Calvin, S. 2013. «EXAFS for Everyone.» *Boca Raton: CRC Press.*

Chandler, D. 1987. «Introduction to Modern Statistical Mechanics.» 249.

Clark B.C., R. Herman & R.F. Wallis. 1965. «Theoretical Mean-Square Displacements for Surface Atoms in Face-Centered Cubic Lattices with Applications to Nickel.» *Phys. Rev.* (139): A860-A867.

Cline, J. P., Deslattes, R. D., Staudenmann, J.-L., Kessler, E. G., Hudson, L. T., Henins, A. & Cheary, R.W. 2000. *Certificates SRM 640c and SRM 660a.* Gaithersburg, MD, USA: NIST.

D'Incau, M., Leoni, M. & Scardi, P. 2007. «High-energy grinding of FeMo powders.» *J. Mater. Res.* (22): 1744–1753 .

Dalba G., & P.Fornasini,. 1997. *J. Synchrotron Rad.* (4): 243-255.

Daw, M. S. & Baskes, M. I. 1984. *Phys. Rev. B* 29: 6443–6453.

Daw, M. S. & Baskes, M. I. 1983. *Phys. Rev. Lett.* 50: 1285–1288.

Debye, P.J.W. 1913. «Interferenz von Röntgenstrahlen und Wärmebewegung.» *Annalen der Physik* 348: 49–92. doi:10.1002/andp.19133480105.

Di Cicco A. M. Berrettoni, S. Stizza, E. Bonetti, G. Cocco. 1994. «Microstructural defects in nanocrystalline iron probed by x-ray-absorption spectroscopy.» *Phys. Rev. B* 17 (50): 12386-12397.

Di Cicco A., G.Aquilanti, M. Minicucci, E. Principi, N. Novello, A. Cognigni, and L. Olivi. 2009. *Journal of Physics: Conference Series* (190).

Dove M. 2003. *Structure and Dynamics: An Atomic View of Materials.* New York: Oxford University Press.

Dove M.T. 1993. *Introduction to lattice dynamics.* New York: Cambridge University Press.

Egami T., and S.J.L. Billinge. 2003. *Underneath the Bragg Peaks: Structural Analysis of Complex Materials.* Oxford, England: Pergamon Press, Elsevier.

Einstein, Albert. 1905. «Über die von der molekularkinetischen Theorie der Wärme geforderte Bewegung von in ruhenden Flüssigkeiten suspendierten Teilchen.» *Annalen der Physik, 322 (8)* 549–560.

Eynatten G. Von, H.E. Bömmel,. 1977. «Size and Temperature Dependence of the Mossbauer Debye Waller Factor of Iron Microcrystals.» *Appl. Phys.* (14): 415-421.

Fornasini, P. 2014. «Chapeter 6.» In *Synchrotron Radiation: Introduction to X-ray Absorption Spectroscopy*, a cura di F. Boscherini & C. Meneghini S. Mobilio. Heidelberg: Springer.

Gelisio L., Beyerlein K. R., Scardi P. 2013. «Atomistic modeling of lattice relaxation in metallic nanocrystals.» *Thin Solid Films* 536: 35-39.

Gelisio L., C. Azanza Ricardo, M. Leoni and P. Scardi. 2010. «Real-space calculation of powder diffraction patterns on.» *J. Appl. Cryst.* (43): 647-653.

Gelisio L., C.L. Azanza Ricardo, M. Leoni & P. Scardi. 2010. «Real-space calculation of powder diffraction patterns on graphics processing.» *J. Appl. Crystallogr.* (43): 647-653.

Gelisio L., K.R. Beyerlein & P. Scardi. 2013. «Atomistic modeling of lattice relaxation in metallic nanocrystals.» *Thin Solid Films* (530): 35–39.

Guinier, A. 1963. *Crystals, Imperfect Crystals, and Amorphous Bodies: X-ray Diffraction.* San Francisco: W. H. Freeman and Company.

Huang W.J., R. Sun, J. Tao, L.D. Menard, R.G. Nuzzo, and J.M. Zuo. 2008. «Coordination-dependent surface atomic contraction in nanocrystals revealed by coherent diffraction.» *Nat. Mater.* (7): 308–313.

Humphrey W. A. Dalke, and K. Schulten. 1996. «VMD: visual molecular dynamics.» *J. Molec. Graphics* (14): 33-38.

Inagaki M., Y. Sasaki, M. Sakai. 1983. «Debye-Waller parameter of palladium metal powders.» *J. Mat. Sci.* (18): 1803-1809.

J., Allen M. P. & Tildesley D. 2017. *Computer Simulation of Liquids.* 2nd. Oxfor University Press.

Jeong I.-K., T. Proffen, F. Mohiuddin-Jacobs, and S.J.L. Billinge. 1999. «Measuring correlated atomic motion using X-ray diffraction.» *J. Phys. Chem. A* 7 (103): 921-924.

Jeong, I.-K., Heffner, R. H., Graf, M. J. & Billinge, S. J. L. 2003. «Lattice dynamics and correlated atomic motion from the atomic pair distribution function.» *Phys. Rev. B* (67): 104301–104309 .

Jiawei Zhang, Qin Kuang, Yaqi Jiang, Zhaoxiong Xie. 2016. «Engineering high-energy surfaces of noble metal nanocrystals with enhanced catalytic performances.» *Nano Today* 11 (5): 661-677.

Jiménez-Villacorta, F., Muñoz-Martín, A. & Prieto, C. 2004. *J. Appl. Phys.* (96): 6224–6229.

Jin M., H. Liu, H. Zhang, Z. Xie, J. Liu, and Y. Xia. 2011. *Nano Res.* 4 (83).

Jones E, Oliphant E, Peterson P, et al. 2001. *SciPy: Open Source Scientific Tools for Python.* http://www.scipy.org/.

Kamberaj H., and A. Van Der Vaart. 2009. «Extracting the causality of correlated motions from molecular dynamics simulations.» *Biophys. J.* (97): 1747–1755.

Klug H. P., Alexander L. E. 1974. *X-Ray Diffraction Procedures: For Polycrystalline and Amorphous Materials.* 2nd. Wiley.

Krivoglaz, M. 1969. *Theory of X-ray and Thermal-Neutron Scattering by Real Crystals.* New York: Plenum Press.

Kuhs, W. F. 2006. «chapter 1.» In *International Tables for Crystallography, Vol. D, Physical Properties of Crystals*, a cura di A. Authier, 228–242. Chester: International Union of Crystallography.

Kuwano H., H. Ouyang & B. Fultz. 1992. «A Mössbauer spectrometry study of the magnetic properties and Debye temperature of nanocrystalline Cr-Fe.» *Mat. Sci. Forum* 561-568.

Kuzmin A., and J. Chaboy. 2014. «EXAFS and XANES analysis of oxides at the nanoscale.» *IUCrJ* (1): 571-589.

Kwangjin An, Gabor A. Somorjai. 2012. «Size and Shape Control of Metal Nanoparticles for Reaction Selectivity in Catalysis.» *ChemCatChem* 4 (10): 1512-1524.

Laskar, M. & Skrabalak, S. E. 2014. «Decoupling the Geometric Parameters of Shape-Controlled Pd Nanocatalysts.» *ACS Catal.* (4): 1120–1128.

Lee, June Gunn. 2011. *Computational Materials Science: an Introduction.* Taylor & Francis Inc.

Leonardi, A., Leoni, M. & Scardi, P. 2013. «Atomistic modelling of polycrystalline microstructures: An evolutional approach to overcome topological restrictions.» *Comput. Mater. Sci.* (67): 238–242 .

Leonardi, A., Leoni, M., Li, M. & Scardi, P. 2012. «Strain in atomistic models of nanocrystalline clusters.» *J. Nanosci. Nanotechnol* (12): 8546–8553 .

Leonardi, A., Leoni, M., Siboni, S. , Scardi, P. 2012. «Common Volume Function and diffraction line profiles from polyhedral domains.» *Journal of Applied Crystallography* 45 (6): 1162-1172.

Leonardi, A., Scardi, P. & Leoni M. 2012. «Realistic nano-polycrystalline microstructures: beyond the classical voronoi tessellation.» *Philos. Mag.* (92): 986–1005 .

Leoni M., Tancredi C., Scardi P. 2006. «PM2K: A flexible program implementing Whole Powder Pattern Modelling.» *Zeitschrift für Kristallographie Supplements* (23): 249-254.

Levine, B. G., Stone, J. E. & Kohlmeyer, A. (2011). *J. Comput. Phys.* 230: 3556–3569.

Long Ran, Keke Mao, Xiaodong Ye, Wensheng Yan, Yaobing Huang, Jianyong Wang, Yao Fu, Xisheng Wang, Xiaojun Wu, Yi Xie, and Yujie Xiong. 2013. «Surface Facet of Palladium Nanocrystals.» *J. Am. Chem. Soc.* 135 (8): 3200–3207. doi:10.1021/ja311739v.

Lonsdale, Katherine. 1968. *International Tables for Crystallography.* Birmingham: Kynoch Press.

Lottici P.P. 1987. «Extended x-ray-absorption fine-structure Debye-Waller factors and vibrational density of states in amorphous arsenic.» *Physical Review B* 35 (3): 1236.

Lottici P.P., Rehr J.J. 1980. «A connection between Raman intensities and EXAFS Debye-Waller factors in amorphous solids.» *Solid State Communications* 35 (7): 565-567.

Luo Mingchuan, Shaojun Guo. 2017. «Strain-controlled electrocatalysis on multimetallic nanomaterials Nature Reviews Materials.» doi:10.1038/natrevmats.2017.59 .

Maa, D.Y. 1939. «Distribution of Eigentones in a Rectangular Chamber at Low Frequency Range.» *J. Acoust. Soc. Amer.* (10): 235.

MacRae A. U., and Germer L. H. 1962. *Physical Review Letters* 8: 489.

Maradudin A.A., E.W. Montroll, G.H. Weiss, and I.P. Ipatova. 1971. *Theory of Lattice Dynamics in the Harmonic Approximation.* New York: Academic Press.

Martyna, G. J., Tobias, D. J. & Klein, M. L. 1994. *J. Chem. Phys* (101): 4177–4189.

Maslen E.N. 2006. «Vol. C, Chapter 6.3.» In *International Tables for Crystallography*, 599–608.

Mendelev M.I. et al. 2003. «Development of new interatomic potentials appropriate for crystalline and liquid iron.» *Philos. Mag.* (83): 3977–3994.

Michailov M., & I. Avramov. 2012. «Surface Energy, Surface Debye Temperature and Specific Heat of Nanocrystals.» *Journal of Physics: Conference Series* (398).

Miller A. P., and B. N. Brockhouse. 1968. «Anomalous Behavior of the Lattice Vibrations and the Electronic Specific Heat of Palladium.» *Phys. Rev. Lett.* (20).

Miller A.P., and B.N. Brockhouse. 1971. «Crystal Dynamics and Electronic Specific Heats of Palladium and Copper.» *Can. J. of Physics* (49): 704-723.

Miyanaga T., & T. Fujikawa. 1994. «Quantum Statistical Approach to Debye-Waller Factor in EXAFS, EELS and ARXPS. III. Applicability of Debye and Einstein Approximation.» *J. Phys. Soc. Jpn.* (63): 3683-3690.

Miyanaga T., M. Nakamae, H. Nago, Y. Ohori, and T. Fujikawa. 2012. «Photoelectron Mean Free Path on the EXAFS Analyses for Nanoparticles.» *Surf. Sci. Nanotech.* (10): 565-568.

More, J. J. 1977. «The Levenberg-Marquardt Algorithm: Implementation and Theory.» In *Numerical Analysis*, a cura di G. A. Watson, 105-116. Springer Verlag.

Niu, W. & Xu, G. 2011. «Crystallographic control of noble metal nanocrystals.» *Nano Today* (6): 265–285.

Parrinello M., & Rahaman, A. 1981. *J. Appl. Phys.* (52): 7182.

Pauling, L. 1947. «Atomic Radii and Interatomic Distances in Metals.» *J. Am. Chem. Soc.* (69): 542–553.

Perez Demydenko C., Scardi P. 2017. «Diffraction peak profiles of surface relaxed spherical Nanocrystals.» *Phil. Mag .*

Plimpton, S. 1995. «Fast Parallel Algorithms for Short-Range Molecular Dynamics.» *J. Comput. Phys.* 117: 1–19.

Popa, N. 1998. *J. Appl. Cryst.* (31): 176-180.

Purushotham E., & N. Gopi Krishna,. 2010. «Effect of lattice strain on the Debye-Waller factors of Mg, Zn and Cd.» *Indian J. Phys.* (84): 887-893.

Rao, C.N.R., Thomas, P.J., Kulkarni, G.U. 2007. *Nanocrystals:: Synthesis, Properties and Applications.* Berlin Heidelberg: Springer.

Rapaport, D. C. 2004. *The Art of Molecular Dynamics Simulation.* 2nd . Cambridge University Press .

Rebuffi L., A. Troian, R. Ciancio, E. Carlino, A. Amimi, A. Leonardi & P. Scardi. 2016. «On the reliability of powder diffraction Line Profile Analysis of plastically deformed nanocrystalline systems.» *Sci. Rep.* (6).

Roe, G.M. 1941. «Frequency Distribution of Normal Modes.» *J. Acoust. Soc. Amer.* 1 (13): 1-7.

Sandia National Laboratiries. s.d. *LAMMPS Publications.* https://lammps.sandia.gov/papers.html.

Scardi P, L Rebuffi, M Abdellatief, A Flor, A Leonardi. 2017. «Debye–Waller coefficient of heavily deformed nanocrystalline iron.» *Journal of applied crystallography* 50 (2): 508-518.

Scardi P., A. Leonardi, L. Gelisio, M. R. Suchomel, B. T. Sneed, M. K. Sheehan, and C.-K. Tsung. 2015. «Anisotropic atom displacement in Pd nanocubes resolved by molecular dynamics simulations supported by x-ray diffraction imaging.» *Phys. Rev. B* 91.

Scardi P., and L. Gelisio. 2016. «Vibrational Properties of Nanocrystals from the Debye Scattering Equation.» *Sci. Reports* (6).

Scardi P., Azanza Ricardo C.L., Perez-Demydenko C., Coelho A. A. 2018. «Whole powder pattern modelling macros for TOPAS.» *Journal of Applied Crystallography* 51 (6): 1752-1765.

Scardi P., Flor A. 2018. «Correlated Debye model for atomic motions in metal nanocrystals.» *Philosophical Magazine* 98 (15): 1412-1435.

Scardi P., Leoni M. 2002. *, Whole Powder Pattern Modelling April 2002, Acta crystallographica. Section A, Foundations of crystallography* 58 (2): 190-200. doi:10.1107/S0108767301021298.

Scardi, P. & Leoni, M. 2001. «Diffraction Line Profiles from Polydisperse Crystalline Systems.» *Acta Cryst. A57,* 604–613.

Scardi, P. 2008. «chapter 13.» In *Powder Diffraction: Theory and Practice*, a cura di R. E. Dinnebier & S. J. L. Billinge, 376–413. Cambridge: Royal Society of Chemistry.

Scardi, P. 2008. «Microstructural Properties: Lattice Defects and Domain Size Effects.» In *Powder Diffraction: Theory and Practice*, 376–413 . Cambridge: The Royal Society of Chemistry.

Scardi, P., Ermrich, M., Fitch, A., Huang, E.-W., Jardin, R., Kuzel, R., Leineweber, A., Mendoza Cuevas, A., Misture, S. T., Rebuffi, L. & Schimpf, C. 2018. «Size–strain separation in diffraction line profile analysis.» *J. Appl. Cryst.* (51): 831-843.

Schnohr C.S., & M.C. Ridgway. 2015. *X-Ray Absorption Spectroscopy of Semiconductors.* Berlin Heidelberg: Springer-Verlag.

Schoening, F.R.L. 1968. «The Debye-Waller factor for small cubes and thin films.» *Acta Crystallogr.* (A24): 615-619.

Sevillano E., H. Meuth, J.J. Rehr,. 1979. *Phys. Rev. B* (20).

Shafai G., Alcántara Ortigoza M. , and Rahman T. S. 2012. «Vibrations of Au13 and FeAu12 nanoparticles and the limits of the Debye temperature concept.» *J. Phys. Condens. Matter.,* 104026.

Shafai G., M. Alcántara Ortigoza and T. S. Rahman. 2012. «Vibrations of Au13 and FeAu12 nanoparticles and the limits of the Debye temperature concept.» *J Phys Condens Matter* 10 (24).

Sheng H. 2018. *EAM potentials.* https://sites.google.com/site/eampotentials/Pd#TOC-Properties-Predicted-by-EAM.

Sheng H.W., M.J. Kramer, A. Cadien, T. Fujita and M.W. Chen,. 2011. «Highly-optimized EAM potentials for 14 fcc metals.» *Physical Review B* 83 (13).

Shi C., E.L. Redmond, A. Mazaheripour, P. Juhas, T.F. Fuller and S.J.L. Billinge. 2013. «Evidence for anomalous bond softening and disorder below 2 nm diameter in carbon supported platinum nanoparticles from the temperature dependent peak width of the atomic pair distribution function.» *J. Phys. Chem. C* 14 (117): 7226-7230.

Shinoda, Shiga, Mikami. 2004. *Phys Rev B* (69).

Sirdeshmukh D.B., G. Subhadra, K.A. Hussain, N. Gopi Krishna, B. Rachavendra Rao. 1993. «X-ray study of strained CdTe powders.» *Cryst. Res. Technol* (28): 15-18.

Solla-Gullón J., E. Garnier, J.M. Feliu, M. Leoni, A. Leonardi & P. Scardi. 2015. «Structure and morphology of shape-controlled Pd nanocrystals.» *J. Appl. Cryst.* (48): 1534–1542.

Stokes, A. R., & Wilson, A. J. C. 1944. «The diffraction of X rays by distorted crystal aggregates.» *Proceedings of the Physical Society* 174 (56).

Stukowski A. 2010. «Visualization and analysis of atomistic simulation data with OVITO - the Open Visualization Tool.» *Modelling Simul. Mater. Sci. Eng.* 18.

Suzuki Y., T. Miyanaga, K. Kita, T. Uruga, and I. Watanabe. 2005. «Local structure of Ag nano-clusters deposited on silicon wafer by total conversion electron yield XAFS.» *Phys. Scr. T* (115): 459-461.

Thijssen, J. 2007. *Computational Physics.* 2nd. Cambridge University Press.

Tuckerman Alejandre, Lopez-Rendon, Jochim, Martyna,. 2006. *J. Phys. A: Math. Gen.* (39).

Tuckerman. 2010. *Statistical Mechanics: Theory and Molecular Simulation.* Oxford Graduate Texts.

Urban, J.P. 1975. «Thermal diffuse X-ray scattering for small samples and small coherent scattering domains.» *Acta Crystallogr.* (A31): 95–100.

Vaccari M., and P. Fornasini. 2006. «Einstein and Debye models for EXAFS parallel and perpendicular mean-square relative displacements.» *J. Synchrotron Rad.* (13): 321-325.

Valiev R.Z., R.K. Islamgaliev, I.V. Alexandrov. 2000. «Bulk nanostructured materials from severe plastic deformation.» *Progress in Materials Science* (45): 103-189.

van Duin A.C.T., S. Dasgupta, F. Lorant, and W.A. Goddard. 2001. «ReaxFF: A Reactive Force Field for Hydrocarbons.» *The Journal of Physical Chemistry A* (105): 9396–9409.

VanHove M.A., W.H. Weinberg, C.-M.Chan. 1986. *Low-Energy Electron Diffraction Experiment, Theory and Surface Structure Determination.* Berlin Heidelberg: , Springer-Verlag.

Veisz B., Z. Kiràly, L. Tòth, & B. Pécz. 2002. «Catalytic Probe of the Surface Statistics of Palladium Crystallites Deposited on Montmorillonite.» *Chem. Mater.* (14): 2882-2888.

Vetelino J.F., S.P.Gaur, S.S.Mitra. 1972. «Debye-Waller Factor for Zinc-Blende-Type Crystals.» *Phys.Rev. B* (5): 2360-2366.

Vidal-Iglesias, F., Arán-Ais, R., Solla-Gullón n, J., Garnier, E., Herrero, E., Aldaz, A. & Feliu, J. 2012. *Phys. Chem. Chem. Phys.* (14): 10258–10265.

W.F., Kuhs. 2006. «Vol. D, Chapter 1.9 .» In *International Tables for Crystallography*, 228–242.

Waller, Ivar. 1923. «Zur Frage der Einwirkung der Wärmebewegung auf die Interferenz von Röntgenstrahlen.» *Zeitschrift für Physik* 17: 398–408. doi:10.1007/BF01328696.

Wang J., Jing Wang, Shubin Yan, Tao Geng, and Tiancai Zhang. 2008. «Transferring cold atoms in double magneto-optical trap by a continuous-wave transfer laser beam with large red detuning .» *Review of Scientific Instruments* 79.

Warren B.E., Averbach B.L. 1950. «The Effect of Cold-Work Distortion on X-Ray Patterns.» *Journal of Applied Physics* 21: 595– 599. doi:doi: 10.1063/1.1699713.

Warren, B. E. 1955. «A generalized Treatment of Cold Work in Powder Patterns.» *Acta Crystallographica* (8): 483-486.

—. 1990. *X-Ray Diffraction.* New-York: Dover.

s.d. *WebElements.* Consultato il giorno March 2019. https://www.webelements.com.

Wenxin Niu, Guobao Xua. 2011. «Crystallographic control of noble metal nanocrystals.» *Nano Today* 6 (3): 265-285.

Wette, Allen R.E. & F.W. De. 1969. «Mean-Square Amplitudes of Vibration at a Surface.» *Phys. Rev.* (186): 1320-1323.

Wilkens, M. 1970. *Phys. Status Solidi (A)* (2): 359–370.

Willis B. T. M., A. W. Pryor,. 1975. *Thermal vibrations in crystallography.* Cambridge University Press.

Wilson, A. J. C. 1962. *X-ray optics: the diffraction of X-rays by finite and imperfect crystals.* London: Methuen.

Wulff G. 1901. «Zur Frage der Geschwindigkeit des Wachstums und der Auflösung der Krystallflagen.» *Zeitschrift für Krystallographie und Mineralogie* 34: 449–530.

Yan Zhou, Chuanchuan Jin, YongLi, Wenjie Shen. 2018. «Dynamic behavior of metal nanoparticles for catalysis.» *Nano Today* 20: 101-120.

Yang C.C., M.X. Xiao, W. Li, Q. Jiang. 2006. «Size effects on Debye temperature, Einstein temperature, and volume thermal expansion coefficient of nanocrystals.» *Solid State Communications* (139): 148–152.

Zhang, H., Jin, M. & Xia, Y. 2012. «Noble-Metal Nanocrystals with Concave Surfaces: Synthesis and Applications.» *Angew. Chem. Int. Ed.* (51): 7656–7673.

Zhao Z.H., H.W. Sheng, K. Lu. 2001. «Microstructure evolution and thermal properties in nanocrystalline Fe during mechanical attrition.» *Acta Mater.* (49): 365-375.

Zhao, Lu K.& Y.H. 1999. «Experimental evidences of lattice distortion in nanocrystalline materials.» *Nanostruct Mater.* (12): 559–562.

Zhou L. G., Hanchen Huang. 2012. «A Response Embedded Atom Method of Interatomic Potentials.» *Physical review. B, Condensed matter* 4 (87).

Zhou X.W., R.A. Johnson, and H.N.G. Wadley. 2004. «Misfit-energy-increasing dislocations in vapor-deposited CoFe/NiFe multilayers.» *Physical Review B* 69 (14). doi:10.1103/physrevb.69.144113.

LIST OF PUBLICATIONS

Debye–Waller coefficient of heavily deformed nanocrystalline iron

P Scardi, L Rebuffi, M Abdellatief, **A Flor**, A Leonardi

Journal of applied crystallography 50 (2), 508-518

Correlated Debye model for atomic motions in metal nanocrystals

P Scardi, **A Flor**

Philosophical Magazine 98 (15), 1412-1435

Vibrational properties of Pd nanocubes

A. Flor, C.-K. Tsung, & P. Scardi

Nanomaterials 9, 609.

Microstructural effects of high-energy grinding on poorly soluble drugs: the case study of efavirenz

E Cappelletto, L Rebuffi, **A Flor**, P Scardi

Powder diffraction 32 (S1), S135-S140

Structural characterization and functional correlation of Fe_3O_4 nanocrystals obtained using 2-ethyl-1,3-hexanediol as innovative reactive solvent in non-hydrolytic sol-gel synthesis

C. Sciancalepore, A.F. Gualtieri, P. Scardi, **A. Flor**, P. Alia, P. Tiberto, G. Barrera, M. Messori, F. Bondioli.

Materials Chemistry and Physics 207, 337-349

ACKNOWLEDGMENTS

The three years leading to the conclusion of this Doctoral Thesis have been challenging in many ways. It has been nevertheless a fundamental journey for me, a long period of time that allowed me to test my limits and discover abilities and skills I did not imagine possessing.

First of all, I am indebted to professor Paolo Scardi, who is not only a brilliant scientist and a very clever person, but also and foremost a teacher. He taught me things that go well beyond the world of research and academia, showing that the path leading to an achievement is built on the foundation of constant effort and dedication. Professor Scardi proved to me that there is no flaw or lack of skills that can not be overcome with imagination and faith in oneself.

I also want to thank my mother and my father, who have always supported me and, no matter how much I strayed from the right path, they still believed in me. My core values and my curiosity toward everything in the world are the consequence of my parents' efforts and sacrifices, for which I will be always grateful.

My brother is also a fundamental part of who I am, and I want to thank him, because I feel that the bond between us is far stronger than a simple biological relation. My brother and I grew up together, shaping one another and raising the bar for each other day after day, even in the moments when we were far apart. Thank you, Enrico.

In the past years I met so many wonderful and special people, both in the university and outside. Even those with whom I had arguments, or resented in some way, are nonetheless deserving of recognition, since it is only thorough discussion and confrontation that new and better ideas can rise.

I am grateful to my colleagues and co-workers at the University: Mirco D'Incau, Syafiq, Binayak, Narges, Ketan, Eleonora and Camilo that especially in the last year showed me how a wonderful workplace can positively influence your day. Honourable mention to Rocco, that no matter what always shares my troubles.

Special thanks also to Luca Rebuffi, who helped me a lot during a difficult period.

A big thanks also to Dodo, Klaus, Lucky, Taberna, Monti, Zo, Biasi for being there when I needed them.

The biggest thanks, the immense gratitude and the main acknowledgment goes however to Daniela, who gives my life purpose and has supported me in every moment, every day. She is the fulcrum about which my erratic character pivots, she is the architect that channels my chaotic imagination into a structured system, she is the shaper of equilibrium and a master at converting flaws into assets. Daniela, I thank you, because you understand me, and you proved me wrong time and time again showing me I was right. Thank you.